
Electronic Thesis and Dissertation Repository

10-13-2019 2:00 PM

Airborne topological acoustics

Xingxing Liu, *The University of Western Ontario*

Supervisor: Yang, Jun, *The University of Western Ontario*

A thesis submitted in partial fulfillment of the requirements for the Doctor of Philosophy degree in Mechanical and Materials Engineering

© Xingxing Liu 2019

Follow this and additional works at: <https://ir.lib.uwo.ca/etd>



Part of the [Acoustics, Dynamics, and Controls Commons](#)

Recommended Citation

Liu, Xingxing, "Airborne topological acoustics" (2019). *Electronic Thesis and Dissertation Repository*. 6577.

<https://ir.lib.uwo.ca/etd/6577>

This Dissertation/Thesis is brought to you for free and open access by Scholarship@Western. It has been accepted for inclusion in Electronic Thesis and Dissertation Repository by an authorized administrator of Scholarship@Western. For more information, please contact wlsadmin@uwo.ca.

Abstract

Advances in topological acoustics are leading to potential development for noise attenuation, ultrasonic imaging, sound manipulation, and information delivering, etc. Recently, ideas and methodologies from condensed-matter physics, such as the quantum Hall effect (QHE), the quantum spin Hall effect (QSHE), and the quantum valley Hall effect (QVHE), combined with configurations of sonic crystals and metamaterials, have been investigated in manipulating acoustic transmissions in the form of one-way edge modes and defect-immune protected acoustics. However, many related studies are still in their infancy and mostly rely on bulky, noisy, overly complicated, untunable and narrow-band-effective facilities, and so it is highly desirable but challenging to design more practical topological acoustic systems, with backscattering immune, tunable, broadband and miniaturized topological acoustic properties.

This thesis investigates novel modulation mechanisms, versatile configurable lattice structures, and microscale acoustic transmission mechanisms to solve the aforementioned airborne topological acoustic challenges. Starting with the rotating modified spiral springs configuration adjusting the inner radius without altering the external lattice structure, a gapless topologically protected acoustic flow-free resonator system based on the QVHE in reconfigurable sonic crystals is designed to realize backscattering immune, tunable and broadband functional acoustic applications. Then, based on the acoustic analogue of the QHE, to replace the generating mechanism of the noisy fan-induced airflow, a new method using heat-induced natural convection coupled with an acoustic circulator is proposed to realize robust nonreciprocal acoustic propagation. This strategy is more feasible because of its dynamic control and versatile topological structures in the absence of moving parts. To further promote the topological acoustics into a more practical stage, based on the QSHE, a temperature modulation scheme is designed to demonstrate that the Floquet topological insulators with thermal-induced impedance matching can realize robust topological acoustic propagation, which is especially useful for noiseless and miniaturized airborne acoustics. Thermal modulation enables miniaturized topological airborne acoustics to the millimeter scale or even smaller. Additionally, a theoretical model with a second-order slip boundary to

describe acoustic wave propagation in micro- and nanochannels is proposed to investigate the miniaturized topological acoustic transmission mechanism. Based on the molecular-based direct simulation Monte Carlo (DSMC) method, this model provides an analytical solution beneficial for topological acoustics in ultrasonic or in miniaturized structures.

Keywords

Topological acoustics, the quantum Hall effect, the quantum spin Hall effect, the quantum valley Hall effect, sonic crystals, metamaterials, tunability, miniaturization, versatile configurable lattice structures, microscale acoustic transmission mechanism, heat-induced natural convection, thermal-induced impedance matching, direct simulation Monte Carlo method.

Summary for Lay Audience

Advances in topological acoustics are leading to potential development for noise attenuation, ultrasonic imaging, sound manipulation, and information delivering, etc. Recently, ideas and methodologies from condensed-matter physics, combined with configurations of sonic crystals and metamaterials, have been investigated in manipulating acoustic transmissions in the form of one-way edge modes and defect-immune protected acoustics. However, many related studies are still in their infancy and mostly rely on bulky, noisy, overly complicated, untunable and narrow-band-effective facilities, and so it is highly desirable but challenging to design more practical topological acoustic systems, with backscattering immune, tunable, broadband and miniaturized topological acoustic properties.

This thesis investigates novel modulation mechanisms, versatile configurable lattice structures, and microscale acoustic transmission mechanisms to solve the aforementioned airborne topological acoustic challenges. Starting with the rotating modified spiral springs configuration adjusting the inner radius without altering the external lattice structure, a gapless topologically protected acoustic flow-free resonator system in reconfigurable sonic crystals is designed to realize backscattering immune, tunable and broadband functional acoustic applications. Then, to replace the generating mechanism of the noisy fan-induced airflow, a new method using heat-induced natural convection coupled with an acoustic circulator is proposed to realize robust one-way acoustic propagation. This strategy is more feasible because of its dynamic control and versatile structures in the absence of moving parts. To further promote the topological acoustics into a more practical stage, a temperature modulation scheme is designed to demonstrate that thermal-induced impedance matching can realize robust topological acoustic propagation, which is especially useful for noiseless and miniaturized airborne acoustics. Thermal modulation enables miniaturized topological airborne acoustics to the millimeter scale or even smaller. Additionally, a theoretical model with a second-order slip boundary to describe acoustic wave propagation in a small scale is proposed to investigate the miniaturized acoustic transmission mechanism. Based on the molecular-based direct simulation Monte Carlo method, this model provides an analytical solution beneficial for topological acoustics in ultrasonic or in miniaturized structures.

Co-Authorship Statement

This thesis is based upon a combination of published work. Various chapters are adapted from the following list of published work.

Chapter 2 was drafted by Xingxing Liu based on the following publication:

Liu, X., Q. Guo, and J. Yang, Tunable acoustic valley edge states in a flow-free resonator system. *Applied Physics Letters*, 2019. **115**(7): p. 074102.

Chapter 3 was drafted by Xingxing Liu based on the following publication:

Liu X, Cai X, Guo Q, Yang J. Robust nonreciprocal acoustic propagation in a compact acoustic circulator empowered by natural convection[J]. *New Journal of Physics*, 2019, 21(5): 053001.

Chapter 4 was drafted by Xingxing Liu based on the following publication:

Liu, Xingxing, Qiuquan Guo, and Jun Yang. "Miniaturization of Floquet topological insulators for airborne acoustics by thermal control." *Applied Physics Letters* 114.5 (2019): 054102.

Chapter 5 was drafted by Xingxing Liu based on the following publication:

Liu X, Cai X, Guo Q, Yang J. Study of acoustic wave propagation in micro-and nanochannels[J]. *Wave Motion*, 2018, 76: 51-60.

All other chapters are drafted and revised solely by Xingxing Liu.

Acknowledgments

It is a pleasure to acknowledge the meaningful contribution from everyone who supported to make this work possible.

First and foremost, I would like to thank my supervisor, Professor Jun Yang, for his patient guidance, valuable suggestions, and positive encouragement throughout my PhD period. I really appreciate that I have the opportunity and honor to be working under the supervision of such brilliant and innovative mind. Also, I would like to thank my advisor committees, Prof. Samuel F Asokanthan and Prof. Liying Jiang, for their kindly guidance.

Many thanks to all of the outstanding colleagues I have had at the University of Western Ontario, for all the passionate and meaningful discussions, and for all the interesting moment we shared together. I have learned a lot from all of you and am very appreciative to have a team with people like you. I would also like to give special thanks to Dr. Cai, Dr. Guo and Dr. Zhang for their insightful suggestions and guidance in both research and life, which really helps a lot to do my study during my PhD period.

Also, I would like to thank all my families and my friends who are always backing me up and relieving my struggles. Without any of you, I would never go this far.

Finally, a big thank you goes to the Natural Science and Engineering Research Council of Canada (NSERC) and the University of Western Ontario. Their support and funding has made all of this research possible, and I am very grateful for the opportunities they have provided.

Table of Contents

Abstract	ii
Summary for Lay Audience	iv
Co-Authorship Statement.....	v
Acknowledgments.....	vi
Table of Contents	vii
List of Tables	x
List of Figures	xi
List of Abbreviations	xvi
Chapter 1	1
1 Introduction to the airborne topological acoustics	1
1.1 History and development of the QHE, QSHE and the QVHE in the condensed-matter system	1
1.2 Acoustic analogues of the QHE for the airborne nonreciprocal acoustics and topological acoustics	5
1.3 Acoustic analogues of the QSHE for the airborne topological acoustics	8
1.4 Acoustic analogues of the QVHE for the airborne topological acoustics	14
1.5 Lattice Boltzmann method and DSMC method for the miniaturization of topological acoustics	19
1.6 Challenges and objectives.....	23
1.7 Outline of the thesis	24
Chapter 2.....	27
2 Tunable acoustic valley edge states in a flow-free resonator system.....	27
2.1 Introduction.....	27
2.2 Topological acoustic model and mode analysis.....	30
2.3 Analytical acoustic band structures	31
2.4 Topological acoustic performance	34

2.5 Supplementary material	37
Chapter 3.....	40
3 Robust nonreciprocal acoustic propagation in a compact acoustic circulator empowered by natural convection	40
3.1 Introduction.....	40
3.2 Prototype design and mode analysis	42
3.3 Velocity distribution of heat-induced natural convection.....	44
3.4 Nonreciprocal performance	46
3.5 Coupled-mode theory for an acoustic circulator by angular-momentum bias.....	48
3.6 Robust nonreciprocal acoustic circulator with other interior configurations.....	49
3.7 Discussion.....	51
3.8 Supplementary material	52
Chapter 4.....	56
4 Miniaturization of Floquet topological insulators for airborne acoustics by thermal control	56
4.1 Introduction.....	56
4.2 Prototype design and mode analysis	58
4.3 Topological performance	61
4.4 Supplementary material	64
Chapter 5.....	70
5 Study of acoustic wave propagation in micro- and nanochannels	70
5.1 Introduction.....	70
5.2 Theory for acoustic wave propagation in narrow channels	73
5.3 The complete solutions based on slip boundary conditions.....	76
5.4 DSMC for the verification of acoustic wave propagation in a narrow channel....	79
5.5 Properties of the new second-order slip model.....	82
5.6 Conclusions.....	86

6 Conclusion and Future Work	88
6.1 Conclusion	88
6.2 Future work.....	91
References.....	93
Curriculum Vitae	104

List of Tables

Table 1-1. Schematic illustration of different topological phases	2
Table 5-2. Values of different slip coefficients	78

List of Figures

Figure 1-1. The analogous QHE in sonic crystal systems. (a-b) The fan-induced-airflow acoustic circulator and its nonreciprocal performance. (c) The hexagonal acoustic lattice incorporated with circulating airflow is presented, and has topological performance against the structure disorder and defects. (d) The honeycomb acoustic lattice with rotating airflow, and the robust edge state transmission against various defects. Reprint with permission from: (a-b) ref.[29], (c) ref. [30], (d) ref. [31]. 7

Figure 1-2. (a) Photograph of a 2D coupled metamaterial ring lattice system. The U-shape waveguides are the input and output ports with specific pseudo-spins. (b) Photograph of one lattice ring surrounded by four coupling rings. The red arrow shows that the wave is carrying pseudo-spin-up, *viz.* propagating in clockwise. (c) Details of the metamaterial waveguide. (d) The simulated and experimental pressure amplitude distributions when pseudo-spin-up and pseudo-spin-down acoustic one-way edge states are excited, showing the robustness of the edge states against the sharp bending. Reprint with permission from ref. [40] 10

Figure 1-3. (a) Schematic of the hexagonal acoustic metamaterial lattice composed of artificial metamolecules. (b) Dispersion relation of the lattice based on the original unit cell for single Dirac cones at the 1st BZ corners. (c) Topologically protected one-way edge waveguide for airborne acoustics and the corresponding acoustic intensity fields. The pseudospin-down mode is excited at the lower and upper edge, and the topological edge states with three types of defects: cavity, disorder, and bends. (d) The spin-locked edge state propagation. (e) Robustness against versatile defects. Reprint with permission from: (a-c) ref. [43] (d-e) ref. [44] 11

Figure 1-4. (a) A time-dependent phononic crystal formed by a hexagonal lattice of acoustic trimers. The grey material represents the silicone rubber. (b) For each unit cell, the acoustic capacitance of each cavity is periodically modulated in a rotating fashion. (c, d) The degenerate dipolar lumped resonance (c) at 21.6 kHz and the next dipolar resonance (d) at 60 kHz. (e, f) Comparison between the bulk band structures in the absence and in the presence of modulation. (g) The boundary between two crystal domains with opposite modulation handedness makes a reconfigurable, backscattering immune and broadband nonreciprocal

waveguide, which perfectly transmits acoustic waves along the boundary, regardless of turns and defects. Reprint with permission from ref. [45] 13

Figure 1-5. (a) A schematic of the acoustic valley Hall insulator. (b) Dispersion relations for the gapless case of $\alpha = 0^\circ$ (black lines) and gapped cases of -10° (color lines). (c) Topological phase dependency with α where the inset shows the vortex features. (d) Dispersions for the interfaces separating two topologically identical (upper panel) and distinct (lower panel) AVH insulating phases. (e) Power transmission (black line) and reflection (red line) spectra for a zigzag path, where the inset shows the field distribution. (f) Transmitted pressure measured for the zigzag path (red circles), and a straight channel (black circles). Reprint with permission from ref. [65] 16

Figure 1-6. (a) Top and side views of the unit cell of acoustic honeycomb lattice. Two resonators play the role of artificial atoms connected by thin coupling waveguides. (b) Band diagram when a unit cell contains identical resonators (blue lines) and when the resonators are of different heights with $\Delta h = 0.15h$ (red lines). (c) Pressure field distribution for eigenstates K_1 and K_2 . (d) Topological transition as the height difference Δh changes from negative to positive. (e) Acoustic pressure field for a finite honeycomb lattice comprising 26×15 unit cells with a Z-shaped zigzag interface. The red arrow indicates the acoustic source. Reprint with permission from ref. [70] 17

Figure 1-7. Acoustic valley pseudospin states and topological mode inversion. (a) Schematics of the hexagonal lattice composed of perturbed three-legged rods (TLRs) embedded in an air matrix. (b) Symmetry breaking by rotating the rods attached to the computer-controlled electric motor. (c-e) Dispersion relations of the acoustic modes by reconfiguring the angle $\varphi = 30^\circ, 0^\circ, -30^\circ$. The symbols K_+ and K_- denote the pseudospin states. (f) Setup of the reconfigurable topological switch. The pedestals of the TLRs in the black region can be rotated to different angles. (g) The distributions of the pressure fields when switched between different topological states. Sound waves transmit through port 1 (port 2) at the rotation angle $-30^\circ(30^\circ)$ of the reconfigurable control region. Reprint with permission from ref. [67] 18

Figure 1-8. Schemes of the collision model and the D2Q9 velocity discretization model. Reprint with permission from ref. [78] 20

Figure 2-1. (a) The hexagonal lattice formed by acoustic double-trimer cell. Each trimer consists of three connected hollow circulators and rectangular channels, with air filled inside all the grey regions (inset: region A, B, C denotes different radius combination units). (b) Two types of double-trimer centrosymmetric cells with self-inward (upper structure) or self-outward (lower structure) radii-rotating modulation. (c) Two types of doubly degenerate dipolar resonances at 7970-8010 Hz corresponding to the configurations of upper and lower structures in (b). The colors from red to blue represent the values of pressure from positive maximum to negative maximum. (d) The tunable inner radius using modified spiral springs with lead rail. (e) Comparison between the band structure without (black curves, same radius in the trimer structure) and with (red dots) radius modulation. 29

Figure 2-2. The ratio of acoustic intensity (Output 3/Output 2) at different radius modulations in a single trimer (middle inset: trimer structure). The dimensions display the inner radius of every circulator in the trimer structure. The inner radius changes from 1.5 mm to a maximum of 8.0 mm. 31

Figure 2-3. (a) Acoustic band-structure diagram for a supercell composed of a 1-by-12 periodic array of double-trimer cells. Black dots refer to bulk modes, and blue dots refer to edge modes. (b) Acoustic pressure distribution for the dominant harmonic cells of an edge mode localized at the supercell centre. 34

Figure 2-4. (a) Immunity of the nonreciprocal edge mode to versatile edge geometries and sharp turns. (b) Reconfigurable and topologically protected one-way edge waveguide along the separating boundary and the robustness against defects. The self-inward radii-rotating modulation cell array is placed in the upper domain, while the self-outward modulation is placed in the lower domain. (c) Topological edge states with the opposite direction for the input source as of (b). The color legend displays the acoustic pressure. 36

Figure 3-1. Model configuration and pressure distribution. (a) Geometrical top view of cross-section at $H = 22 \text{ mm}$. The red region is specified as high temperature region is heated at a given temperature that is 373.15 K, 423.15 K, 473.15 K, 523.15 K, 573.15 K and 623.15 K, respectively. The rest blue area is set as a balanced temperature 273.15 K. (b) The acoustic pressure distribution in the condition of the optimal nonreciprocal performance with all the

dimensions labeled. The pressure distribution of the clockwise (c) and counterclockwise (d) dipole modes of the acoustic circulator corresponding to the azimuthal order to be $m=1$ 44

Figure 3-2. The contours and vectors of velocity field distributions in different temperatures. The high temperature region is set as (a) 373.15 K, (b) 423.15 K, (c) 473.15 K, (d) 523.15 K, (e) 573.15 K, (f) 623.15 K, respectively. The arrows show the velocity vectors. 45

Figure 3-3. Nonreciprocal performance in different temperatures and the comparison with experimental and theoretical results. (a) Transmission coefficients at different high temperatures for Port 2 (curves with lower peak values) and Port 3 (curves with higher peak values). (b) Comparison of normalized transmission among *Alu*'s experimental results[29], theoretical results (Eq. (3-6)) and the simulation results of the biasing velocity distribution induced by the applied high temperature at 623.15 K. 47

Figure 3-4. The velocity contours and nonreciprocal performance of acoustic circulators with four types of interior configurations, where temperature of the high temperature region is 523.15 K. The velocity contours and vector arrows for (a) Triangle structure. (b) Y-parallel triangles structure. (c) Hexagon structure. (d) Hexagram structure. (e) Transmission coefficients for Port 2 (curves with lower peak values) and Port 3 (curves with higher peak values). 50

Figure 4-1. (a) The hexagonal lattice of acoustic trimers. Each trimer is composed of three connected hollow circulators and rectangular channels. The inner media is air. (b) The periodically modulated and distributed acoustic impedance of each circulator, with the modulation scheme of 0°C , 90°C and 300°C throughout the double-trimer lattice. (c) A doubly degenerate dipolar resonance at 6.85-7 kHz. (d) The next resonant range, occurring at 8.6-8.85 kHz, due to one degenerate dipolar resonance. The colour legend denotes the acoustic pressure distribution. (e) Comparison between the band structure with (black curves) or without (red dots) modulation. 59

Figure 4-2. Normalized transmission coefficients of pressure at different temperature distributions in a single trimer (the upper left inserted trimer structure), as the temperature distribution of the acoustic input metamolecule remains is 0°C , while two outputs are shown in the above legend. Curves with same colour represents the output values in two output

ports, for the highest temperature output port relates to the upper curve (port 1) and the middle-high temperature output port relates to the lower curve (port 2)..... 62

Figure 4-3. (a) The simplified modulation scheme for two trimers in the double-trimer lattice are mirror symmetric with each other, as the colours of red, yellow and green represent acoustic impedances induced by the temperatures of $0\text{ }^{\circ}\text{C}$, $300\text{ }^{\circ}\text{C}$ and $90\text{ }^{\circ}\text{C}$, respectively. (b) The one-way edge transmission in the modulation scheme of (a), as the arrows show a lower transmission edge route. (c) The modulation scheme for every double-trimer lattice is not mirror symmetric, while the right trimer is anticlockwise rotating around the left trimer. (d) The edge transmission in the modulation scheme of (c), as the arrows also show an upper transmission edge route..... 63

Figure 5-1. Narrow channel geometry for acoustic wave propagation from the left to right side, exhibiting fully diffuse reflection on the upper and lower walls..... 74

Figure 5-2. Comparison between the simulation result and the analytical predictions of different slip models on attenuation coefficient for $\omega = 6 \times 108\text{ rad/s}$ 80

Figure 5-3. Comparison of the new second-order slip model, no-slip model and first-order slip model for the relative complex effective density..... 84

Figure 5-4. Comparison of the new second-order slip model, no-slip model and first-order slip model for the effective damping coefficient R' 85

Figure 5-5. Comparison of the new second-order slip model, no-slip model and first-order slip model for the relative effective acoustic speed..... 85

Figure 5-6. Comparison of the new second-order slip model, no-slip model and first-order slip model for the relative characteristic impedance..... 86

List of Abbreviations

<p>QHE..... quantum Hall effect</p> <p>QSHE.....quantum spin Hall effect</p> <p>QVHE..... quantum valley Hall effect</p> <p>QVH..... quantum valley Hall</p> <p>TKNN.....Thouless–Kohmoto– Nightingale–den Nijs</p> <p>SCs.....sonic crystals</p> <p>2D..... two-dimensional</p> <p>AVH.....acoustic valley-Hall</p> <p>TI.....topological insulator</p> <p>LBM..... lattice Boltzmann method</p> <p>FEM..... finite element method</p> <p>FDTD..... finite-difference time-domain</p> <p>DSMC.....direct simulation Monte Carlo</p> <p>CFD..... computational fluid dynamics</p>	<p>MEMS..... micro-electromechanical systems</p> <p>Kn.....Knudsen</p> <p>BGK..... Bhatnagar–Gross–Krook</p> <p>UGKS-DSMC.....unified gas-kinetic scheme DSMC</p> <p>IP-DSMC..... information preserving DSMC</p> <p>N-S equation..... Navier-Stokes equation</p> <p>LVDSMC.....Low-Variance Deviational Simulation Monte Carlo</p> <p>MD..... molecular dynamics</p> <p>VHS..... variable hard sphere</p> <p>HS..... hard sphere</p> <p>TMAC.....tangential momentum accommodation coefficient</p>
---	---

Chapter 1

1 Introduction to the airborne topological acoustics

Airborne topological acoustics have been investigated for around five years while tremendous efforts have been made to solve problems of topologically protected acoustic transmissions. Many ideas and methodologies, from condensed-matter physics, such as the QHE, the QSHE, and the QVHE etc., have been utilized and fully investigated to realize some potential applications, like information delivering, ultrasonic imaging, and noise reduction, etc. The theme of this thesis is to develop more practical topological acoustic properties applied in related devices or systems, including backscattering immune, tunable, broadband and miniaturized topological acoustic applications. Some detailed modulation strategies and controlling mechanisms have been fully investigated and developed, including importing air-induced flow field to mimic magnetic field in the QHE based system, metamaterial-type lattice array modification in the QSHE or QVHE based systems, and versatile acoustic properties based modulation model. This chapter will review the research background and recent efforts to investigate acoustic topological states in two- and three-dimensional systems, where the spin and valley degrees of freedom are utilized to control the acoustic transmission route in the form of unidirectional edge modes and defect-immune topological protected acoustics. The theoretical investigations and related experimental verifications are summarized based on the latest advancements in airborne topological acoustics, then the research challenges and objectives are identified.

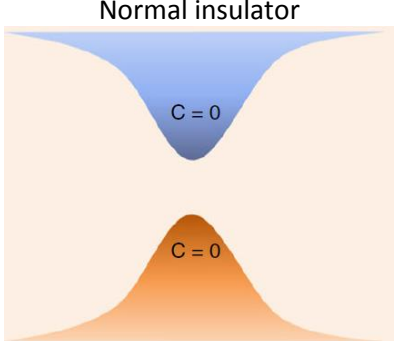
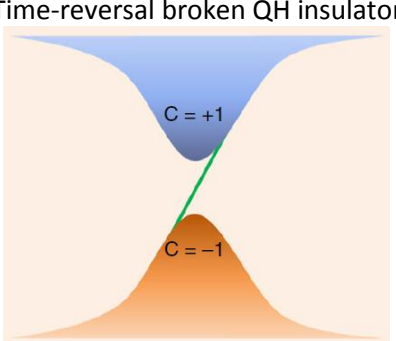
1.1 History and development of the QHE, QSHE and the QVHE in the condensed-matter system

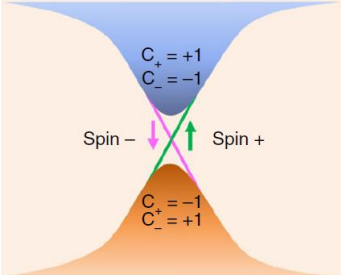
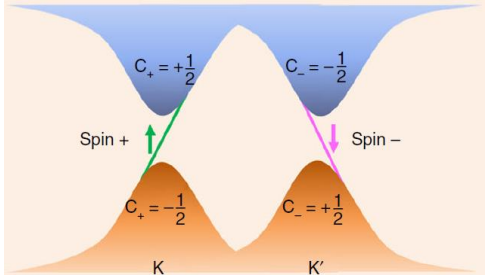
In a condensed-matter system[1], the specific phases of matter are characterized by the spontaneously broken underlying symmetries. These phases have differences in their symmetric properties[2] that cannot be smoothly interconnected by any path in parameter space. In 1980, Von Klitzing's discovery of the QHE[3] constructed an effective way to classify the phases of matter. The quantized Hall conductivity[4] was discovered when a 2D electron gas sample was disposed in a strong magnetic field with a low temperature, and was independent of impurities and sample size. The state used to describe this phenomenon was

switched to the notion of topological orders[4, 5], which characterize phases of matter beyond the symmetry breaking, thereby opening a new research branch in photonic/phononic waves[6], electromagnetic waves, and mechanical waves, etc.

Topological performance for phases of matter depends on the fundamental properties of the whole system and changes only under a transition state of quantum phase[7], and is insensitive to perturbations of material parameters. For the QHE, the quantization of the Hall conductivity originates from the fundamental non-trivial topological properties of the band structures. According to the Thouless–Kohmoto–Nightingale–den Nijs (TKNN) theory[5], the Chern number[8] is used to describe the non-zero topological invariant[9], and characterizes the Berry phase[10] accumulation over the Brillouin zone[11]. The value of the Chern number closely depends on the performance of the energy bands in the momentum space[12]. For electromagnetics, a periodic magnetic flux can be utilized to break the time-reversal symmetry of structures and produce a non-zero Chern number[13]. The resulting topologically non-trivial property[14-17] supports the existence of a gapless edge state[18] in the bulk band gap structure, exhibiting a special electronic property whereby electrons are conducted along the edge but insulated in the bulk of the structure. As shown in Table 1-1, this property is essentially different from a normal insulator with a zero Chern number.

Table 1-1. Schematic illustration of different topological phases

Topological phases		
Properties	Normal insulators exhibit band gaps, separating the conducting bands from the valence bands, characterized by the zero Chern number (a topological invariant).	A quantum Hall insulator can be realized by breaking time-reversal symmetry. It also has a band gap, which is spanned by a gapless edge state, exhibiting the electronic property that is conducting on the edge but insulating in the bulk. This phenomenon is characterized by the non-zero Chern number.

<p>Topological phases</p>	<p>Time-reversal-invariant QSH insulator</p> 	<p>Time-reversal-invariant QVH insulator</p> 
<p>Properties</p>	<p>The inherent spin-orbital coupling can also give rise to non-trivial topological states, known as the QSH insulators. A pair of gapless edge states emerges in the insulating band gap. The edge states carry conjugate electronic spins and exhibit spin-dependent propagation property. This is characterized by the spin Chern number (C_+ and C_-), while the total Chern number is zero, implying the intact time-reversal symmetry.</p>	<p>A discrete valley degree of freedom has also been proposed to realize topological states, known as the QVH insulators. Valley refers to the two energy extrema of the band structure in the momentum space, in which the Berry curvature exhibits opposite signs. Its integral over the whole Brillouin zone is zero, while the integral within each valley is nonzero. The system shows a valley-selective non-trivial property. The QVHE is characterized by the valley Chern number (C_+ and C_-). The total Chern number is also zero, hence the time reversal symmetry is intact.</p>

Later in 2005, the QSHE was proposed by Kane and Zhang et al[14, 16]. Beyond the effect of magnetic field, it was found that the inherent spin-orbit, coupled to the spin of the electron, can also create non-trivial topological phases, and a pair of gapless edge states exists in the insulating band gap. The edge states exhibit conjugate electronic spins[19] and spin-based propagation property, as shown in Table 1-1. In the QSHE, the total Hall conductivity and the Chern number are zero, implying that the time-reversal symmetry remains intact, which is the reason for protecting the spin-based edge states. The separating spin Hall conductivity is non-zero despite the fact that the total Hall conductivity is zero, and can be described by the spin Chern number[20].

Recently, a valley state with another discrete degree of freedom was investigated to achieve a topological state, and is known as the QVHE in valleytronics[21, 22]. The valley state denotes the two extrema of the energy band structure in the momentum space, and its Berry curvature[23] exhibits opposite numbers in the separating band regions. The integral of the full Brillouin zone is calculated as zero, while the integral within the separating valley is

nonzero. As a result, the whole QVHE system shows a valley-selective topologically non-trivial property, and also retains the intact time-reversal symmetry. Although the nature of the aforementioned topological phases differs, they share the same properties in that the edge states crosslink the bulk band gap and even separate band domains with different Chern numbers.

Different types of topological states and their associated properties can introduce many potential applications for the next generation of topological quantum computing[24-26] and electronic devices. However, in real electronic applications, realizing topological states remains challenging based on the existence of the inevitable material defects and the validity of the single electron approximation. As a result, utilizations of topological states have been extended to the research of phononic and photonic systems[27], taking advantage of their large scale in both space and time. These advantages make the fabrication and measurement process more accurate and much easier to realize compared to electronic systems. Additionally, as the phononic/photonic systems[27] are normally not restricted by the Fermi level (the thermodynamic work required to add one electron to the body), so many appropriate methods and strategies can be of interest in thorough investigations. Nevertheless, many challenges lie in emulating the topological states in the condensed-matter system given the classical wave regime, due to the mechanism difference between the electron and the phonon/photon. For example, phonon/photon systems cannot directly interact with the magnetic field as they are unable to carry a half-integer spin[28], so that these systems often require additional efforts to break the time-reversal symmetry. In the search for topological states of matter, the difference between bosons[29] and fermions[30] can also inspire potential applications in the investigation of low loss phononic/photonic devices. Compared to photonic systems, acoustic systems differ substantially since acoustic wave lacks a degree of freedom for transverse polarization that can be utilized to construct pseudo spins, which mimic the spin-up and spin-down modes in electronic systems. Acoustic systems often require additional complexities to break the time-reversal symmetry, which is one key factor in mimicking the quantum effects and in realizing topologically robust acoustic propagation.

The following paragraphs in the introduction offer some recent detailed advances in topological states in the airborne acoustic wave regime. The specific organization of the content is as follows: first, the origins of the analogous QHE for acoustics are introduced to obtain nonreciprocal or topological performance, followed by the main breakthroughs in the analogous QSHE used in acoustic systems. Then, recent developments in the analogous QVHE are provided and discussed. Some basic principles and mechanisms that can effectively clarify the acoustic transmission mechanism in micro- and nanochannels are introduced to investigate the topological acoustics in ultrasonic or in a micro- or nanostructure to realize miniaturization. The last section discusses the perspectives on existing challenges and my objectives in this investigation of airborne topological acoustics.

1.2 Acoustic analogues of the QHE for the airborne nonreciprocal acoustics and topological acoustics

The topological phases of matter were first exemplified by the QHE, exhibiting the phenomenon of an insulator in the metal bulk while a conductor along the structure edges, where the electrons transmit unidirectionally without dissipation and backscattering. The associated Hall conductivity is quantized as $\sigma_{xy} = Ce^2/h$, which is not affected by material impurities. Here, C is the Chern number, e is the charge of one electron, and h denotes the Plank constant. The characterized topology of the electronic functions in the momentum space is independent of the constructed material properties[4, 5], which leads to topological robustness against impurities. In a 2D system, the Chern number is calculated by,

$$C = \frac{1}{2\pi} \int F(\mathbf{k}) \cdot d\mathbf{s} \quad (1-1)$$

where $F(\mathbf{k}) = \nabla_{\mathbf{k}} \times A(\mathbf{k})$ represents the Berry curvature and $A(\mathbf{k}) = \langle u_n(\mathbf{k}) | i\nabla_{\mathbf{k}} | u_n(\mathbf{k}) \rangle$ is defined as the Berry connection. $u_n(\mathbf{k})$ is the periodic part of the Bloch state for the n th energy band of the momentum \mathbf{k} . In the condition of symmetric operation, the Berry curvature obeys the definitions of $TF(\mathbf{k}) = -F(-\mathbf{k})$ and $PF(\mathbf{k}) = F(-\mathbf{k})$, where T and P represent the time-reversal and parity operators, respectively. Breaking T symmetry but retaining the P symmetry, the integral over the whole Brillouin zone makes the Chern number a non-zero value. For the QHE, the zero Chern number corresponds to a topological trivial state while the non-zero Chern number corresponds to a topological non-trivial state.

The topological states with the non-zero Chern number display special wave transmission properties of unidirectional edge transmission and immunity to impurities, which have potential in the next-generation of quantum computing and electronic devices.

Inspired by the development of electronic systems, the concept of topological state with the QHE was quickly utilized in the analogous classical acoustic realms. Generally, breaking the T symmetry is challenging, usually requiring extraordinary complexities, such as importing nonlinearity or utilizing magneto-acoustic materials. These possible methods either introduce inherent signal distortion or require impractically large volume. Then in 2014, inspired by an investigation utilizing magnetic bias to create electromagnetic nonreciprocity in gyromagnetic materials, Fleury et al. proposed an effective method of using rotating airflow to break the T symmetry in acoustic C_{3v} symmetric ring cavities[31]. As shown in Figure 1-1(a-b), the imparted fan-induced airflow, replacing the role of magnetic bias, splits degenerate modes of the two counter-propagating azimuthal ring resonators and introduces acoustic nonreciprocity. The nonreciprocal performance is good around the dipolar resonant frequency. Specifically, for the QHE-based topological acoustics, the acoustic transmission equation in a circumstance of the background airflow is,

$$\left[(\nabla - i\mathbf{A}_{eff})^2 + \frac{w^2}{c^2} + \left(\frac{\nabla \rho}{2\rho} \right)^2 - \frac{\nabla^2 \rho}{2\rho} \right] \phi = 0 \quad (1-2)$$

where w is the angular frequency, c is the acoustic speed, ϕ is the velocity potential, and ρ is the mass density of air. The effective vector potential $\mathbf{A}_{eff} = -w\mathbf{V}/c^2$ generates the effective magnetic field $\mathbf{B}_{eff} = \nabla \times \mathbf{A}_{eff}$ that can break the T symmetry, and \mathbf{V} is the background velocity field. The equation (1-2) denotes the acoustic transmission mechanism with airflow.

Based on the method of introducing external flow field, many designs of the analogous QHE in sonic crystal systems to achieve topological performance have been provided[32-36]. In Figure 1-1(c-d), the hexagonal acoustic lattice and the honeycomb lattice both display the imported circulating fluid flow can be used to break the T symmetry. Due to the intrinsic symmetry of lattice structures, a pair of Dirac-like points emerges at the boundary of the Brillouin zone[37-39] when $\mathbf{V} = 0$. In contrast, when the external airflow is introduced, the Dirac-like point degeneracies are lifted to create a finite complete band gap by breaking the T

symmetry, which is characterized by an opened band gap. The calculated Chern number for the two separating bands obtains non-zero values ($C = \pm 1$), which implies the systems are in the topological non-trivial states. Some topological performance of one-way edge transmission along boundaries, even truncated by the lattice with topologically trivial states and unidirectional behaviors immune to structure defects and sharp bends, are demonstrated in the lower part of Figure 1-1(c-d).

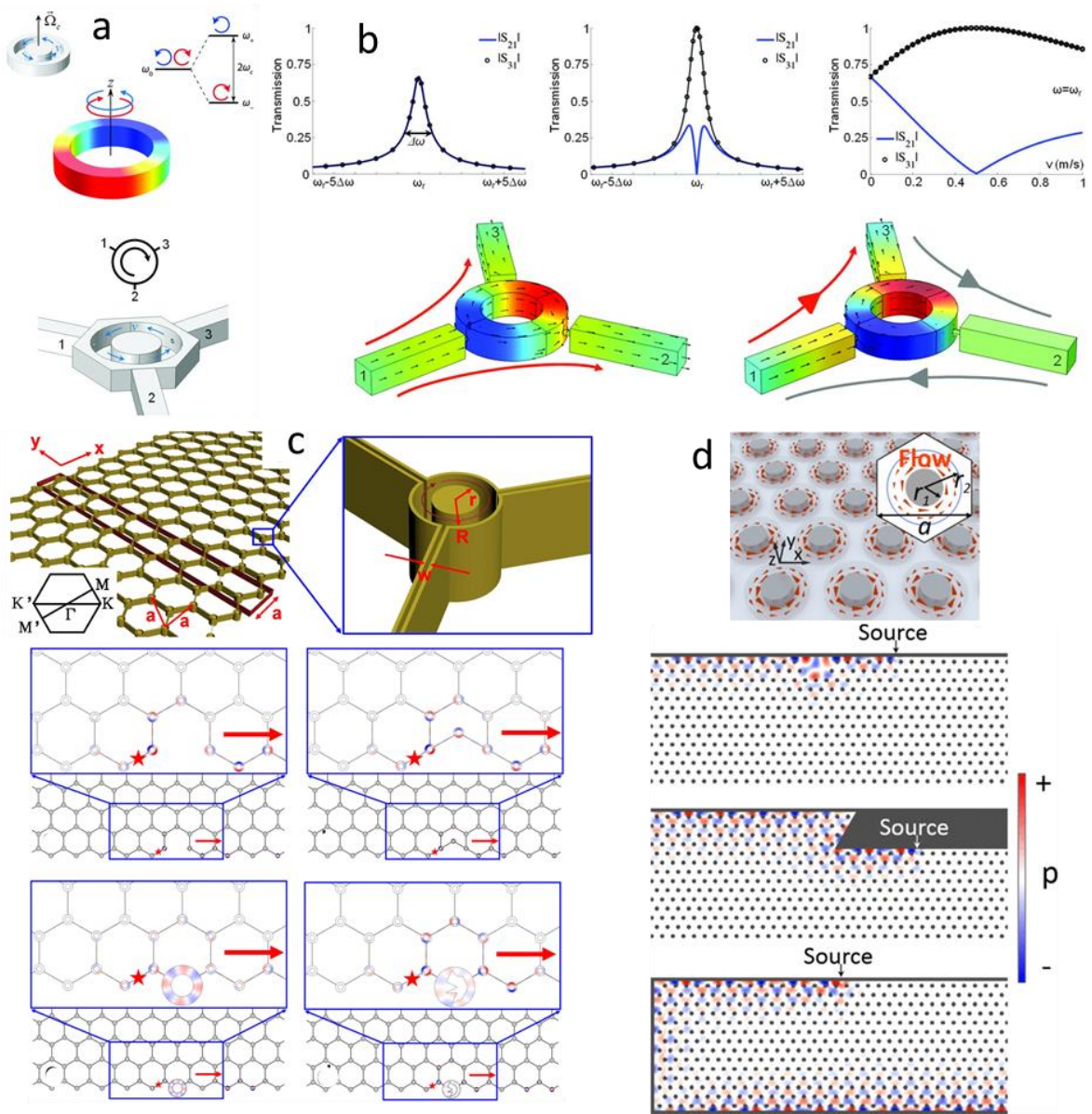


Figure 1-1. The analogous QHE in sonic crystal systems. (a-b) The fan-induced-airflow acoustic circulator and its nonreciprocal performance. (c) The hexagonal acoustic

lattice incorporated with circulating airflow is presented, and has topological performance against the structure disorder and defects. (d) The honeycomb acoustic lattice with rotating airflow, and the robust edge state transmission against various defects. Reprint with permission from: (a-b) ref.[31], (c) ref. [32], (d) ref. [33].

A few more studies have proceeded based on the QHE. For experimental implementation, the design of uniform flow biased circulators often imposes serious challenges. Zhu et al. used a chiral-structured rotor coupling with ring resonators to realize high-order whispering gallery modes with a high Q factor[40]. This design makes the acoustic system produce a stable and uniform airflow, and achieves good acoustic nonreciprocity even at low rotating airflow speeds. Chen et al. designed a C_{4v} symmetric circulator by considering different rectangular waveguide sizes and tunable rotating airflow velocities[35]. The resulted adjustable topology of the band gap enriched the use of acoustic topological insulators.

1.3 Acoustic analogues of the QSHE for the airborne topological acoustics

Naturally, in addition to acoustic analogues of the QHE that require breaking T symmetry, exploiting the QSHE to investigate topological states under preserved T symmetry is proposed. The band structure of the QSHE can be considered a combination of two coupled Quantum Hall States. Differently, the spin-orbit coupling dominates in the QSHE where the coupling between orbital angular momentum and spin makes the moving electrons exert a spin-dependent force, even without magnetic materials and an electromagnetic field. As a result, the electrons with spin up and spin down angular momenta transmit in opposite directions along the state edges. The spin Chern number is used to describe the corresponding topological order as[41],

$$C_{\pm} = \frac{1}{2\pi} \int F_{\pm}(\mathbf{k}) \cdot d\mathbf{s} \quad (1-3)$$

where $F_{\pm}(\mathbf{k}) = \nabla_{\mathbf{k}} \times \langle u_{\pm}(\mathbf{k}) | i\nabla_{\mathbf{k}} | u_{\pm}(\mathbf{k}) \rangle$ represents the Berry curvature. The electron Bloch states are decomposed into two parts, $u_{+}(\mathbf{k})$ and $u_{-}(\mathbf{k})$, representing the spin up and spin down components, respectively. The true topological invariants defined in equation (1-3) make the QSHE-based topological systems robust against structure disorder or defects,

including different types of spin symmetry-breaking perturbations. Any non-magnetic impurities will not remove the existence of metallic edge states, as electrons are not completely reflected when scattered, even in stronger impurities.

The QSHE with the spin-locked and T symmetry protected edge states can find its counterparts in phononics, which require the pseudo T symmetry and fermion-like pseudo spins. However, as the airborne acoustic wave only propagates longitudinally, the lack of various polarizations makes it challenging to realize analogous QSHE. One existing solution was provided by using coupled resonator lattices that support anticlockwise and clockwise resonant modes, which take the role of pseudo spins[42, 43]. Figure 1-2 shows a cell of the 2D coupled metamaterial ring lattice, consisting of one central lattice and four surrounding coupling lattice rings[42]. The sufficiently large coupling strength defines the pseudo-spin modes of acoustics, and the topological edge state depends on wave circulation directions constructed in the lattice rings. The designed lattice configurations, like the pseudo-spin-up clockwise mode and the pseudo-spin-down anticlockwise mode[44], support the pseudo-spin dependent edge states and realize the scattering immune to sharp boundary turns or lattice dislocations. The edge states with different pseudo-spin modes are decoupled given the existence of the homogenous coupling between neighboring rings, and close the time-reversed channels due to backscattering. The rings of the designed structure no longer act as resonators and the mode of the edge state is considered a conventional waveguide mode. As shown in Figure 1-2, when the coupling strength between two adjacent lattice rings outstrips a threshold, any acoustic wave holding a pseudo-spin in a lattice ring can tunnel into neighboring coupling rings with a flipped pseudo-spin mode, then transfers to another lattice ring with the pseudo-spin reserved, leading to the formation of an interesting zigzag route.

Recently, another method utilizing two degenerate Bloch modes to induce the pseudo spin states, instead of taking two polarizations of two resonant modes, was proposed[45]. Specifically, as shown in Figure 1-3(a-c), by expanding a primitive small unit cell into a larger unit cell, the Dirac-like cones in K and K' points existing in the primitive Brillouin zone are folded into the Γ point of the new Brillouin zone, which forms the doubly degenerate Dirac-like cones. By tuning the geometric parameters of lattice structures, a band inversion can be found close to the degenerate point, which can be characterized as the

topological transition. The scalar acoustic modes display electronic orbital d-like and p-like wave shapes, which correspond to the spin-down and up states. Simply adjusting the intermolecular coupling strength by expanding or contracting the hexagonal resonator lattice can create band inversion between the pseudospin dipole mode and quadrupole mode, and thereby realize configurable one-way transmissions and topologically protected edge states.

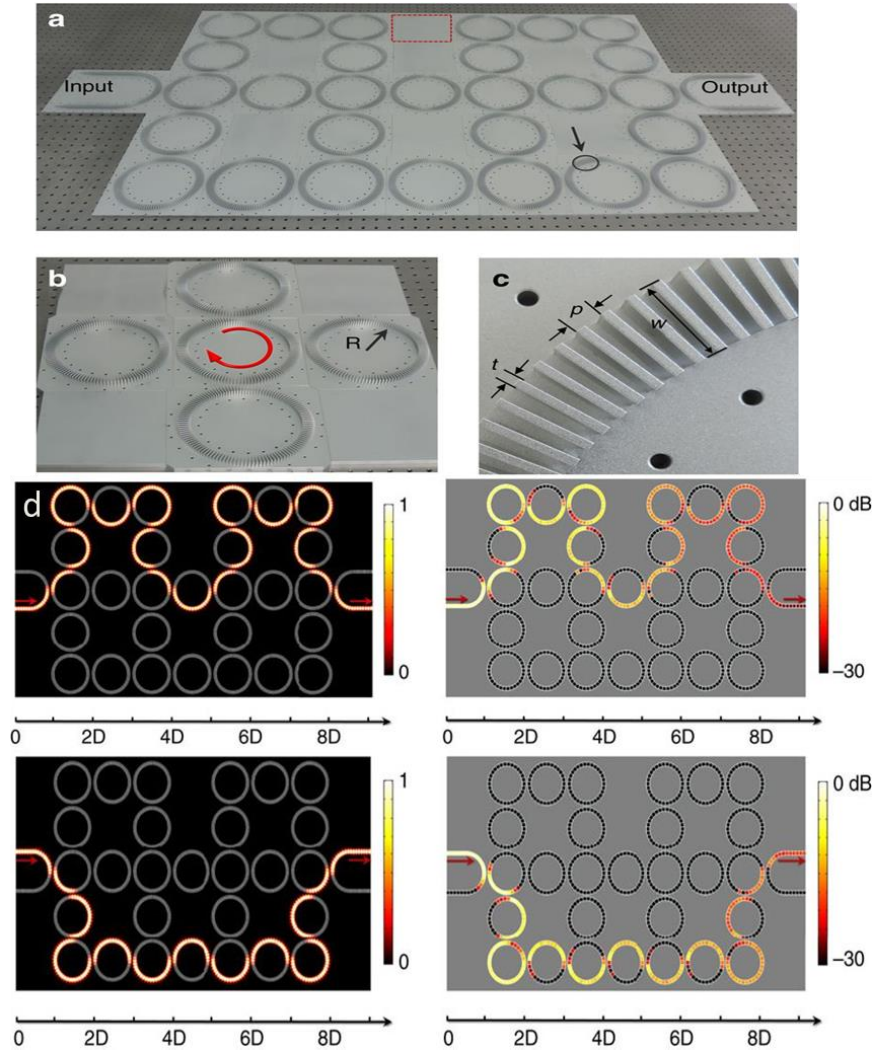


Figure 1-2. (a) Photograph of a 2D coupled metamaterial ring lattice system. The U-shape waveguides are the input and output ports with specific pseudo-spins. (b) Photograph of one lattice ring surrounded by four coupling rings. The red arrow shows that the wave is carrying pseudo-spin-up, *viz.* propagating in clockwise. (c) Details of the metamaterial waveguide. (d) The simulated and experimental pressure amplitude distributions when pseudo-spin-up and pseudo-spin-down acoustic one-way edge states

are excited, showing the robustness of the edge states against the sharp bending.

Reprint with permission from ref. [42]

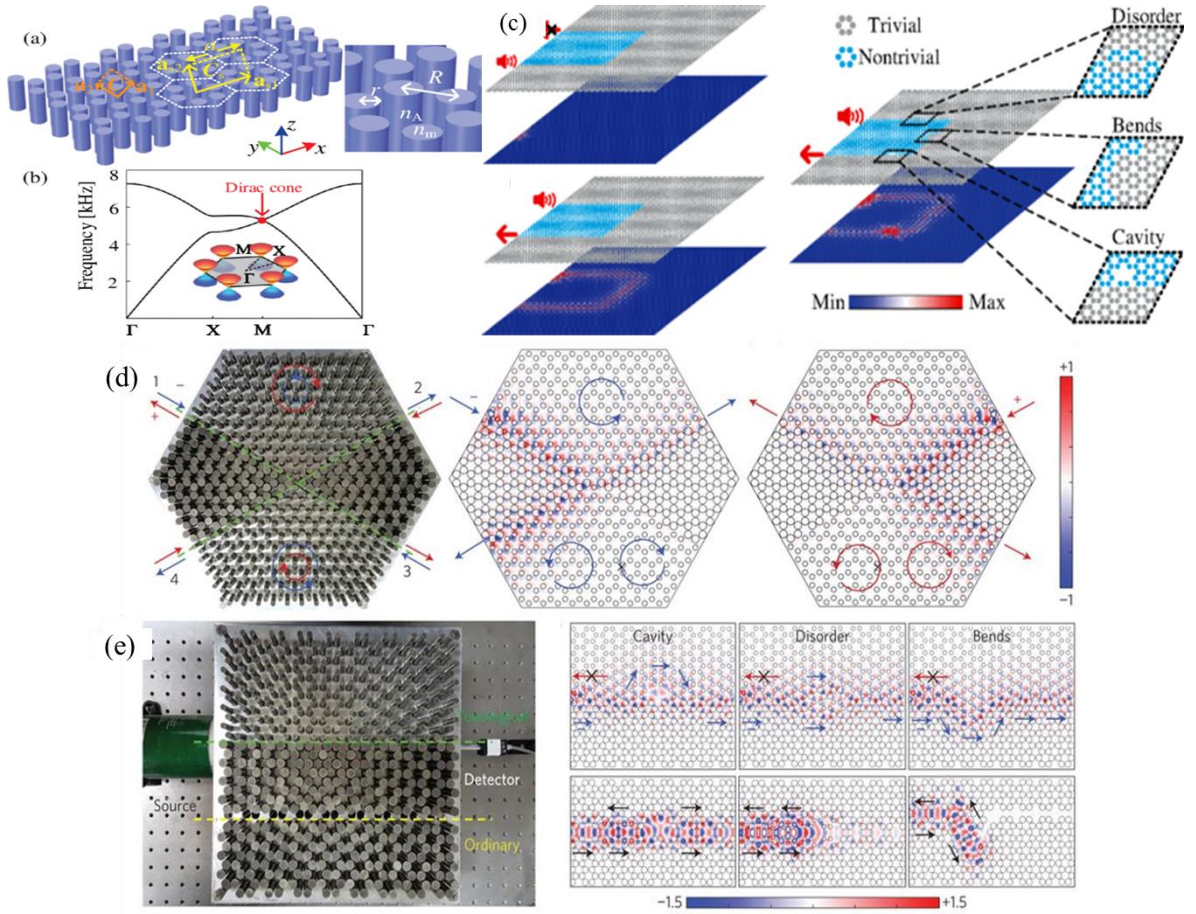


Figure 1-3. (a) Schematic of the hexagonal acoustic metamaterial lattice composed of artificial metamolecules. (b) Dispersion relation of the lattice based on the original unit cell for single Dirac cones at the 1st BZ corners. (c) Topologically protected one-way edge waveguide for airborne acoustics and the corresponding acoustic intensity fields. The pseudospin-down mode is excited at the lower and upper edge, and the topological edge states with three types of defects: cavity, disorder, and bends. (d) The spin-locked edge state propagation. (e) Robustness against versatile defects. Reprint with permission from: (a-c) ref. [45] (d-e) ref. [46]

Specifically, as shown in Figure 1-3(d-e), based on the principle of accidental degeneracy[46], the acoustic analogous QSHE is realized by a honeycomb lattice consisting of steel rods in air. The C_{6v} symmetric honeycomb lattice supports two pairs of degeneracies

at the Γ point, including the dipolar modes p_x/p_y and the quadrupolar mode $d_{x^2-y^2}/d_{xy}$, which can interchange to emulate different pseudo spin states. By decreasing the volume ratio of the steel rods, the pair of dipolar modes that are separated by the band gap will exchange their positions as the movement of frequency, and the same phenomenon will happen in the pair of quadrupolar modes as the band inversion. In the middle of this transition process, there is a state where the band gap closes and the two bands would touch together, forming the doubly degenerate Dirac-like cones. This gap opening, closing and reopening process characterizes a topological transition from the ordinary (trivial) state to the topological state (non-trivial) state. In the acoustic topological state, a pair of edge states emerges to carry opposite group velocities to mimic the spin-up and down states. Correspondingly, the spin-dependent acoustic transmission depicted in Figure 1-3(d). Further investigation in Figure 1-3(e) reveals that the spin-locked edge state transmission is robust against cavities, bends, and disorders.

Moreover, as shown in Figure 1-4, Fleury et al. introduced[47] one fluidic acoustic topological system whose lattices are modulated in a time-harmonic rotating strategy, as a change in space and time, demonstrating the Floquet topological insulators[48-53] for acoustic analogues. This proposal is based on an on-site rotating modulation scheme compressing the volume of each cavity cell using a piezoelectric actuator, and the phase-uniform lattice is not requested. The imparted acoustic capacitance modulation creates an effective spin on each trimer unit to equivalently break the time-reversal symmetry. Modulations up to tens of percents are available using suitable actuating strategies, which make possible topologically protected, broadband and unidirectional acoustic devices. This work also realizes the applications of an ultra-broadband acoustic diode and a topologically protected acoustic emitter. All the aforementioned properties make the QSHE-based acoustic designs have potential in developing chip-scale acoustic devices.

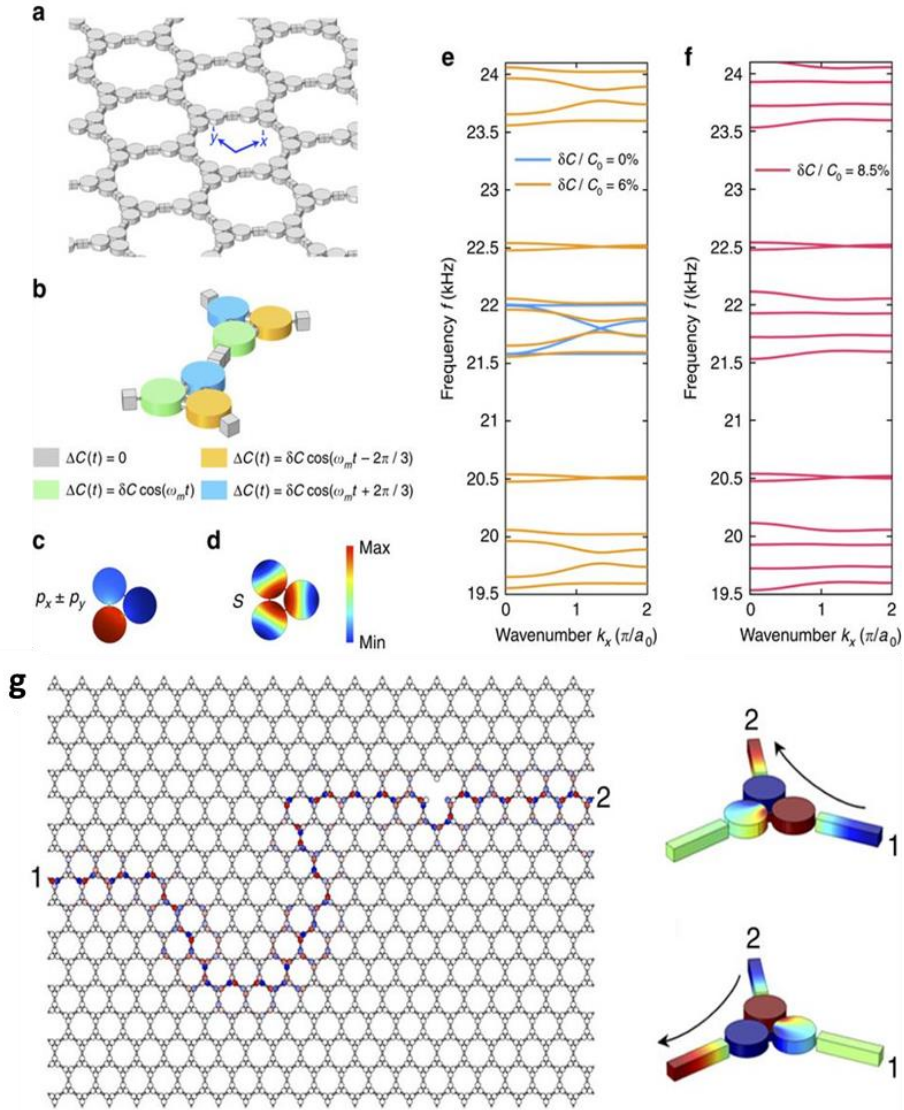


Figure 1-4. (a) A time-dependent phononic crystal formed by a hexagonal lattice of acoustic trimers. The grey material represents the silicone rubber. (b) For each unit cell, the acoustic capacitance of each cavity is periodically modulated in a rotating fashion. (c, d) The degenerate dipolar lumped resonance (c) at 21.6 kHz and the next dipolar resonance (d) at 60 kHz. (e, f) Comparison between the bulk band structures in the absence and in the presence of modulation. (g) The boundary between two crystal domains with opposite modulation handedness makes a reconfigurable, backscattering immune and broadband nonreciprocal waveguide, which perfectly transmits acoustic waves along the boundary, regardless of turns and defects. Reprint with permission from ref. [47]

1.4 Acoustic analogues of the QVHE for the airborne topological acoustics

Most recently, the discrete valley degree of freedom[54-58], characterizing as quantum states of energy extrema in the momentum space, due to its great potential as a new method of information carrier, is attracting increasing attention. This is also considered as the valley pseudospin, which has been widely observed in 2D crystals and conventional semiconductors. The intervalley scattering barely occurs as the existence of the large separation in the momentum space, and it means that the valley can be considered as a good index to characterize the quantum states. The existence of valley-like frequency dispersions can transfer the valley concept to the classical wave system, as the similarity of classical waves in periodic structures, these dispersions have been realized in photonic crystals[59-63] and SCs[37, 64]. Based on the QVHE[65, 66], the corresponding valley-protected edge states[67-73] were theoretically and experimentally investigated in 2D acoustic systems.

In 2016, Lu et al.[65, 67] firstly introduced valley states of SCs for acoustics. As shown in Figure 1-5, the hexagonal SC lattice consists of solid triangular rods constrained in a 2D waveguide, and its symmetric property can be denoted by the rotation angle α . At the corners of the 1st Brillouin zone, the existence of a two-fold Dirac degeneracy for any SC with $\alpha = n\pi/3$ is preserved by the C_{3v} symmetry, while the degeneracy would be lifted by any other rod rotation angle if the mirror symmetries[64] are broken. The dispersion relations for the SCs with $\alpha = 0^\circ$ and $\alpha = -10^\circ$ are shown in Figure 1-5(b). The vortex revolution of the clockwise mode and anticlockwise mode at each valley characterizes the valley degree of freedom in this 2D acoustic system, as shown in Figure 1-5(c). The tuning of the acoustic valley-Hall (AVH) phase transition in a SC structure is adjusted by the rotating angle α . When $\alpha < 0^\circ$, the vortex chirality of the upper (lower) state corresponds to anticlockwise (clockwise) mode, which is strictly inverted when $\alpha > 0^\circ$. The AVH phase transition accompanied by the inversion of two pseudo spin states can be characterized by the α -dependent continuum Hamiltonian. Based on the $\mathbf{k} \cdot \mathbf{p}$ perturbation method, the unperturbed Hamiltonian $H(\mathbf{k}_\perp) \equiv H_0(\delta\mathbf{k})$ close to Dirac points can be calculated as[14, 74] $H_0(\delta\mathbf{k}) = v_D(\delta k_x \sigma_x + \delta k_y \sigma_y)$, where v_D is the group velocity, $\delta\mathbf{k} = (\delta k_x, \delta k_y) \equiv \mathbf{k}_\perp - \mathbf{k}_D$ denotes

the distance difference of K and K' points as $\mathbf{k}_D = \pm \frac{4\pi}{3\alpha_0} e_x$, and σ_x, σ_y are Pauli matrices of the vortex pseudo spins. The perturbation Hamiltonian is diagonalized with $H_P = mv_D^2 \sigma_z$. The +/- sign of the effective mass $m = (w_{q^+} - w_{q^-})/2v_D^2$ means two different types of AVH insulators are separated by the Dirac semi-metal phase, and takes $m=0$ in the phase diagram. In the first Brillouin zone, the massive Dirac Hamiltonian δH imports a non-trivial Berry curvature $\Omega_K(\delta\mathbf{k}) = \frac{mv_D}{2(\delta k^2 + m^3 v_D^2)^{3/2}}$. The time-reversal symmetry is corresponding to the zero Chern number, which is the Berry curvature integral over the whole Brillouin zone. If the Berry curvature integral over one half of the Brillouin zone for an individual valley is accurately calculated, the non-zero valley Chern number can be defined as[75] $C_K = \text{sgn}(m)/2$. As a result, the difference for the topological order over the interface is quantized, which maintains a chiral edge mode in the bulk-boundary correspondence[76]. Two different SC interfaces were studied to verify this, one is constructed by $\alpha = 10^\circ$ and 50° SCs, while the other is constructed by $\alpha = -10^\circ$ and 10° SCs, as the detailed dispersion relation is correspond to the top panel and bottom panel of Figure 1-5(d), respectively. For the configuration of the top panel, the band structure is completely gapped due to the existence of identical valley-Hall states within the SC lattice. For the bottom panel, topological edge states lie within the bulk band gap as shown by the green lines, which are based on the AVH phase inversion crossing the interface. Similar to the acoustic analogues of the QSHE, the topological edge states associated with the acoustic analogues of the QVHE also emerge robustly against crystal bends and defects. Figure 1-5(e-f) also shows an immune backscattering transmission of the topological valley edge mode[69, 74] along the interface separating two different sharp bends, even though the lattice obstacles and defects induce inter-valley scattering transmission.

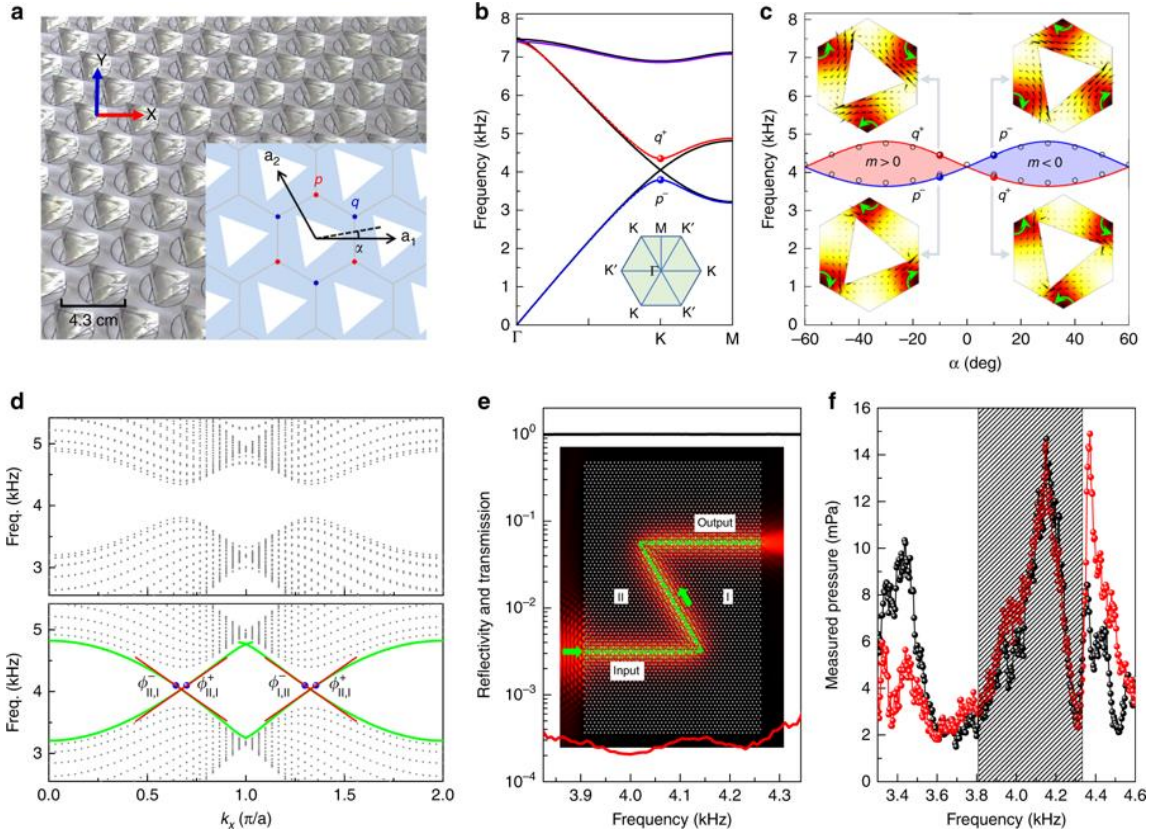


Figure 1-5. (a) A schematic of the acoustic valley Hall insulator. (b) Dispersion relations for the gapless case of $\alpha = 0^\circ$ (black lines) and gapped cases of -10° (color lines). (c) Topological phase dependency with α where the inset shows the vortex features. (d) Dispersions for the interfaces separating two topologically identical (upper panel) and distinct (lower panel) AVH insulating phases. (e) Power transmission (black line) and reflection (red line) spectra for a zigzag path, where the inset shows the field distribution. (f) Transmitted pressure measured for the zigzag path (red circles), and a straight channel (black circles). Reprint with permission from ref. [67]

Yang et al.[72] designed a periodic acoustic resonator system that can be considered as an acoustic analogue of a gapped graphene monolayer. The designed honeycomb acoustic lattice consisting of circulators is described with a simple nearest-neighbor tight-binding model, and the height of the circulator is tuned periodically to emulate the acoustic counterpart of the QVH topological insulator. As the heights change in the adjacent two resonators, the band gap remains unchanged while the band inversion will emerge. As shown in Figure 1-6, a zigzag domain wall separated by different modulation domains with opposite valley Chern

numbers is characterized as gapless topological valley edge states, while an armchair domain wall is characterized as gapped edge states. Moreover, the valley vortex states in this acoustic resonator system analogously rotate around six atoms as an π orbit configuration in the graphene, rather than valley vortex existing in the space among the adjacent sites.

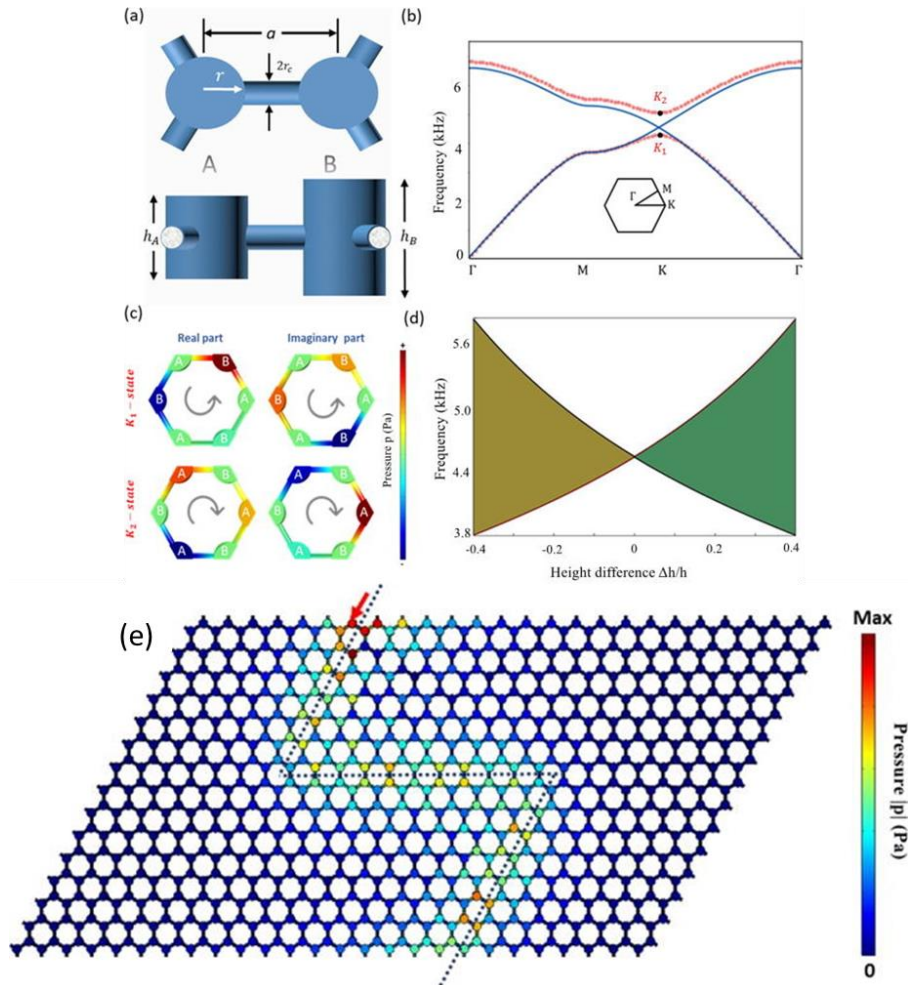


Figure 1-6. (a) Top and side views of the unit cell of acoustic honeycomb lattice. Two resonators play the role of artificial atoms connected by thin coupling waveguides. (b) Band diagram when a unit cell contains identical resonators (blue lines) and when the resonators are of different heights with $\Delta h = 0.15h$ (red lines). (c) Pressure field distribution for eigenstates K_1 and K_2 . (d) Topological transition as the height difference Δh changes from negative to positive. (e) Acoustic pressure field for a finite honeycomb lattice comprising 26×15 unit cells with a Z-shaped zigzag interface. The red arrow indicates the acoustic source. Reprint with permission from ref. [72]

Zhang et al.[69] experimentally realized acoustic topologically protected adjustable edge states using three-legged epoxy resin rods, and the formed phononic TI is based on valley pseudospin without introducing external bias. Three-legged rods are arranged to construct a triangular lattice, which is tuned by the computer-controlled motors. Specifically, each of the rods can be rotated independently enabling flexible switching between trivial and non-trivial configurations. This design provides a robust and versatile approach towards manipulating acoustic transmission route without back reflection. Moreover, the broad frequency response of the tunable acoustic transmission has been utilized to design acoustic delay lines, which has the potential for acoustic applications of pulse processing and signal buffering.

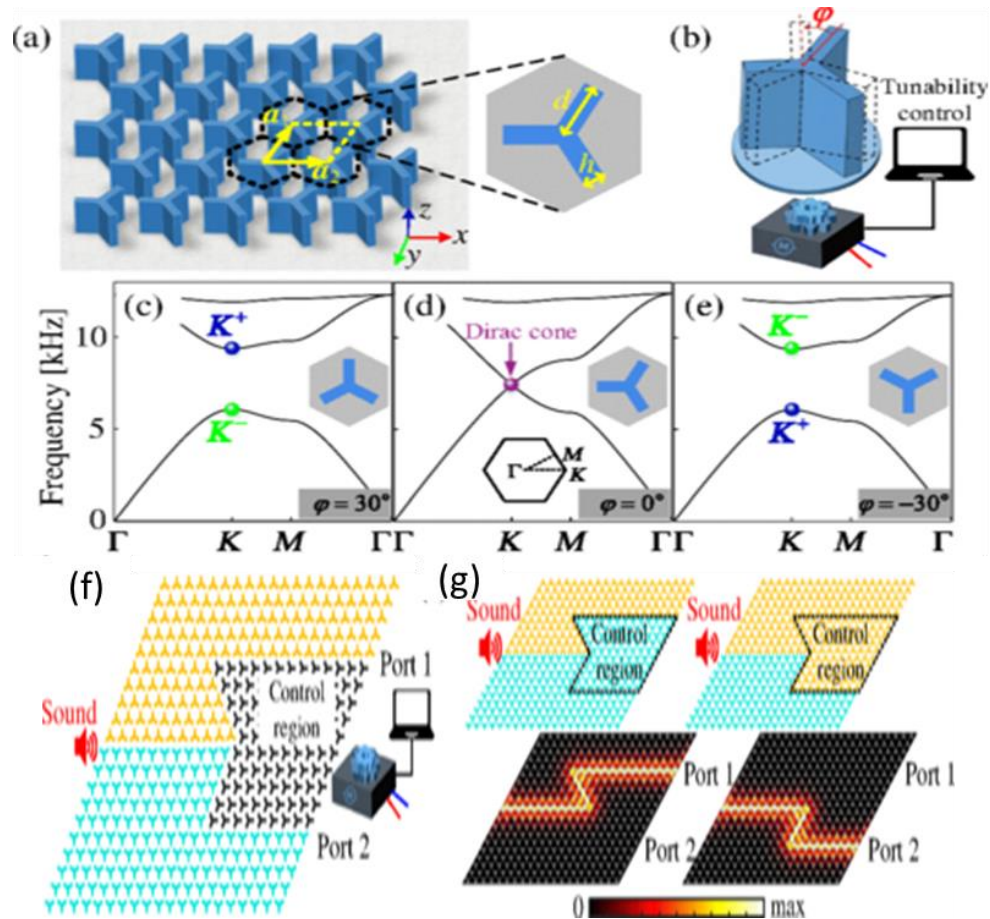


Figure 1-7. Acoustic valley pseudospin states and topological mode inversion.

(a) Schematics of the hexagonal lattice composed of perturbed three-legged rods (TLRs) embedded in an air matrix. (b) Symmetry breaking by rotating the rods attached to the computer-controlled electric motor. (c-e) Dispersion relations of the acoustic modes by

reconfiguring the angle $\varphi = 30^\circ, 0^\circ, -30^\circ$. The symbols K^+ and K^- denote the pseudospin states. (f) Setup of the reconfigurable topological switch. The pedestals of the TLRs in the black region can be rotated to different angles. (g) The distributions of the pressure fields when switched between different topological states. Sound waves transmit through port 1 (port 2) at the rotation angle $-30^\circ(30^\circ)$ of the reconfigurable control region. Reprint with permission from ref. [69]

1.5 Lattice Boltzmann method and DSMC method for the miniaturization of topological acoustics

An analytical model that can effectively predict the acoustic transmission mechanism in micro- and nanochannels is important to future research into topological acoustics in ultrasonics or in a small structure so as to realize miniaturization. The major challenges of micro-nano scale acoustic transmission are mainly due to the unknown mechanisms in this discontinuous medium, and the difficulty of fabricating effective physical devices for experimental measurement. Therefore, numerical methods may become necessary tools to further investigate this issue. While there are a variety of numerical methods dealing with acoustic propagating problems, including the finite element method (FEM) and finite-difference time-domain (FDTD) method, few of them have proven to be effective at micro-nano scales. Among them, the use of the lattice Boltzmann method (LBM) has shown great feasibility and potential in studying micro-nano acoustic transmission issues.

The LBM[77, 78] was first introduced to investigate gas flow and proved to be an effective tool to avoid certain weaknesses in lattice gases, while retaining their distinct advantages: parallelization and simplicity. Instead of handling a single particle, the LBM handles particle distribution probability using statistical methods to compute the macroscopic parameters of the whole system. The reason for the LBM's simple parallelization lies in the fact that the operations on the grids are local, so that each node can be updated independently of others.

The application of LBM in micro-nano scale acoustic transmissions was first proposed by McNamara and Zanetti[79]. The mechanism of particle collision and transferring process of LBM are also applicable in micro-nano acoustic transmissions, which should consider propagation in a discontinuous medium, as in essence, the airborne acoustic wave

propagating is the result of air molecule movement. For monocomponent gas, the distribution function of the particle is denoted as f , which is a function of space location vector $r(x,y,z)$, particle velocity vector $\xi (\xi_x, \xi_y, \xi_z)$ and time t . Assuming ma to be an external force exerted on every particle, then during every time step dt , if no collision occurs:

$$f(\mathbf{r} + d\mathbf{r}, \xi + \mathbf{a}dt, t + dt)d\mathbf{r}d\xi = f(\mathbf{r}, \xi, t)d\mathbf{r}d\xi \quad (1-4)$$

Employing the Taylor expansion, and considering the change of particle number in collision, that is, $(\frac{\partial f}{\partial t})_{collision}d\mathbf{r}d\xi dt$, then yields:

$$(\frac{\partial f}{\partial t})_{collision} = \frac{\partial f}{\partial t} + \xi \cdot \frac{\partial f}{\partial \mathbf{r}} + \mathbf{a} \cdot \frac{\partial f}{\partial \xi} \quad (1-5)$$

The collision process denotes particle diameter as dD , particle velocities before and after collision as ξ_1, ξ_2 and ξ'_1, ξ'_2 , and considers the whole collision process elastic. Therefore, after considering momentum conservation, energy conservation and the increment of particles during the collision process, the final distribution function f , that is, the Boltzmann equation, can be expressed as:

$$\frac{\partial f}{\partial t} + \xi \cdot \frac{\partial f}{\partial \mathbf{r}} + \mathbf{a} \cdot \frac{\partial f}{\partial \xi} = \iint (f' f'_1 - f f_1) d_D^2 |\mathbf{g}| \cos\theta d\Omega d\xi_1 \quad (1-6)$$

where, $|\xi'_2 - \xi'_1| = |\xi_2 - \xi_1| = |\mathbf{g}|$; dS is the sphere microelement, $dS = d_D^2 d\Omega$, with $d\Omega$ being the angle of the first particle. The right side of equation (1-6) is considered the collision term, usually represented as $J(ff_1)$.

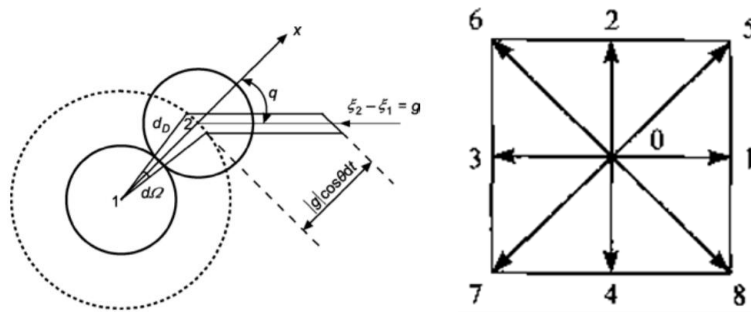


Figure 1-8. Schemes of the collision model and the D2Q9 velocity discretization model.
Reprint with permission from ref. [80]

The Maxwell distribution is a particular solution for the Boltzmann equation in the condition of monocomponent gas without external force. The collision term in the Boltzmann equation

is nonlinear, which makes it very complicated to obtain a detailed solution. The BGK approximation[81] uses a simplified operator Ω_f to replace the collision term $J(ff_1)$ in the Boltzmann equation:

$$\Omega_f = \nu[f^{eq}(r, \xi) - f(r, \xi, t)] \quad (1-7)$$

Where f^{eq} is the Maxwell equilibrium distribution; τ_0 is the average time interval between two collisions, i.e., relaxation time. Thus the Boltzmann-BGK equation can be re-written as:

$$\frac{\partial f}{\partial t} + \boldsymbol{\xi} \cdot \frac{\partial f}{\partial \mathbf{r}} + \mathbf{a} \cdot \frac{\partial f}{\partial \boldsymbol{\xi}} = \frac{1}{\tau_0} (f^{eq} - f) \quad (1-8)$$

$$f^{eq} - f = (f^{eq} - f)|_{t=0} \exp(-\frac{t}{\tau_0}) \quad (1-9)$$

The lattice Boltzmann (LB) equation is a special discrete form of the Boltzmann-BGK equation. The particle velocity ξ can be simplified as a velocity space of finite dimensions $\{\mathbf{e}_0, \mathbf{e}_1, \dots, \mathbf{e}_N\}$, with N representing the number of different types of velocities. Then the distribution function f can be discretized as $\{f_0, f_1, \dots, f_N\}$, $f_\alpha = f_\alpha(\mathbf{r}, \mathbf{e}_\alpha, t)$. So the lattice Boltzmann-BGK equation with the external force term can be expressed as:

$$f_\alpha(\mathbf{r} + \mathbf{e}_\alpha \delta_t, t + \delta_t) - f_\alpha(\mathbf{r}, t) = -\frac{1}{\tau} [f_\alpha(\mathbf{r}, t) - f_\alpha^{eq}(\mathbf{r}, t)] + \delta_t F_\alpha(\mathbf{r}, t) \quad (1-10)$$

Where, F_α is the external force term and can be denoted as $F_\alpha = (\mathbf{a} \cdot \nabla_\xi f)_\alpha$, while the dimensionless relaxation time is $\tau = \tau_0/\delta_t$, with δ_t being the time step.

Besides the above models, there are several other LB models divided by velocity discretization or boundary conditions. For example, Qian[82] proposed D2Q9, D2Q7, D3Q15 and D3Q19 models, etc. More specifically, for incompressible LB models[83], there are incompressible isothermal models and incompressible thermal models, while for compressible perfect gas LB models, there are multi-velocities models (Chen-Ohashi model[84], Watari-Tsutahara model[85]), tunable specific heat ratio models (multi-energy model[86], Kataoka-Tsutahara model[87], Qu-Shu model[88]) and coupled double distribution function models[89], etc. In terms of boundary conditions[90], the LBM can be further divided into the heuristic scheme, the kinetic scheme, the extrapolation scheme and the complex boundary scheme, etc. In the application of acoustic transmissions, the compressible model with different boundary conditions is mostly employed.

However, most of the LB models are applied in the continuum regime for fluid flow issues, while the DSMC method can be available in the transition regime (the hydrodynamic length is in the same magnitude of the related mean free path). To investigate wave propagation in small confined geometries with specific boundary conditions, Hadjiconstantinou[91] in 2003 developed a model with the first-order slip boundary condition and provided an analytical solution for acoustic wave propagation in micro- and nanochannels, which was an extension of Lamb's continuum treatment[92, 93]. In 2005, considering the effects of the Knudsen layer and using the second-order velocity boundary condition, Hadjiconstantinou[94] solved the oscillatory shear-driven Couette flow problem using the Navier-Stokes approximation and achieved good agreement with DSMC results up to $Kn \approx 0.4$. Kozlov et al.[95] investigated acoustical properties in pores of simple geometries with the first-order approximation and validated their results with experimental data of dynamic density at low frequencies. Umnova et al.[96] developed an analytical model to describe acoustic propagation in microfibrinous materials while accounting for the slip boundary effect, where the homogenous method used was also verified by finite element method (FEM) simulation. In terms of numerical investigation, various simulation methods have been proposed, such as the linearized Boltzmann method[97-99], Lattice Boltzmann method[100-102], Bhatnagar-Gross-Krook (BGK) model[103, 104], molecular dynamics (MD) model[105-107], and DSMC[80, 108]. Based on our literature survey, the DSMC method, initially proposed by G. A. Bird[80], is the most widely used tool for the simulation of acoustic wave propagation at the micro- and nanoscales and is renowned for its accuracy and time efficiency. Derivative DSMC methods, such as Wang and Xu's unified gas-kinetic scheme DSMC (UGKS-DSMC)[109], Fan and Shen's information preserving DSMC (IP-DSMC)[110], Mohssen and Hadjiconstantinou's Low-Variance Deviational Simulation Monte Carlo (LVDSMC)[111], were proposed to improve the performance of the traditional DSMC method. All these works mentioned above can only extend the traditional continuum theory up to $Kn \approx 0.4$ or even smaller for the acoustic wave propagation in micro- and nanochannels, so there is still a need to develop an analytical solution suitable for higher Knudsen numbers.

1.6 Challenges and objectives

Although versatile topological acoustic systems have been designed and investigated, there are many limitations blocking their applications in sound attenuation[112-114], information delivering[54, 55, 58], ultrasonic imaging[115-117], and acoustic cloaking[118-120], etc. The development of topological acoustics has reached a stage where many analogous methodologies of condensed matter systems have been investigated, including the QHE, the QSHE and the QVHE based methods. However, these systems are still considered to be at an early stage, as the more practical properties of miniaturization, broadband, wide tunability and noiseless dynamic controlling for topological acoustic systems or designs still require further investigation.

Specifically, two types of mechanisms are fully investigated to realize topological acoustics, including introducing external air flow and designing unique metamaterials with gapless edge spin states, both have their unique advantages and disadvantages. Generally, for the QHE based methods, bulky and noisy external equipment is needed to import air flow inside an acoustic circulator. For the QSHE and QVHE based methods, a specific lattice array is needed to realize good topological performance. Despite current research, and in order to obtain their practical properties, special modulation strategies and versatile mechanisms require further investigation. For instance, an acoustic transmission mechanism at a microscale or smaller scale is needed to realize miniaturized topological acoustic systems and ultrasonic imaging related applications. Modulation strategies other than introducing external air flow and rotating sonic crystal units are needed to obtain dynamically wide-band unidirectional transmission control.

Paving the way towards practical performance of topological acoustics is necessary in real applications. Therefore, the ultimate objective of this thesis is to develop more modulation strategies and more detailed mechanisms to advance the realization of miniaturization, broadband, wide tunability and noiseless dynamic controlling for topological acoustic systems. Specifically, miniaturizing the unit cell into the millimeter or even smaller scale requires better modulation strategies and fuller investigation of acoustic transmission mechanisms at the micro- and nanoscale, which is significant to realizing ultrasonic related applications. Wide tunability plays a key role in wide-band control of one-way transmission

routes and edge transmission properties, and promotes the applications of acoustic cloaking, ultrasonic imaging, information delivering and noise attenuation, etc. In addition, noiseless dynamic controlling makes the topological acoustic system more accurate and reliable.

1.7 Outline of the thesis

In what follows, the dissertation will be organized in an outline as six chapters.

Chapter 1 reviews the research background information relevant to the thesis work, including the designs, modulation strategies and functionalities for acoustic analogues of the QHE, the QSHE, and the QVHE, respectively. Different topological acoustic properties can be achieved based on analogues of the condensed matter system, such as edge transmissions, specific route transmissions, and nonreciprocal control. Then, the acoustic transmission mechanism at the micro- and nanoscale is provided for further investigation. Finally, research challenges and objectives are identified.

Recent developments in valleytronic materials have inspired developing various analogues of sonic crystal systems for manipulating airborne acoustic transmissions. Earlier designs of acoustic topological insulators were normally characterized by untunable bulky geometries and a narrow effective frequency response, which limited the design and development of practical acoustic devices. To avoid the aforementioned limitations, Chapter 2 introduces a gapless topologically protected acoustic resonator system based on the QVHE in reconfigurable phononic crystals. The method of simply rotating the modified spiral springs to adjust the inner radius without altering the lattice structure can be utilized to realize backscattering immune, tunable, broadband and miniaturized functional acoustic applications. It offers a design route in novel valley phenomena for acoustic topological flow-free resonator systems.

The QVHE based topological acoustic design in Chapter 2 still need bulky mechanical control devices and the whole setup is not noiseless. The further investigation of nonreciprocal acoustics and topological acoustics can be inspired by the recent development of the QHE that breaks time-reversal symmetry by magnetic biasing. Nonreciprocal acoustic propagation is highly desirable to control acoustics in isolation, broadband unidirectional

transmission, and topologically robust to structural disorders or defects. So far, these fascinating properties have been investigated through fan-induced moving media, acoustic capacitance adjustment and acoustic metamaterials. However, these may be associated with disadvantages including extra noise and limited dynamic controlling performance. To solve these problems, Chapter 3 introduces heat-induced natural convection coupled with an acoustic circulator to demonstrate that a classical acoustic circulator with thermal management can realize robust nonreciprocal acoustic propagation, which is based on the QHE. The concept of combining heat-induced natural convection and aeroacoustics creates a new practical paradigm and increases the feasibility for nonreciprocal acoustics due to the merits of dynamic control, versatile topological structures, and miniaturization in the absence of moving parts.

Some fascinating topological acoustic properties have been investigated through fan-induced moving media (or the natural convection induced air flow provided by me in Chapter 3), acoustic capacitance adjustment and acoustic metamaterials (Chapter 2). However, most of them are still associated with disadvantages including extra noise, bulky volume and limited dynamic controlling performance. Thus, Chapter 4 introduces a temperature modulation scheme in a lattice of resonators to demonstrate that the Floquet topological insulators with thermal control can realize topologically robust and nonreciprocal acoustic propagation. This control strategy provides an alternative platform to conduct acoustic topological applications, especially for noiseless and miniaturized airborne acoustics. Thermal modulation provides the possibility of miniaturizing topological airborne acoustics into the millimeter scale or even smaller.

Furthermore, in order to investigate the topological acoustics in ultrasonic or in a micro- or nanostructure to realize miniaturization, an analytical model that can effectively clarify the acoustic transmission mechanism in micro- and nanochannels is necessary. Moreover, the acoustic wave propagating through porous nanomaterials like aerogels, MEMS devices, high-frequency acoustic transmission devices or near-vacuum systems, possesses relatively high Knudsen numbers, normally in the transition regime ($0.1 < Kn < 10$), in which the classical continuum theory breaks down. So in Chapter 5, a theoretical model with the second-order slip boundary to describe acoustic wave propagation in micro- and nanochannels, is proposed.

The proposed theoretical model provides analytical solutions for the complex wavenumber, attenuation coefficient and other related transmission variables as functions of a Knudsen number in the early transition regime ($0.1 < \text{Kn} < 1.0$), which are valuable for understanding acoustics at the micro- and nanoscales. In addition, numerical simulations using the molecular-based DSMC method for dilute argon gas are carried out to validate the model and its analytical results. This model can effectively predict the acoustic behaviour in micro- and nanochannels, which is important for future research into topological acoustics in ultrasonic or in a small structure to realize miniaturization.

Finally, Chapter 6 provides conclusions and a summary of all the results reported within the thesis, along with prospects for future work.

Chapter 2

2 Tunable acoustic valley edge states in a flow-free resonator system

Recent developments in valleytronic materials have inspired developing various analogues of sonic crystal systems for manipulating airborne acoustic transmissions. Earlier designs of acoustic topological insulators were normally characterized by untunable bulky geometries and a narrow effective frequency response, which limited the design and development of practical acoustic devices. Here we design a gapless topologically protected acoustic resonator system based on valley edge states in reconfigurable phononic crystals. By simply rotating the modified spiral springs to adjust the inner radius without altering the outer lattice structure, this method can be utilized to realize backscattering immune, tunable, broadband and miniaturized functional acoustic applications. This study also offers a design route in novel valley phenomena for acoustic topological flow-free resonator systems. It is noted here, this Chapter is based on author's publication: Liu, X., Q. Guo, and J. Yang, *Tunable acoustic valley edge states in a flow-free resonator system. Applied Physics Letters*, 2019. **115**(7): p. 074102. And all the figures are used with the permission from ref. [121].

2.1 Introduction

The discoveries of TIs[16, 122, 123], the QHE[124, 125], and QSHE[14, 17] in condensed matter physics have inspired the exploration of nonreciprocal or topological performances of classical waves, such as acoustics[43, 46, 126-129], light[130-132], and mechanical waves.[133-135] Early attempts at constructing nonreciprocal[31, 129] and topological acoustic states[33, 34, 127, 136, 137] relied on importing external circulating fluid as the background flow, which can work as the analogue of the electromagnetic field in the QHE. Artificial structures of phononic graphene in the doubly degenerate Dirac-like cones[5, 45, 46, 138] can be used to map the QSHE. C_{3v} phononic crystals or acoustic metamaterials[45, 134, 139, 140] consisting of anisotropic rods with versatile modulations[72] and inherent spin-orbital coupling bands constitute the QVHE.[65-67] All these concepts are investigated to design different types of acoustic topological insulators to control acoustic transmissions,

resulting in acoustic isolation, one-way transmission along edges, and topological immunity against structural disorder or defects.

Recently, the QVHE labeled with the band structure of the two energy extrema in the momentum space has shown great potential in delivering and storing information. The discrete degree of freedom displays a selective valley with topologically non-trivial properties, among which the Chern number remains zero and the time-reversal symmetry is intact. The easily achieved valleytronic properties[55, 141] of manipulation and transmission have been extended to the topological acoustics for novel control of airborne acoustics. In acoustic related research of the valley edge states, the topological acoustic performances are achieved by the anisotropic lattice of scatters with versatile geometries and rotating units.[35, 45, 70, 142] However, great challenges still remain given the lack of tunable, broadband and miniaturized functional acoustic related applications.

Here, we present a design to realize tunable and broadband acoustic topological edge states in a flow-free resonator system with a millimeter order of magnitude for each small unit. This two-dimensional periodic acoustic counterpart of a gapped graphene monolayer can be considered a tight-binding model. By designing tunable inner radii of adjacent hollow circulators to realize versatile combinations of chiral on-site rotating modulation schemes, the existence of topological transition is demonstrated, which is characterized by the opposite valley Chern numbers. Different from breaking translational symmetries and point groups in pseudomagnetic fields, we mimic the QVHE-based valley states as opposed to spin states. Specifically, the mirror-symmetry-breaking property is accomplished by dynamically adjusting the inner radii of the six hollow circulators in each primitive cell. This induces inversed band modulation in different valley pseudospin degrees of freedom. Moreover, the tunable inner radius in each circulator can allow us to adjust this type of acoustic topological property with wide effective frequency ranges and configurable transmitting routes. Full-wave simulations of band structure analysis and acoustic propagation are conducted and used to display these fascinating physics of topological acoustics with versatile potential applications, including acoustic cloaking[118-120, 143], ultrasonic imaging[115-117, 144-146], RF filters[147-149], and noise attenuation[112-114, 150-154], etc.

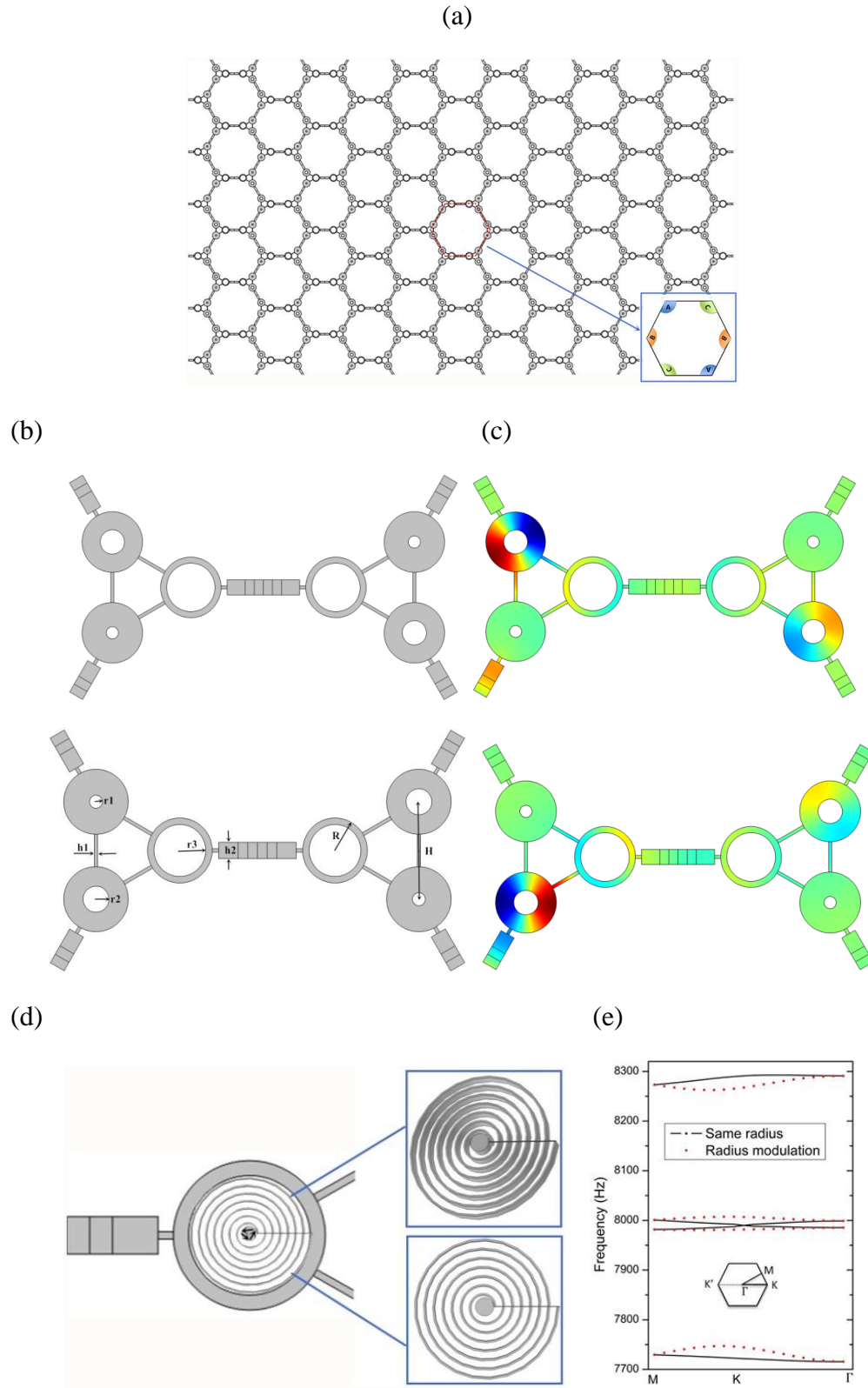


Figure 2-1. (a) The hexagonal lattice formed by acoustic double-trimer cell. Each trimer consists of three connected hollow circulators and rectangular channels, with air filled

inside all the grey regions (inset: region A, B, C denotes different radius combination units). (b) Two types of double-trimer centrosymmetric cells with self-inward (upper structure) or self-outward (lower structure) radii-rotating modulation. (c) Two types of doubly degenerate dipolar resonances at 7970-8010 Hz corresponding to the configurations of upper and lower structures in (b). The colors from red to blue represent the values of pressure from positive maximum to negative maximum. (d) The tunable inner radius using modified spiral springs with lead rail. (e) Comparison between the band structure without (black curves, same radius in the trimer structure) and with (red dots) radius modulation.

2.2 Topological acoustic model and mode analysis

As shown in Figure 2-1(a), the acoustic system designed in this work can be considered a complex honeycomb acoustic lattice described by a simplified nearest-neighbor tight-binding model.[155] The primitive double-trimer cell with mirror-symmetry-breaking self-inward or self-outward units is shown in Figure 2-1(b). All the grey regions are treated as air and the white regions are considered solid walls in the simulation. Each trimer consists of three acoustic hollow resonators connected by thin rectangular waveguides ($h_1 = \frac{1}{30}a, h_2 = \frac{1}{6}a$). The nearest-neighbor distance of two resonators is $H = a = 30 \text{ mm}$, and the lattice constant is $a_0 = \left(\frac{10\sqrt{3}}{3} - 1\right)a$. Each primitive cell has two acoustic three-unit resonators (each resonator has the same outer radius of $R = 10 \text{ mm}$, but with tunable inner radius, while for the designs of Figure 2-1, 2-3, 2-4, r_1, r_2 and r_3 are set as $\frac{1}{15}a, \frac{2}{15}a$ and $\frac{4}{15}a$, respectively). The tunable-radius mechanism is realized by replacing the solid inner cylindrical column with modified spiral springs as shown in Figure 2-1(d). The solid column in the middle of this spiral spring is connected with the outer spring edge by the lead rail, while the end interface of the outer spring edge is pinned in the lead rail, which makes this spiral spring well convoluted while rotating the solid column in the radius-changing process. All the inner radii of the resonators can be adjusted to realize different acoustic properties.

Different inner radii of the trimer structure are modulated by rotating the modified spiral springs, which can obtain wide-band nonreciprocal acoustic transmission and can be used to

guide the design of topological acoustic systems. The ratio of acoustic energy intensity between the acoustic output 3 and output 2 is shown in Figure 2-2. Specifically, different combinations of circulators in the trimer unit display different optimal nonreciprocal frequency ranges. The corresponding effective bandwidth is around 50 Hz for every type of trimer structure without changing the outer radius. More radius combinations can be found in the supplementary material and the working frequency can be in a wide range of 6.1-8 kHz in the dipolar mode. Although the radius difference is small, there are good nonreciprocal transmission properties and the dimensions considered in this design can be narrowed into the millimeter scale, which really inspires future investigations of tunable broadband and miniaturized acoustic topological performance. For even smaller structures, the tuning mechanisms can be thermal management with thermal expansion material, camera aperture rotating mechanical structure, or the smaller proposed modified spiral spring structure.

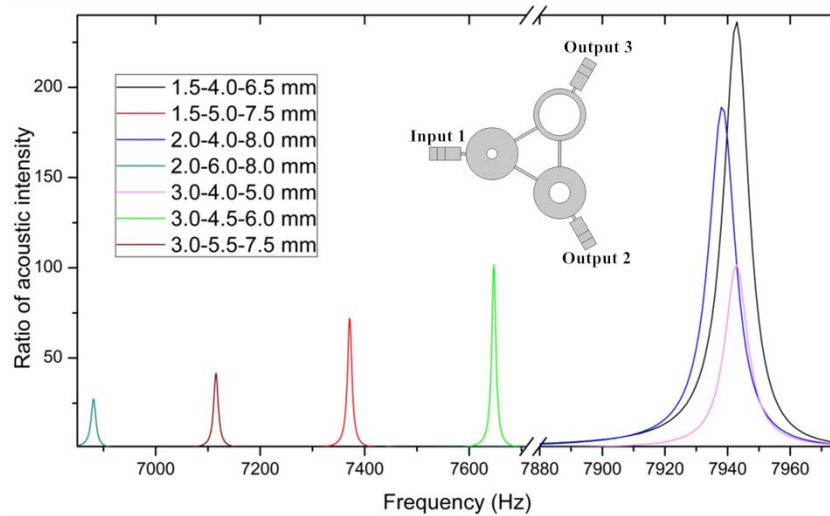


Figure 2-2. The ratio of acoustic intensity (Output 3/Output 2) at different radius modulations in a single trimer (middle inset: trimer structure). The dimensions display the inner radius of every circulator in the trimer structure. The inner radius changes from 1.5 mm to a maximum of 8.0 mm.

2.3 Analytical acoustic band structures

The geometry under analysis is mapped onto a tight-binding Hamiltonian model considering the hexagonal lattice with the nearest-hopping, which is modified to adjust the internal trimer

structure (shown in the middle inset of Figure 2-2). The Bloch Hamiltonian[67] \bar{H} of this hexagonal periodic system can be written as

$$\bar{H} = \begin{pmatrix} V_0 + V_A & H_{\mathbf{k}} & H_{\mathbf{k}}^* \\ H_{\mathbf{k}}^* & V_0 + V_B & H_{\mathbf{k}} \\ H_{\mathbf{k}} & H_{\mathbf{k}}^* & V_0 + V_C \end{pmatrix} \quad (2-1)$$

$$H_{\mathbf{k}} = -\varepsilon_V [\exp(-i\mathbf{k} \cdot \mathbf{e}_1) + \exp(-i\mathbf{k} \cdot \mathbf{e}_2) + \exp(-i\mathbf{k} \cdot \mathbf{e}_3)] \quad (2-2)$$

The parameters introduced in Eq. (2-1) and Eq. (2-2) are defined in the form of the Hamiltonian, where V_0 is the on-site energy, which is in the condition of the lowest resonant frequency for the average of all isolated acoustic resonators. V_A , V_B and V_C represent the energy modulations for the corresponding resonators due to the changes in volume, while $H_{\mathbf{k}}$ is the on-site coupling energy between the resonators. Moreover, ε_V is denoted as the hopping terms. $\mathbf{e}_1 = (0, \mathbf{a})$, $\mathbf{e}_2 = \left(-\frac{\sqrt{3}}{2}\mathbf{a}, -\frac{a}{2}\right)$, and $\mathbf{e}_3 = \left(\frac{\sqrt{3}}{2}\mathbf{a}, -\frac{a}{2}\right)$ are used to define the position of the nearest-neighbor connected resonators, and $\mathbf{k} = (k_x, k_y, k_z)$ is the Bloch wave vector. When $V_A = V_B = V_C$, this means all three resonators in the acoustic trimer are the same, and the system in this condition exhibits space-inversion symmetry.

The band structure of the double-trimer cell is achieved by the full-wave simulation using COMSOL Multiphysics, and it exhibits one Dirac cone at the K point when $V_A = V_B = V_C$, as shown in the black line of Figure 2-1(e). If $V_A \neq V_B \neq V_C$, as shown in the red dots of Figure 2-1(e), such a cell includes this specific orientation in which the band gap opens at the K point from 7970-8010 Hz. The doubly degenerate dipolar resonance associated with the exchange of kinetic and potential energy between the interconnected waveguides and the hollow circulators is shown in Figure 2-1(c). The self-inward or self-outward radii-rotating modulation directs the acoustic pressure distribution in two opposite paths. The topological transition exists when the exchange between the two opposite modes in the same valley emerges.

In order to further understand this topological transition, we expand the above Hamiltonian in Eq. (2-1) with the consideration of a nonzero valley Chern number. Also, the $\mathbf{k} \cdot \mathbf{p}$ perturbation method[67] is applied as a form of effective Hamiltonian,

$$H_{\mathbf{K}}(\delta\mathbf{k}) = v_D \delta k_x \sigma_x + v_D \delta k_y \sigma_y + m v_D^2 \sigma_z \quad (2-3)$$

where v_D and σ_i are the Pauli matrices for the degrees of freedom of the valley and the cell, respectively. By separating the Dirac phase with $m = 0$, the mass term of $m = \Delta w / 2v_D^2$ is utilized to characterize the different valley Hall insulators, as Δw denotes the bandwidth for the opening band gap. The same radii-rotating orientation in the double-trimer cell combines with $V_A \neq V_B \neq V_C$, which determines the band states of this acoustic structure. The local Berry curvature[58] around the valley can be calculated utilizing the eigenvector,

$$\Omega_{\mathbf{K}}(\delta\mathbf{k}) = \frac{m v_D}{2(\delta k^2 + m^3 v_D^2)^{3/2}} \quad (2-4)$$

Therefore, the topological charges (denoted as the valley Chern number) of the first band can be calculated by integrating the local Berry curvature in half of the Brillouin zone [56, 57], as the upper band or the lower band in the valley K (K') displays different signs of for the difference of the valley-projected Chern numbers,

$$2\pi C_K = \int \Omega_{\mathbf{K}}(\delta\mathbf{k}) dS = \pi \text{sgn}(m) \quad (2-5)$$

$$2\pi C_{K'} = \int \Omega_{\mathbf{K}'}(\delta\mathbf{k}) dS = -\pi \text{sgn}(m) \quad (2-6)$$

The Chern numbers of the inward (outward) rotating modulation in the upper (lower) cell structure of Figure 2-1(b) are $\pm \frac{1}{2} (\mp \frac{1}{2})$ for the upper or lower band at related valley domains. If a proper domain wall is built with the appropriate modulation of each cell array (domain A, B and C in Figure 2-1(a)), the difference in the two opposite bands for the Chern numbers is equal to ± 1 , which indicates the existence of a topological valley edge state at the interface of the two opposite modulation domains with the correspondence of the bulk edge. Obviously, the topological phase transition state occurs when $V_A = V_B = V_C$. Furthermore, there are three resonator units in every domain, which means the phase modulation in this type of structure can include a large amount of combinations.

To verify the existence of such valley-dependent edge states at the designed resonator system with topological performance, we utilize a supercell composes of a 1-by-12 array of primitive cells with inward and outward rotating modulations in the upper and lower domain,

respectively (Figure 2-3(b)). Simulation results, along with the consideration of periodic boundary conditions in Figure 2-3(a), exhibit the bulk and edge bands of the corresponding projected band structures. The group velocity of the edge state at the valley point is positive (negative) because the change of valley Chern number between the two types of domains is equal to $1(-1)$, indicating the positive (negative) transmission direction in the edge states. Also, the pressure distribution of this edge mode is shown in Figure 2-3(b), which displays the local valley pseudospin state locked to the transmission direction.

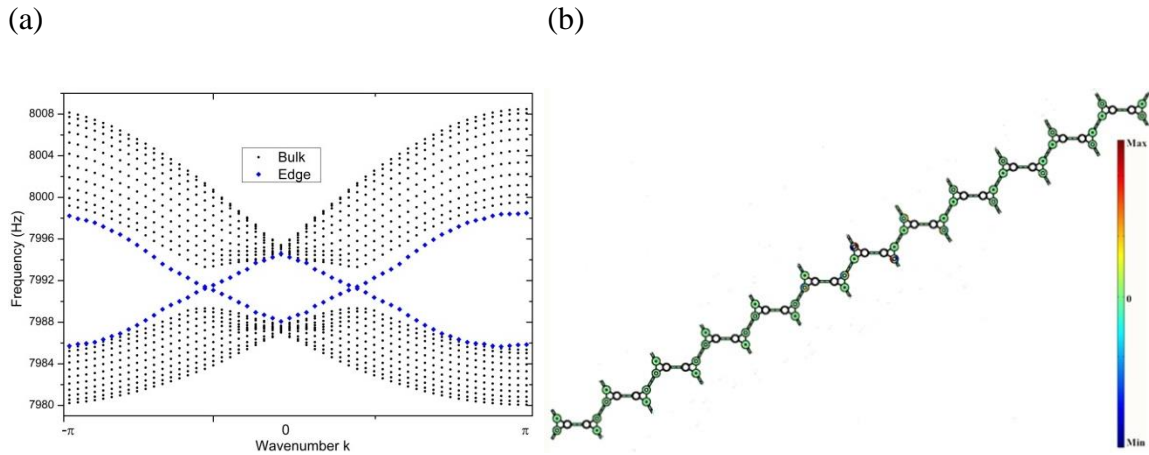


Figure 2-3. (a) Acoustic band-structure diagram for a supercell composed of a 1-by-12 periodic array of double-trimer cells. Black dots refer to bulk modes, and blue dots refer to edge modes. (b) Acoustic pressure distribution for the dominant harmonic cells of an edge mode localized at the supercell centre.

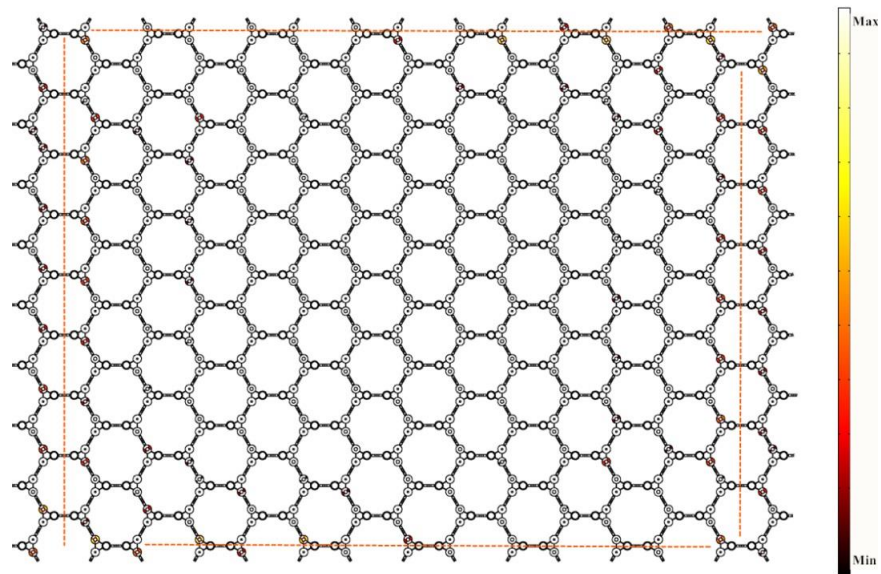
2.4 Topological acoustic performance

This tunable acoustic valley edge state based topological insulator allows the existence of excellent topological protections against local disorders and defects. To confirm the topological performance of these acoustic valley edge states, large-scale numerical experiments with a large amount of the lattice array are conducted. Figure 2-4(a) displays that an acoustic edge state can seamlessly transmit along a periodic lattice array despite the presence of a stringent structure of turns and transitions. Moreover, the absence of backward-transmission modes ensures the lack of back reflection initiated by arbitrary abruptness or discontinuity. Figure 2-4(b) illustrates two types of domains with inward-radii modulation

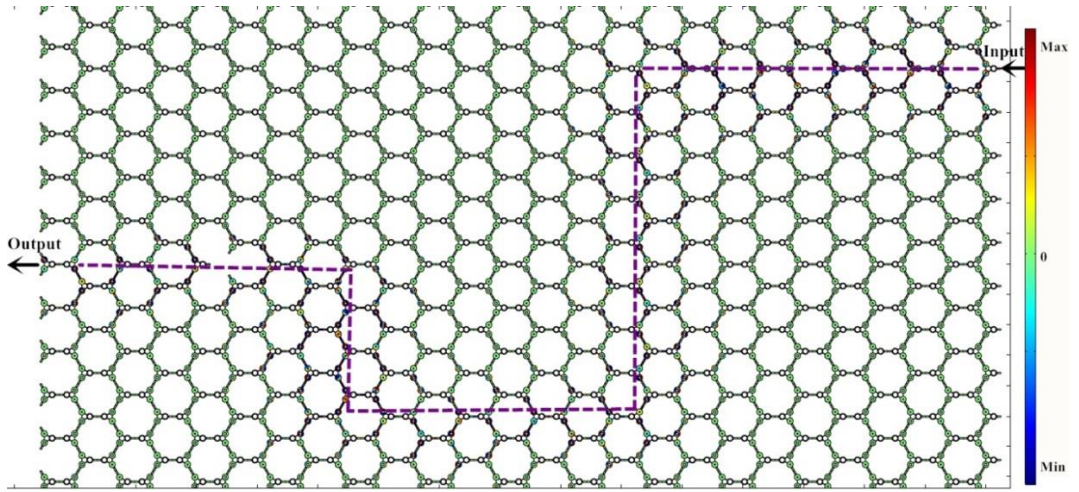
spins and outward-radii modulation spins placed in the upper domain and lower domain, respectively. Even with one missing trimer defect and sharp turns, we can still realize backscattering immune, broadband nonreciprocal, and dynamically tunable acoustic waveguides. Moreover, the transmission route can be reconfigured by changing the separating boundaries and the related radius modulation strategy, which provides great potential in acoustic manipulating devices. For the opposite domain configuration, as shown in Figure 2-4(c), the gapless topological edge state is not supported so that the transmission along the domain separating edge will vanish.

In this work, we have designed a flow-free acoustic resonator system that can work as the acoustic analogue of the QVHE-based topological insulator. Through the radius modulations in a two-dimensional trimer structure, the formed honeycomb lattice with topological valley edge states can easily realize backscattering immune, broadband nonreciprocal, and dynamically tunable acoustic waveguides. In particular, the ability to independently adjust the inner radius of the circulator for the trimer-based lattice structure enables flexible topological configurations in a wide frequency range, which can further extend the design versatilities of future tunable acoustic topological devices.

(a)



(b)



(c)

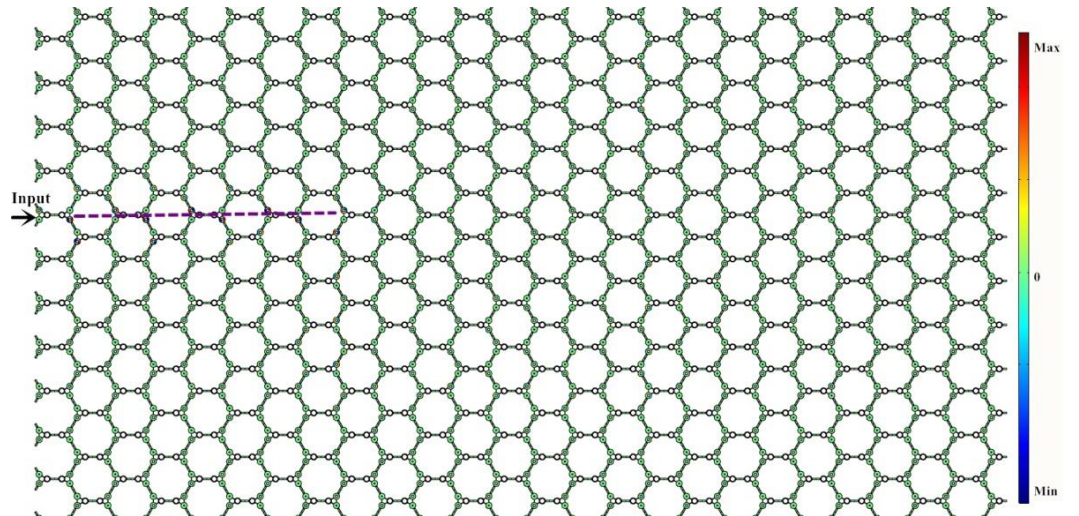


Figure 2-4. (a) Immunity of the nonreciprocal edge mode to versatile edge geometries and sharp turns. (b) Reconfigurable and topologically protected one-way edge waveguide along the separating boundary and the robustness against defects. The self-inward radii-rotating modulation cell array is placed in the upper domain, while the self-outward modulation is placed in the lower domain. (c) Topological edge states with the opposite direction for the input source as of (b). The color legend displays the acoustic pressure.

2.5 Supplementary material

2.5.1. Broadband acoustic transmission in radii-tunable resonator systems

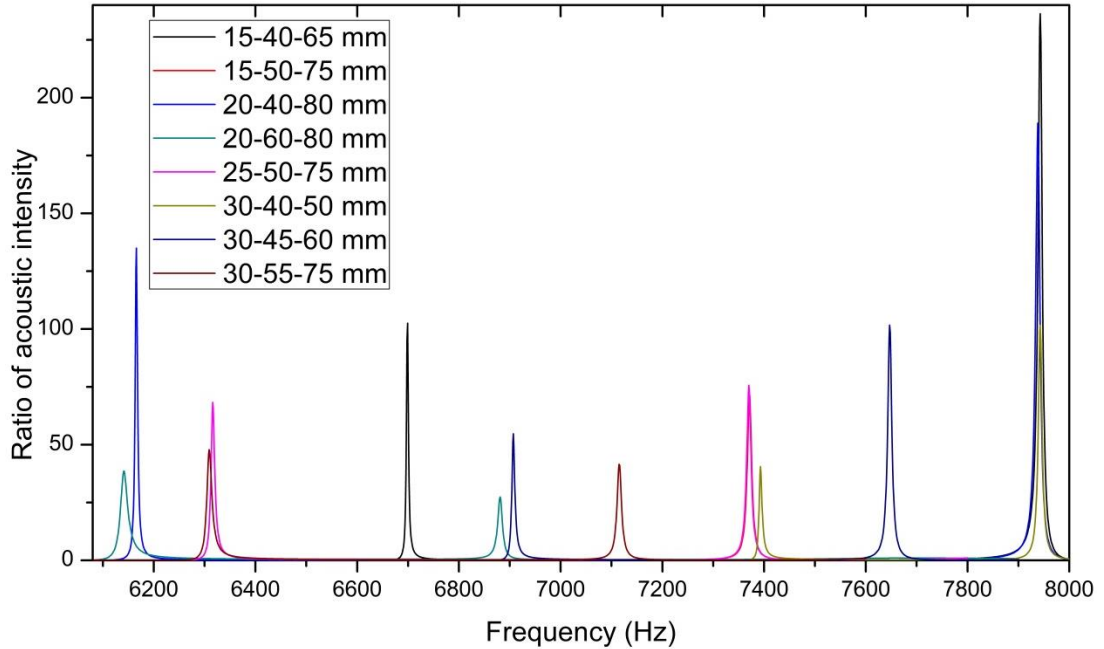


Figure S2-1. The ratio of acoustic intensity (Output 3/Output 2) at different radius modulations in a single trimer with a wider resonant frequency range. The inner radius changes from 1.5 mm to a maximum of 8.0 mm.

2.5.2. Simulation process

Acoustic pressure distribution, band structures and mode patterns presented in this work are computed using the finite element solver *COMSOL Multiphysics*. Pressure acoustics, eigenfrequency model is adopted and the media filled in the resonators is set as air. In Figure 2-3(a), the band diagram is computed with a 1×12 supercell which is periodic along x direction. To compute the full-wave numerical simulation in Figure 2-4(a), a 14×9 periodical lattice array is adopted. All the field patterns shown in the manuscript are computed with pressure acoustics, frequency domain model in the finite element solver *COMSOL Multiphysics*.

2.5.3. Hamiltonian derivation process

The Bloch Hamiltonian \bar{H} of this hexagonal periodic system can be written as,

$$\bar{H} = \begin{pmatrix} V_0 + V_A & H_{\mathbf{k}} & H_{\mathbf{k}}^* \\ H_{\mathbf{k}}^* & V_0 + V_B & H_{\mathbf{k}} \\ H_{\mathbf{k}} & H_{\mathbf{k}}^* & V_0 + V_C \end{pmatrix} \quad (\text{S2-1})$$

$$H_{\mathbf{k}} = -\varepsilon_V [\exp(-i\mathbf{k} \cdot \mathbf{e}_1) + \exp(-i\mathbf{k} \cdot \mathbf{e}_2) + \exp(-i\mathbf{k} \cdot \mathbf{e}_3)] \quad (\text{S2-2})$$

According to the $\mathbf{k} \cdot \mathbf{p}$ perturbation method, the perturbation term of the Hamiltonian is defined as,

$$H'_k = \frac{\hbar^2 k^2}{2m} + \frac{\hbar \mathbf{k} \cdot \mathbf{p}}{m} \quad (\text{S2-3})$$

$$\mathbf{k} \cdot \mathbf{p} = k_x \left(-i\hbar \frac{\partial}{\partial x} \right) + k_y \left(-i\hbar \frac{\partial}{\partial y} \right) + k_z \left(-i\hbar \frac{\partial}{\partial z} \right) \quad (\text{S2-4})$$

And also, the Hamiltonian is,

$$H_k = H'_k + H_0 \quad (\text{S2-5})$$

$$H_0 = \frac{p^2}{2m} + V \quad (\text{S2-6})$$

Then considering the acoustic wave equation,

$$\nabla^2 p + k^2 p = 0 \quad (\text{S2-7})$$

The following Eq. (S2-8) is the $\mathbf{k} \cdot \mathbf{p}$ perturbation term for the acoustic wave equation, which can be obtained by expanding the Bloch eigenstates at point \mathbf{k} as the linear combinations of the Bloch eigenstates at point Γ , then we can derive,

$$H'_k = \frac{2i}{\rho} \mathbf{k} \cdot \nabla + i\mathbf{k} \cdot \nabla \frac{1}{\rho} - \frac{k^2}{\rho} \quad (\text{S2-8})$$

For the trimer unit with $V_A = V_B = V_C$, the perturbation Hamiltonian $\delta \mathbf{k} \cdot \mathbf{p}$, spanned by the degenerated states $\psi_{p^-}{}^0$ and $\psi_{q^+}{}^0$, yields conic dispersions centered at the hexagonal

Brillouin zone corners due to the protection of the C_{3v} symmetry. Here, \mathbf{p} is a vectorial operator determined by the density distribution of the lattice unit. The mirror symmetry is broken as the change of modulation handedness, and the deterministic degeneracy is thus removed. This leads to a Dirac mass term $\delta_{ij}(\omega_i^2 - \omega_D^2)$, where $\omega_i = \omega_p^-$ or ω_q^+ is the volume difference dependent band-edge frequency, and ω_D is the Dirac frequency of the trimer unit with $V_A = V_B = V_C$. Utilizing the detailed form of the \mathbf{p} matrix, $\mathbf{p}_{11} = \mathbf{p}_{22} = 0$ and $\mathbf{p}_{21} = \mathbf{p}_{12} = 2w_D v_D (\hat{\mathbf{x}} + i\hat{\mathbf{y}})$, we can derive a compact form of the perturbation Hamiltonian H'_k that satisfies the eigen-problem $H'_k \psi = \delta\omega \psi$, where $\delta\omega$ is the frequency deviation from ω_D .

We can further expand the above Hamiltonian in Eq. (S2-1) near the K point, from the $\mathbf{k} \cdot \mathbf{p}$ perturbation method and spanned by the degenerate vortex pseudospins $\psi_{p^-}^0$ and $\psi_{q^+}^0$, which can be expressed as,

$$H_K(\delta\mathbf{k}) = v_D \delta k_x \sigma_x + v_D \delta k_y \sigma_y + m v_D^2 \sigma_z \quad (\text{S2-9})$$

Chapter 3

3 Robust nonreciprocal acoustic propagation in a compact acoustic circulator empowered by natural convection

The aforementioned QVHE based topological acoustic design still need bulky mechanical control devices and the whole setup is not noiseless. The further investigation of nonreciprocal acoustics and topological acoustics can be inspired by the recent development of the quantum Hall effect in condensed matter physics that breaks time-reversal symmetry by magnetic biasing. Nonreciprocal acoustic propagation is highly desirable to control acoustics in isolation, broadband unidirectional transmission, and topologically robust to structural disorders or defects. So far, these fascinating properties have been investigated through fan-induced moving media, acoustic capacitance adjustment and acoustic metamaterials. However, these may be associated with disadvantages including extra noise and limited dynamic controlling performance. Here we overcome these limitations by introducing heat-induced natural convection into acoustic circulator, and demonstrate that the classical acoustic circulator with thermal management can realize robust nonreciprocal acoustic propagation. The concept of combining heat-induced natural convection and aeroacoustics creates a new practical paradigm and increases the feasibility for nonreciprocal acoustics due to merits of dynamic control, versatile topological structures, and miniaturization in the absence of moving parts. It is noted here, this Chapter is based on author's publication: Liu X, Cai X, Guo Q, et al. Robust nonreciprocal acoustic propagation in a compact acoustic circulator empowered by natural convection[J]. *New Journal of Physics*, 2019, 21(5): 053001. And all the figures are used with the permission from ref. [129].

3.1 Introduction

The exploration at the basis of the QHE[15, 122, 156], has inspired many researchers in related fields of interest to investigate nonreciprocity and topologically nontrivial states[16, 123, 128, 157-159]. Reciprocity[132, 160] is a basic property in wave transmission process associated to the physical laws of time-reversal symmetry, which in return, makes the non-trivial band gaps attribute to the broken time-reversal symmetry[34, 47]. For the

electromagnetic nonreciprocity[161-163], the magnetic biasing is commonly employed to break reciprocity and achieve unidirectional mode with the local perturbation to the edge. Examples can be found in some photonic analogues, such as bianisotropic metamaterials[164], chiral waveguides[165, 166], silicon-ring resonators[167, 168] and photonic crystals[43, 127, 169, 170].

However, for the nonreciprocal acoustics, the magnetic biasing is typically associated with a weak magneto-acoustic effect[171], which is only observable under large and impractical biasing structures. Inspired by using the external magnetic biasing to create the electromagnetic nonreciprocity due to the Zeeman effect[172], some analogous approaches are introduced by importing rotational motion[31, 33, 136, 140] or angular momentum in specific acoustic resonators[32, 34]. *Alu et al*[31, 34] designed a circular resonator with flowing air rotating inside, together with three uniformly distributed ports for acoustic wave input/output. The flowing air works as the magnetic biasing counterpart and exhibits nonreciprocal acoustic propagation by breaking the time-reversal symmetry. *Alu et al.* also proposed[47] the idea of acoustic Floquet topological insulators combining with the concept of capacitance adjustment in the trimer metamolecules, which realized broadband acoustic isolation and nonreciprocal acoustic emitters. *Ni et al.*[32] investigated similar two-dimensional topologically one-way edge mode in networks of acoustic resonators with circulating air flow, which shows robust one-way edge transmission against structural disorders and defects. Moreover, in order to achieve unidirectional acoustic transmission, acoustic metamaterials, sonic crystal structures[67, 136] and phononic crystals[173, 174] combining circulating flow, have been proposed to realize one-way propagation of pseudo-spin-dependent edge states under broken time-reversal symmetry or controlled propagation of acoustic wave in an arbitrary network pathway.

The previous studies have developed various acoustic devices or system-level configurations to demonstrate the concept of nonreciprocal acoustics by breaking time-reversal symmetry or parity symmetry. More work is demanded to advance this technology into more practical functions. Using fans or other rotating machines as the formation of circulating flow did create a valid gauge flow field to break the time-reversal symmetry, whereas introducing inevitable extra noise and difficulty in miniaturizing the whole structure due to the bulky

angular momentum generator. For the case of acoustic capacitance adjustment[47], elastic material and piezoelectric actuators were employed, making it difficult to fabricate and realize dynamic control. For the acoustic metamaterial and sonic crystals, specific arrays or configurations often required relatively bulky structures that greatly limit their applications in a broad frequency range or concise dynamic control.

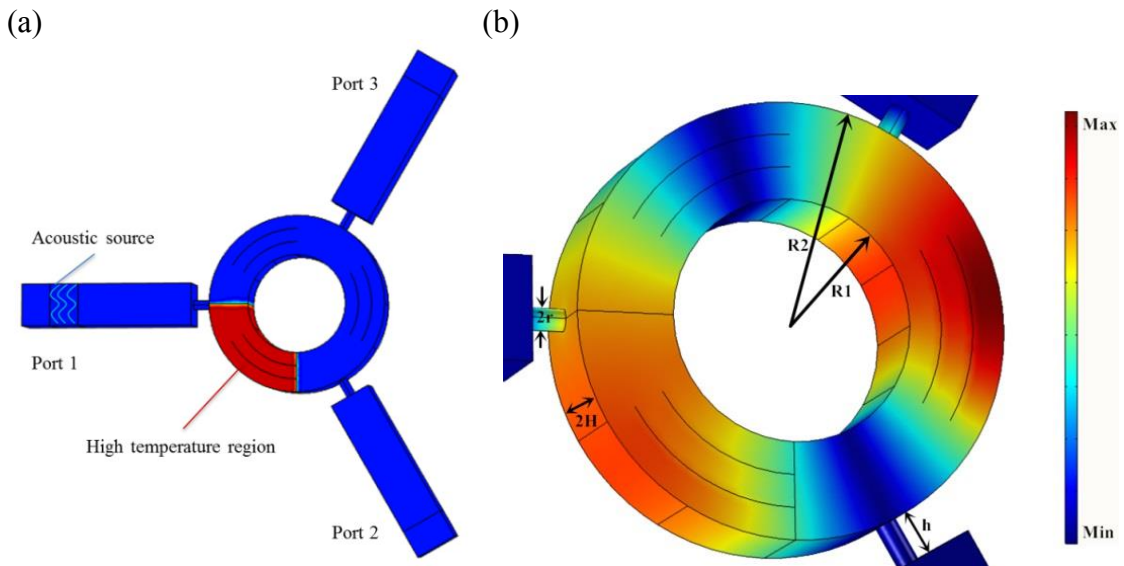
In this study, we propose a design of using heat-induced natural convection to form a steady air-flow circulation, which can break time-reversal symmetry and achieve robust nonreciprocal acoustic propagation in a ring resonator. In our geometry of analogue, a circulator with 120-degree rotational symmetry of three-port coaxial cylinders associated with three corresponding rectangular waveguides is designed. Distribution of a temperature gradient in a vertically placed ring circulator creates a steady circulating air-flow field due to the existence of buoyancy force. Meanwhile, velocity and flow direction in the circulator can be easily tuned by adjusting temperature distribution. In this scenario, no extra noise would be generated as no moving components are employed in the whole setup, which can facilitate its applications by conducting more accurate control and miniaturizing the whole structure. Our design, a compact configuration without moving parts, creates a new paradigm for the application of nonreciprocal acoustics, which reduces the difficulty in device/material fabrication. Moreover, we further demonstrate that the nonreciprocal resonators with different interior circulator configurations, can exhibit excellent nonreciprocal acoustic propagation performance empowered by the heat-induced natural convection. This study also shows great potential for the insulation of any interior structures in acoustic circulators.

3.2 Prototype design and mode analysis

In the designed 3D nonreciprocal acoustic circulator, three-port subwavelength rectangular waveguides ($44 \times 178 \times 44$ mm) are connected by hard-walled coaxial cylinders ($r = 4.75$ mm, $h = 21$ mm), and the height of the whole structure is 44 mm. Three groups of thin heating layers are evenly distributed (spaced with 120° within the hollow ring circulator) to form a tri-symmetric structure and relatively uniform velocity distribution. Moreover, dynamic control of the velocity field can be realized by heating different groups of these thin heating layers. The inner and outer radii of the ring circulator are set as $R_1 =$

51 mm and $R_2 = 92$ mm, respectively. The fundamental waveguide mode for acoustic plane wave is supported in the studied frequency range. In Figure 3-1(a), it can be found that the temperature distribution in the vertically placed circulator (buoyancy created by the lower left high temperature region) induces a steady circular velocity field by natural convection. Specifically, all the surfaces and two thin heating layers inside the hollow circulator of the red region are set as the high temperature region. Introducing this circular momentum to fill a subwavelength acoustic resonant ring circulator, the degenerate counter-propagating azimuthal resonant mode can be split. As is shown in Figure 3-1(b), the pressure distribution in a peak frequency is displayed with all the dimensions labeled, which can visualize the nonreciprocal protection. A proper velocity distribution induced by natural convection and a suitable circulator design together can create giant nonreciprocity through modal interference.

As is shown in Figure 3-1(c) and Figure 3-1(d), the acoustic circulator with biasing angular momentum field can support clockwise and counterclockwise dipole modes[32] with eigenfrequencies ω_{\pm} . If the fluid inside the circulator is stationary, these modes would be degenerate with $\omega_+ = \omega_-$. When the biasing angular momentum in the form of air rotation is induced by natural convection, the degeneracy is lifted by $\Delta\omega = \omega_+ - \omega_- = 2v_{av}/R_{eff}$, where v_{av} represents the average air velocity and R_{eff} is the effective radius of the circulator.



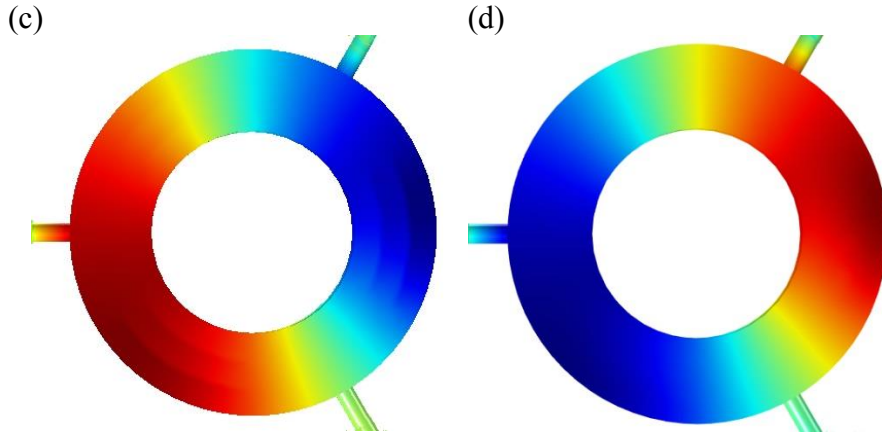


Figure 3-1. Model configuration and pressure distribution. (a) Geometrical top view of cross-section at $H = 22$ mm. The red region is specified as high temperature region is heated at a given temperature that is 373.15 K, 423.15 K, 473.15 K, 523.15 K, 573.15 K and 623.15 K, respectively. The rest blue area is set as a balanced temperature 273.15 K. (b) The acoustic pressure distribution in the condition of the optimal nonreciprocal performance with all the dimensions labeled. The pressure distribution of the clockwise (c) and counterclockwise (d) dipole modes of the acoustic circulator corresponding to the azimuthal order to be $m=1$.

3.3 Velocity distribution of heat-induced natural convection

Natural convection is a heat transporting process, in which the fluid motion is not created by external sources but by the spatial density differences due to the temperature gradient. In the acoustic circulator with a controlled temperature distribution, the fluid in the heated region becomes less dense and rises, while the fluid in the cooler region moves downside forming an air-circulating cycle. In order to form a steady circulating velocity field, the high temperature and low temperature regions are controlled by specific heat fluxes to maintain relative balanced temperature distribution. Normally, the internal driving force of natural convection comes from fluid density difference induced buoyancy, which would be affected by factors[175], such as temperature gradient, density difference, gravity, distance through the convective medium, diffusion rate and viscosity, through which dynamic control can be easily realized.

The contours and vectors of velocity field distributions in different temperature gradients are illustrated in Figure 3-2. The obtained velocity field is then used to calculate acoustic transmission in this biasing circulator by Aeroacoustics Module in *COMSOL*. As is shown in Figure 3-2, the high temperature region is placed in the lower left corner, which takes up a quarter of this circulator, and the rest region is kept at a relative balanced temperature 273.15 K by ice-water bath. For a fully developed and steady state air flow in this circulator, the average velocity on the left side is higher than the velocity on the right side, which could contribute better to the unidirectional acoustic propagation incident from the left channel. Moreover, the maximum velocity will also increase with the increase of temperature gradient. Three groups of thin heating layers also act as flow deflectors that can be used to facilitate the formation of a relatively more uniform and higher velocity distribution to achieve better nonreciprocal performance (More details in the supplementary material).

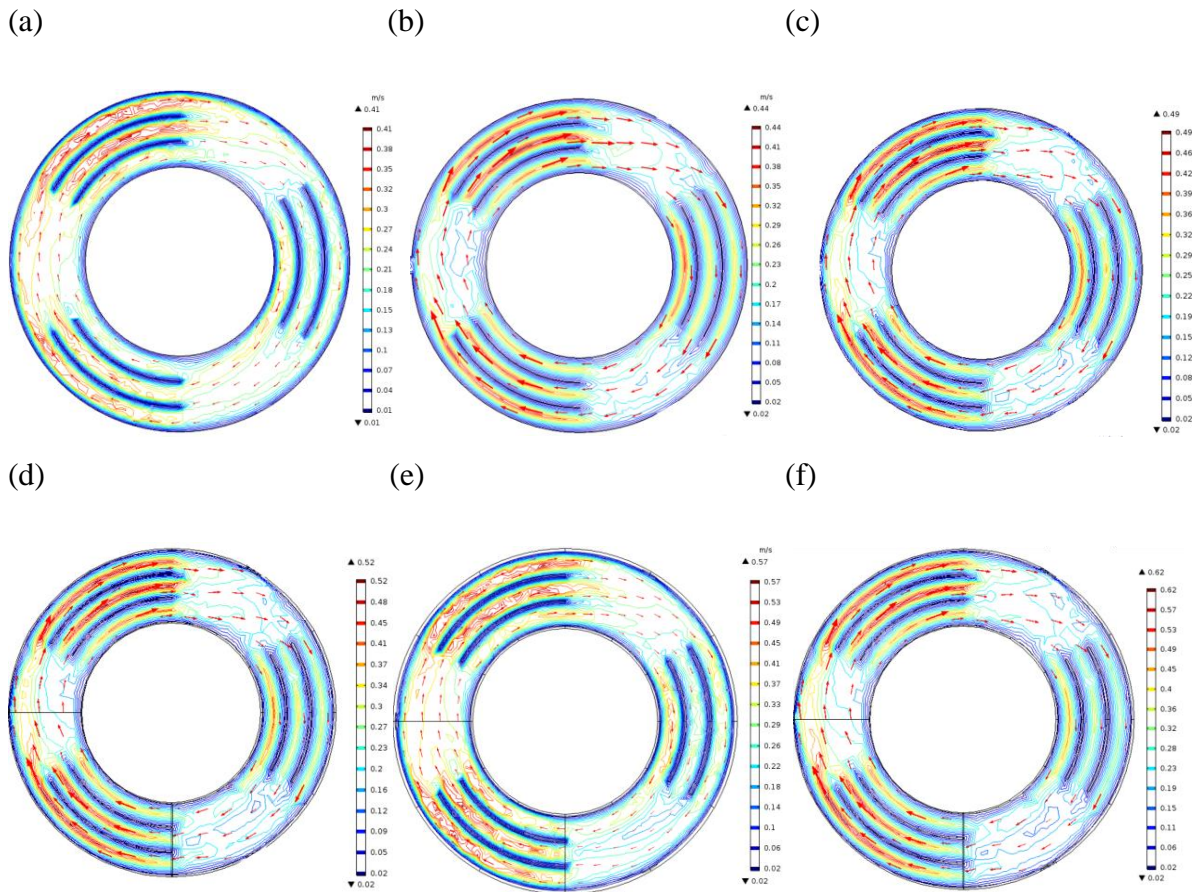


Figure 3-2. The contours and vectors of velocity field distributions in different temperatures. The high temperature region is set as (a) 373.15 K, (b) 423.15 K, (c)

473.15 K, (d) 523.15 K, (e) 573.15 K, (f) 623.15 K, respectively. The arrows show the velocity vectors.

3.4 Nonreciprocal performance

Modeling of the complex coupling of air flow and acoustics can be achieved by *COMSOL Multiphysics* and the add-on Acoustics Module using the linearized Navier-Stokes Module interfaces, which allows robust simulation of complex flow-acoustics interaction that leads to flow-dependent acoustic property change. This Acoustic Module offers a detailed analysis of turbulent and non-isothermal flow that influences the acoustic field in this system. This module takes all the energy dissipation from viscous loss and thermal loss into account, while do not include flow-induced noise source terms. Basically, the full linear perturbation to the general equations of CFD (computational fluid dynamics)-mass, momentum, and energy conservation can be solved using the Eq. (3-1)-Eq. (3-3).

The linearized Navier-Stokes equations represent a linearization to the full set of governing equations for a compressible, viscous, and non-isothermal flow[176]. Here, it is performed as the first-order perturbation around the steady-state background flow defined by its pressure, velocity, temperature, and density (p_0 , u_0 , T_0 , and ρ_0). This yields the governing equations for the propagation of small acoustic perturbations in the pressure, velocity, and temperature (p' , u' , and T'). In the perturbation theory, a superscript $'$ is used to denote variables of the first-order perturbations. The governing equations (with subscript 0 on the background fields) are:

$$\rho_0 C_p \left(\frac{\partial T'}{\partial t} + \mathbf{u}' \cdot \nabla T_0 + \mathbf{u}_0 \cdot \nabla T' \right) + \rho C_p (\mathbf{u}_0 \cdot \nabla) T_0 - \alpha_p T_0 \left(\frac{\partial p'}{\partial t} + (\mathbf{u}' \cdot \nabla) p_0 + (\mathbf{u}_0 \cdot \nabla) p' \right) - \alpha_p T' (\mathbf{u}_0 \cdot \nabla) p_0 = \nabla \cdot (k \nabla T') + \Phi + \mathbf{Q} \quad (3-1)$$

$$\rho_0 \left[\frac{\partial \mathbf{u}'}{\partial t} + (\mathbf{u}' \cdot \nabla) \mathbf{u}_0 + (\mathbf{u}_0 \cdot \nabla) \mathbf{u}' \right] + \rho' (\mathbf{u}_0 \cdot \nabla) \mathbf{u}_0 = \nabla \cdot \boldsymbol{\sigma} + \mathbf{F} - \mathbf{u}_0 M \quad (3-2)$$

$$\frac{\partial \rho'}{\partial t} + \nabla \cdot (\rho' \mathbf{u}_0 + \rho_0 \mathbf{u}') = M, \quad (3-3)$$

where M , F , and Q represent different source terms, Φ is the viscous dissipation function, σ is the stress tensor, and normally in frequency domain, the time derivative $\partial/\partial t$ can be denoted by

harmonic dependence $i\omega$, and w is defined as frequency. The standard hard wall boundary conditions and perfectly matching layers have been assigned in the simulation process.

Numerical simulations of the heat-induced natural convection based acoustic circulator in dipole mode are performed to investigate nonreciprocal acoustic propagation. As is shown in Figure 3-3(a), the acoustic pressure amplitude of transmission coefficient at Port 2 and Port 3 in the absence of angular-momentum biasing at two output ports are identical and equal to 0.691 due to the symmetric splitting circular structure, with the remaining 1/9 of acoustic power being reflected or dissipated. Figure 3-3(a) nevertheless displays, in the condition of the acoustic circulator with angular-momentum biasing, the transmission coefficient of output Port 3 is proportional to the temperature in high temperature region and could reach a maximum value of more than 0.9 at 623.15 K. On the contrary, the related transmission coefficients of output Port 2 decreases, and can be less than 0.1. Actually the velocity field created by the heat-induced natural convection can lead to robust nonreciprocal acoustic transmission, even by a small temperature gradient, indicating that the proposed acoustic nonreciprocal circulator is robust.

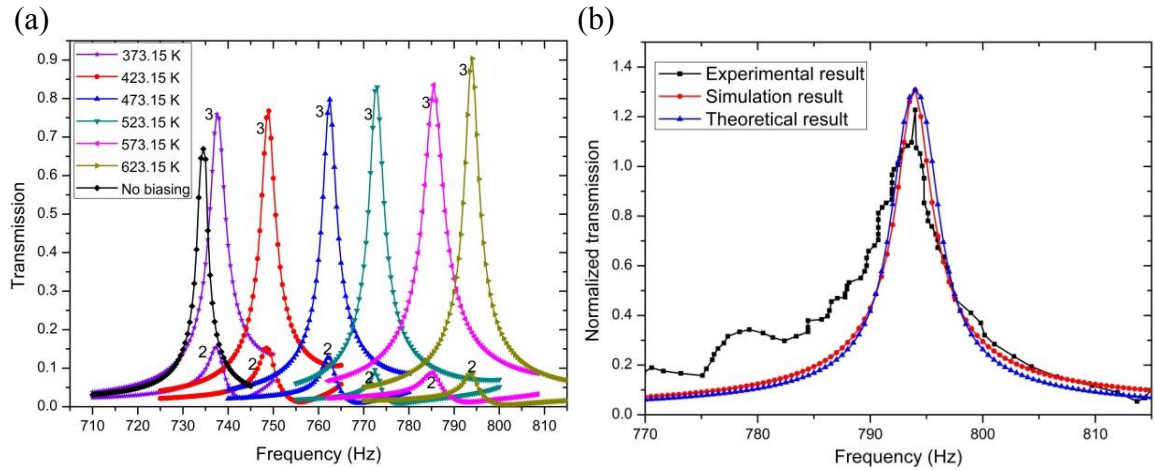


Figure 3-3. Nonreciprocal performance in different temperatures and the comparison with experimental and theoretical results. (a) Transmission coefficients at different high temperatures for Port 2 (curves with lower peak values) and Port 3 (curves with higher peak values). (b) Comparison of normalized transmission among *Alu*'s experimental results[31], theoretical results (Eq. (3-6)) and the simulation results of the biasing velocity distribution induced by the applied high temperature at 623.15 K.

In Figure 3-3(b), all the full-wave simulation and theoretical results are compared with the experimental results, which show good agreement, once the average value of the heat-induced velocity distribution matches the value from *Alu's* model[31]. As stated above, by varying the heating temperature, different interior velocity distributions can be easily obtained and the optimal nonreciprocal effect can be achieved when the temperature of the heated region is 623.15 K. The optimal velocity predicted by the analytical model coincides well with the average value of the velocity field. As predicted in the former analytical theory, the transmission to Port 2 can be reduced to zero at the operating frequency ω_0 , whereas the transmission to Port 3 is close to unity, which indicates almost all the acoustic power is transmitted to Port 3. These results show the correct amount of acoustic Zeeman splitting to achieve well-performed acoustic circulators with natural convection by a wide range of temperature gradients, enabling the dynamic control with minor temperature gradient for robust nonreciprocal acoustic transmission in specific structures.

The acoustic pressure distributions in an unbiased condition (Supplementary Figure S3-1(b)) and the biased conditions induced by natural convection (Figure 3-1(c) and 3-1(d)) are compared to fully understand the mechanism of the proposed design. For the unbiased condition, the resonant dipole modes are degenerate and evenly excited, resulting in a symmetric acoustic pressure distribution with respect to the axes of three ports in this cavity. While for the biased condition, the resonant dipole modes are split to produce an asymmetric field distribution for all the output ports. Specifically, the acoustic transmission in Port 2 is very small, while it in Port 3 is close to 1, which confirms a robust nonreciprocal acoustic transmission in the proposed acoustic circulator design. In addition, the selection of heated regions and temperature ranges can be adjusted to realize dynamic control of acoustic transmission direction and its nonreciprocal performance. In this scenario, the acoustic energy is routed exclusively in one direction and is easy to realize dynamic control without any moving components.

3.5 Coupled-mode theory for an acoustic circulator by angular-momentum bias

The modified coupled-mode theory[34, 155, 177] is developed as an analytical solution to describe the acoustic propagation in the circulator under angular-momentum bias considering

acoustic energy dissipation, which agrees well with the full-wave simulation results conducted by *COMSOL Multiphysics*. Based on the model of an azimuthally symmetric acoustic circulator under angular-momentum bias, the scattering parameters $S_{i1} = S_i^- / e^{-i\omega t}$ can be achieved according to Eq. (3-4)-Eq. (3-6), which represent reflection coefficient and transmission coefficients for Ports 1, 2 and 3, respectively, as:

$$S_{11} = -1 + e^{\varphi_{11}} \left(\sqrt{\frac{2\gamma_+}{3}} \alpha_+ + \sqrt{\frac{2\gamma_-}{3}} \alpha_- \right) \quad (3-4)$$

$$S_{21} = e^{\frac{2\pi i}{3} + \varphi_{21}} \sqrt{\frac{2\gamma_+}{3}} \alpha_+ + e^{-\frac{2\pi i}{3} + \varphi_{21}} \sqrt{\frac{2\gamma_-}{3}} \alpha_- \quad (3-5)$$

$$S_{31} = e^{\frac{4\pi i}{3} + \varphi_{31}} \sqrt{\frac{2\gamma_+}{3}} \alpha_+ + e^{-\frac{4\pi i}{3} + \varphi_{31}} \sqrt{\frac{2\gamma_-}{3}} \alpha_- , \quad (3-6)$$

where, γ_{\pm} denotes the inverse of decay times to the output Ports 1, 2 and 3, which are located at the equally distributed positions $\varphi = 0, \frac{2\pi}{3}$ and $4\pi/3$, respectively, which normally can be denoted as $\gamma_+ = \gamma_- = \gamma$ owing to symmetry. The coefficient α_{\pm} is $\alpha_{\pm} = ie^{\varphi_{11}} \sqrt{\frac{2\gamma_{\pm}}{3}} / (w - w_{\pm} + i\gamma_{\pm})$, where the eigenfrequencies of the right and left-handed modes are given by $w_{\pm} = w_0 \pm v_{av}/R_{eff}$ when the cavity modes are split. w_0 is the resonance frequency and R_{eff} comes from the calculation of $w_0 = c_{eff}/R_{eff}$, where effective acoustic speed changes with air temperature in the form of $\sqrt{k' \cdot p/\rho}$, as k' is the ratio of specific heat. Optimal nonreciprocal performance can be achieved at $w_{\pm} = w_0 \pm \gamma_{\pm}/\sqrt{3}$. Moreover, considering the acoustic energy dissipation generated by the non-uniform velocity and temperature distribution, related damping coefficients φ_{11} , φ_{21} and φ_{31} are substituted in the transmission Eq. (3-4)-Eq. (3-6). More details can be found in the supplementary material.

3.6 Robust nonreciprocal acoustic circulator with other interior configurations

We've designed different interior structures to confirm that the heat-induced natural convection can form a robust nonreciprocal acoustic transmission in this type of acoustic circulator. As is shown in Figure 3-4(a-d), the interior structures of triangle, Y-parallel

triangles, hexagon and hexagram are placed vertically with a well-adjusted high temperature region and a low temperature region, which can form a steady velocity field therein. The triangle structure achieves a maximum velocity distribution, whereas the Y-parallel triangle structure gets a minimum velocity distribution. In Figure 3-4(e), the interior configurations of hexagon and hexagram obtain the best nonreciprocal performance, although their velocities are not the maximum ones. We can conclude that nonreciprocal performance is not only determined by the velocity distribution, but also the specific geometrical configuration. Moreover, in this type of acoustic circulator, the differences for transmission coefficients of two output ports are still big enough to obtain excellent nonreciprocal performance.

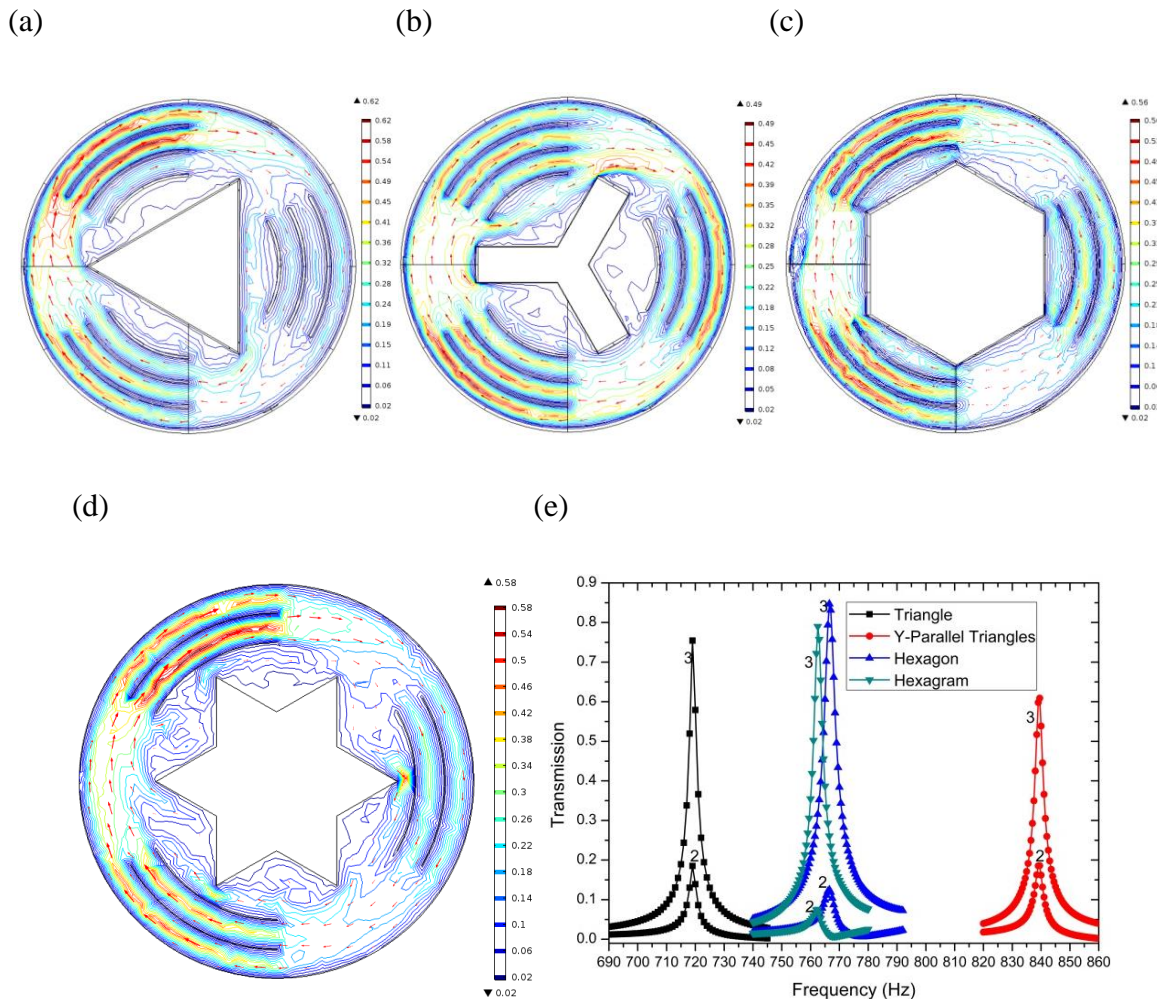


Figure 3-4. The velocity contours and nonreciprocal performance of acoustic circulators with four types of interior configurations, where temperature of the high temperature region is 523.15 K. The velocity contours and vector arrows for (a)

Triangle structure. (b) Y-parallel triangles structure. (c) Hexagon structure. (d) Hexagram structure. (e) Transmission coefficients for Port 2 (curves with lower peak values) and Port 3 (curves with higher peak values).

3.7 Discussion

We have reported that the heat-induced natural convection can be easily incorporated into acoustic circulators to realize nonreciprocal acoustic propagation in compact configurations without using moving components that may generate extra noise, taking a significant step towards the realization of nonreciprocal acoustics for practical applications. In many applied scenarios, compared to other methods of adopting external biasing variables, manipulating temperature gradient is convenient to realize and can be controlled more concisely. Our design confirms that the classical yet simple acoustic circulator with different temperature distributions can realize robust nonreciprocal acoustic propagation. Moreover, in order to demonstrate that the heat-induced natural convection is a facile way of generating steady velocity field in various structural configurations to realize nonreciprocal acoustic propagation, four types of interior structures are designed to verify the versatility and robustness in these circulator configurations. The simulation results show excellent nonreciprocal performance for the protection of interior structures, which also certifies the feasibility and reliability at the basis of coupling thermal control with nonreciprocal acoustics.

This work, by combining the concept of natural convection and aeroacoustics, opens a new practical paradigm in nonreciprocal acoustics, particularly for practical applications. Due to its noiseless, controllable, structurally flexible and size-compact merits, such acoustic nonreciprocal design will also lead to new applications in the miniaturization of nonreciprocal acoustic-related applications, such as ultrasonic components, MEMS devices and sound attenuation in circumstances with temperature control capability, which provides alternative and practical option for the design of nonreciprocal acoustics based on existing external flow-driven basing model.

3.8 Supplementary material

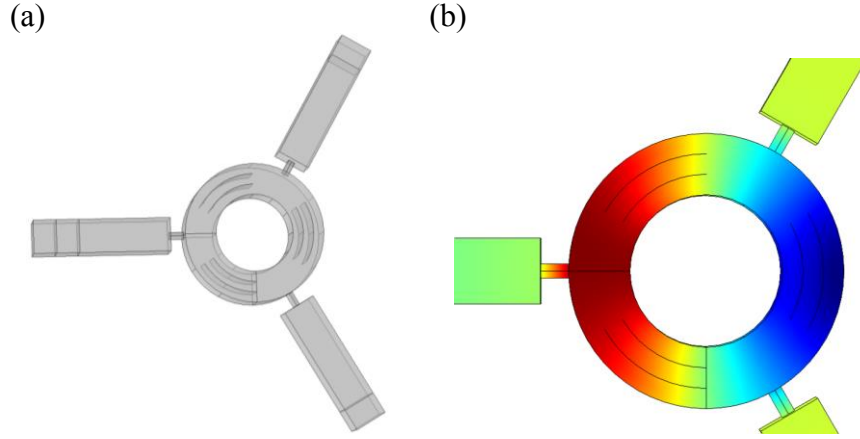


Figure S3-1| Detailed model configuration and mode analysis. (a) Detailed 3D model with interior deflectors evenly distributed. (b) The pressure distribution of the dipole mode of the acoustic circulator without angular-momentum biasing. The color from red to blue represents the value of pressure from positive maximum to negative maximum.

3.8.1. Governing equations for natural convection in the acoustic circulator

Our numerical model includes predefined Multiphysics coupling effect for the non-isothermal flow in which the density depends on temperature. Also, this model couples the compressible flow ($Ma < 0.3$) with heat transfer in fluid [175, 178], and the effect of thermal radiation. The Non-Isothermal Flow and Conjugate Heat Transfer interfaces incorporate the fully compressible formulation of the continuity and momentum equations. Some basic governing equations of heat transfer with radiation and compressible flow with gravity are written as,

$$\rho C_p \left(\frac{\partial T}{\partial t} + \mathbf{u} \cdot \nabla T \right) + \nabla \cdot [-k \nabla T + \varepsilon (G - n^2 \sigma T^4)] = \alpha_p T \left(\frac{\partial p}{\partial t} + \mathbf{u} \cdot \nabla p \right) + \tau : \nabla \mathbf{u} + Q \quad (\text{S3-1})$$

$$\rho \frac{\partial \mathbf{u}}{\partial t} + \rho (\mathbf{u} \cdot \nabla) \mathbf{u} = \nabla \cdot \left[-p \mathbf{I} + \mu (\nabla \mathbf{u} + (\nabla \mathbf{u})^T) - \frac{2}{3} \mu (\nabla \cdot \mathbf{u}) \mathbf{I} \right] + \mathbf{F} + \rho \mathbf{g} \quad (\text{S3-2})$$

$$\frac{\partial \rho}{\partial t} + \nabla \cdot (\rho \mathbf{u}) = 0, \quad (\text{S3-3})$$

where, ρ is density, C_p is the specific heat capacity at constant pressure, T is the absolute temperature, u is the velocity vector, k is the thermal conductivity, ε is the emissivity, G is the incoming radiative flux, n is the refractive index, σ is the Stefan–Boltzmann constant, α_p is the coefficient of thermal expansion, τ is the viscous stress tensor, Q contains heat sources other than viscous dissipation, F is the body force vector, and g is the gravity constant.

3.8.2. Couple-mode theory considering dissipation

According to the temporal coupled-mode theory based on Fano resonance in optical resonators, and also in combination of the 120-degree rotational symmetry this circulator, we can obtain the equation (S3-4). Here, \mathbf{K} and \mathbf{D} , represents the coupling coefficients between the resonances and the waves at the ports, respectively. This model is valid only when the characteristic length of the circulator is far smaller than the resonance frequency, which is confirmed in the simulation and experiment results. Moreover, considering the acoustic energy dissipation generated by the non-uniform velocity and temperature distribution, related damping coefficients φ_1 and φ_2 are imported in the transmission equations.

$$\mathbf{K}^* = \mathbf{D} = \begin{Bmatrix} e^{\varphi_{11}}\sqrt{2\gamma_+/3} & e^{\varphi_{11}}\sqrt{2\gamma_-/3} \\ e^{-\frac{2\pi i}{3}+\varphi_{21}}\sqrt{2\gamma_+/3} & e^{\frac{2\pi i}{3}+\varphi_{21}}\sqrt{2\gamma_-/3} \\ e^{-\frac{4\pi i}{3}+\varphi_{31}}\sqrt{2\gamma_+/3} & e^{\frac{4\pi i}{3}+\varphi_{31}}\sqrt{2\gamma_-/3} \end{Bmatrix} \quad (\text{S3-4})$$

The equation (S3-4) can then be substituted into the temporal coupled-mode theory consisting of a single-mode resonator coupled with 3 ports. Where the amplitudes a_+ and a_- of the clockwise and counterclockwise modes of this acoustic circulator under angular-momentum biasing can be denoted as:

$$\frac{da_+}{dt} = (-iw_+ - \gamma_+)a_+ + e^{\varphi_{11}}\sqrt{\frac{2\gamma_+}{3}}S_1^+ + e^{-\frac{2\pi i}{3}+\varphi_{21}}\sqrt{\frac{2\gamma_+}{3}}S_2^+ + e^{-\frac{4\pi i}{3}+\varphi_{31}}\sqrt{\frac{2\gamma_+}{3}}S_3^+ \quad (\text{S3-5})$$

$$\frac{da_-}{dt} = (-iw_- - \gamma_-)a_- + e^{\varphi_{11}}\sqrt{\frac{2\gamma_-}{3}}S_1^+ + e^{\frac{2\pi i}{3}+\varphi_{21}}\sqrt{\frac{2\gamma_-}{3}}S_2^+ + e^{\frac{4\pi i}{3}+\varphi_{31}}\sqrt{\frac{2\gamma_-}{3}}S_3^+ \quad (\text{S3-6})$$

where S_1^+, S_2^+ and S_3^+ are the excitation signals at related ports. The output signals S_1^-, S_2^- and S_3^- can be derived from the interferences of resonance-assisted coupling, coupling

through a direct pathway of the incoming and outgoing waves, and the acoustic energy dissipation. The related equations of output signals are shown as:

$$S_1^- = -S_1^+ + e^{\varphi_{11}} \left(\sqrt{\frac{2\gamma_+}{3}} a_+ + \sqrt{\frac{2\gamma_-}{3}} a_- \right) \quad (\text{S3-7})$$

$$S_2^- = -S_2^+ + e^{\frac{2\pi i}{3} + \varphi_{21}} \sqrt{\frac{2\gamma_+}{3}} a_+ + e^{-\frac{2\pi i}{3} + \varphi_{21}} \sqrt{\frac{2\gamma_-}{3}} a_- \quad (\text{S3-8})$$

$$S_3^- = -S_3^+ + e^{\frac{4\pi i}{3} + \varphi_{31}} \sqrt{\frac{2\gamma_+}{3}} a_+ + e^{-\frac{4\pi i}{3} + \varphi_{31}} \sqrt{\frac{2\gamma_-}{3}} a_- \quad (\text{S3-9})$$

Here, we assume the excitation is harmonic and only works at port 1 for $S_1^+ = e^{-i\omega t}$, $S_2^+ = S_3^+ = 0$. For the variable change of amplitudes $\alpha_{\pm} = a_{\pm} e^{-i\omega t}$, we can achieve the following equations:

$$-i\omega a_+ = (-i\omega_+ - \gamma_+) a_+ + e^{\varphi_{11}} \sqrt{\frac{2\gamma_+}{3}} \quad (\text{S3-10})$$

$$-i\omega a_- = (-i\omega_- - \gamma_-) a_- + e^{\varphi_{11}} \sqrt{\frac{2\gamma_-}{3}} \quad (\text{S3-11})$$

Then we can achieve the solutions displayed in the article as:

$$\alpha_{\pm} = i e^{\varphi_{11}} \sqrt{\frac{2\gamma_{\pm}}{3}} / (\omega - \omega_{\pm} + i\gamma_{\pm}) \quad (\text{S3-12})$$

$$S_{11} = -1 + e^{\varphi_{11}} \left(\sqrt{\frac{2\gamma_+}{3}} \alpha_+ + \sqrt{\frac{2\gamma_-}{3}} \alpha_- \right) \quad (\text{S3-13})$$

$$S_{21} = e^{\frac{2\pi i}{3} + \varphi_{21}} \sqrt{\frac{2\gamma_+}{3}} \alpha_+ + e^{-\frac{2\pi i}{3} + \varphi_{21}} \sqrt{\frac{2\gamma_-}{3}} \alpha_- \quad (\text{S3-14})$$

$$S_{31} = e^{\frac{4\pi i}{3} + \varphi_{31}} \sqrt{\frac{2\gamma_+}{3}} \alpha_+ + e^{-\frac{4\pi i}{3} + \varphi_{31}} \sqrt{\frac{2\gamma_-}{3}} \alpha_- \quad (\text{S3-15})$$

In different heat induced angular-momentum biasing field, the damping coefficients φ_{11} , φ_{21} and φ_{31} are different. In Figure S3-2, the theoretical prediction of S parameters are based on the simulation results for the definition of the damping coefficients.

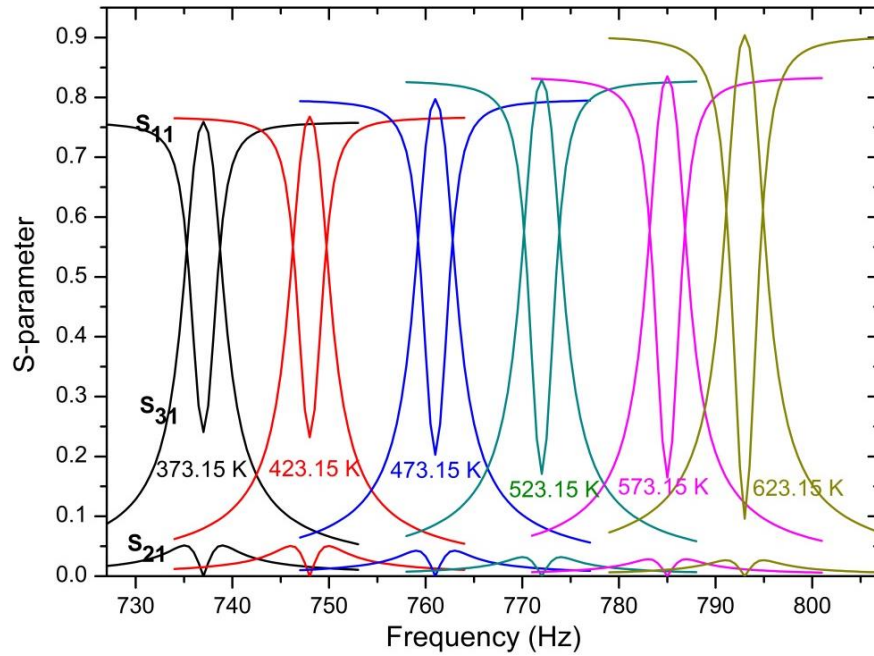


Figure S3-2| Scattering parameters. Magnitude of the scattering parameters versus frequency for different velocity distributions of the temperature gradient induced biasing.

Chapter 4

4 Miniaturization of Floquet topological insulators for airborne acoustics by thermal control

The acoustic topological insulator is a revolutionary design to control acoustics in isolation and broadband unidirectional transmission, which is topologically robust and immune to structural disorders or defects. Currently, these fascinating properties have been investigated through fan-induced moving media, acoustic capacitance adjustment and acoustic metamaterials. However, most of them are still associated with disadvantages including extra noise, bulky volume and limited dynamic controlling performance. In this study, we overcome these limitations by introducing a modulation scheme of temperature difference in a lattice of resonators to demonstrate that the Floquet topological insulators with thermal control can realize topologically robust and nonreciprocal acoustic propagation. This controlling strategy provides an alternative platform to conduct acoustic topological applications, especially for noiseless and miniaturized airborne acoustics. Thermal modulation provides possibility to miniaturize topological airborne acoustics into millimeter scale or even smaller. It is noted here, this Chapter is based on author's publication: Liu, Xingxing, Qiuquan Guo, and Jun Yang. "Miniaturization of Floquet topological insulators for airborne acoustics by thermal control." *Applied Physics Letters* 114.5 (2019): 054102. And all the figures are used with the permission from ref. [127].

4.1 Introduction

The development of topological insulators has had a profound impact in condensed matter systems.[9, 16] Such insulator systems host robust one-way edge transmission against structural disorders[179] or defects.[180] Studies have demonstrated that the analogous topological insulators can lead to significant possibilities when extended to classical photonic[181-183] or acoustic systems[33, 45, 46, 126, 157, 184]. Specifically, for acoustic systems, some attempts[130, 180, 185, 186] have been made to construct topological ordered edge states by emulating the quantum Hall effect, breaking time-reversal symmetry, and forming internal or lattice symmetries.[131, 168, 187] In most acoustic application scenarios, structural disorders or defects coupling with backscattering waves in transmission process,

leads to a significant and pivotal issue of impedance matching in engineering acoustic systems.

Recently, many strategies of breaking time-reversal symmetry have been investigated by introducing rotational motion[31, 32] or angular momentum[34] in topological acoustic systems. Zhang et al.[72] applied different heights of acoustic honeycomb lattice with inversion symmetry breaking to form an acoustic analogue of a gapped graphene monolayer. For acoustics in liquids, Alu et al.[126] proposed the idea of acoustic Floquet topological insulators with weak spatiotemporal modulation to realize capacitance adjustment in trimer metamolecules. However, implementing uniform motion in a resonator encounters many challenges, including acoustic energy losses, extra noise, and bulky configuration, which may become detrimental in most acoustic application scenarios.

In this study, we investigate the miniaturization of Floquet topological insulators for airborne acoustic systems based on the modulation of acoustic impedance. This modulation scheme possesses the ability to eliminate impedance matching challenges. This is achieved in an acoustic double-trimer lattice whose impedance matching is modulated by separating temperature distributions in each metamolecule, demonstrating the acoustic analogue of Floquet topological insulators. Different from Alu's[126] on-site rotating modulation scheme in liquid, we demonstrate that the temperature-based modulation of acoustic impedance matching can function well in airborne topological acoustic systems, especially for the miniaturization of these systems. This opens a new avenue for practical applications of acoustic topological insulators.

Specifically, different temperatures can induce different acoustic impedances as density and acoustic speed change in distributed metamolecules of each trimer, which is exploited as the basis of modulation strategy. As the airborne acoustic impedance of metamolecules can be modulated in an effective manner, up to tens of percents, this method opens the possibility to design topologically protected, broadband, noiseless, dynamic controlling, and miniaturized (approximately 1/10 of other models[31, 32, 34] in size, due to the existence of lumped impedance matching units) acoustic topological systems, including a broadband acoustic topological insulator, and a nonreciprocal acoustic array which is robust to impedance

disorders. We employ a rigorous full-wave acoustic transmission[188] and band gap simulation (all simulations are performed by COMSOL Multiphysics) to demonstrate the possibility of Floquet topological insulators and their related applications to practical devices for airborne acoustic engineering.

4.2 Prototype design and mode analysis

The acoustic system we propose in this work is shown in Figure 4-1. An acoustic hexagonal lattice array is formed by the unit of double-trimer acoustic lattice, as shown in Figure 4-1(a). Each trimer consists of three acoustic hollow circulators interconnected by cylindrical waveguides, which can work as resonant acoustic metamolecules. The inner and outer radii of the hollow circulator are set as 5 mm and 10 mm (R_{inner} and R_{outer}), respectively. The fundamental waveguide mode for an acoustic plane wave is supported in the studied frequency range. To realize dynamic control of acoustic impedance (Figure 4-1(b)) for every hollow circulator, we control the heat flux to keep each hollow circulator at a relative constant temperature, which can be realized by immersing each circulator into the different temperature circumstances. The detailed setup includes; heated oil circumstance for highest temperature, ice water for 0 °C, and heated water for middle-high temperature with a feedback control. The proposed realization is speculative and not yet verified experimentally. The interconnected waveguides are made of adiabatic material to avoid heat conduction. Each hollow circulator can be modelled as a lumped element[126] storing acoustic energy, which can be described on the basis of acoustic impedance $Z = \rho c$. For the working temperature range in this study, a trimer consists of three hollow circulators are considered as a L-C resonating circuit, supporting a doubly degenerate dipolar resonance at 6.85-7 kHz associated with the resonant exchange of kinetic and potential energy among the coupling waveguides and the hollow circulators (Figure 4-1(c)). As shown in Figure 4-1(d), the next resonant range, occurring at 8.6-8.85 kHz, is formed by one degenerate dipolar resonance.

To break time-reversal symmetry and induce topologically nontrivial properties in this resonant acoustic circulator array, the acoustic impedance of each circulator is modulated by on-site impedance matching as the temperature distribution changes. As it is shown in Figure 4-1(b), this modulation protocol of the double-trimer lattice is almost uniform within each circulator, while due to the surface radiation and thermal convection there is a gradient in the

connected channels. Specifically, as the temperature is set as variable, acoustic speed is defined as $c = \sqrt{\frac{\gamma RT}{\mu}}$ and air density is $\rho = \frac{P}{RT}$, where γ represents the adiabatic index, R , μ , T and P are defined as the molar gas constant, the mean molar mass of air, the air temperature, and the ambient pressure, respectively. Acoustic impedance will decrease with the increase of temperature (Supplementary Figure S4-1(b)). Impedance modulation up to tens of percents is easy to achieve using suitable temperature controlling strategies, which may be leveraged to further increase the bandwidth of the topologically nontrivial band gap (Figure 4-1(e)). Moreover, when thermal modulation is applied, the band structure folds along the frequency axis. By introducing impedance modulation to break temporal symmetry, degeneracy is lifted by some degrees related to the modulation scheme at the diagonal direction of the double-trimer lattice. Black lines show the band structure for such a unit lattice in which the band gap opens at the k_x direction in the frequency ranges of two dipolar resonances. Dipolar modes can be considered as a superposition of counter-rotating band states $p_x \pm ip_y$, which is similar to the rotating modulation strategy. K and K' points also coincide well with the peak-transmission frequencies.

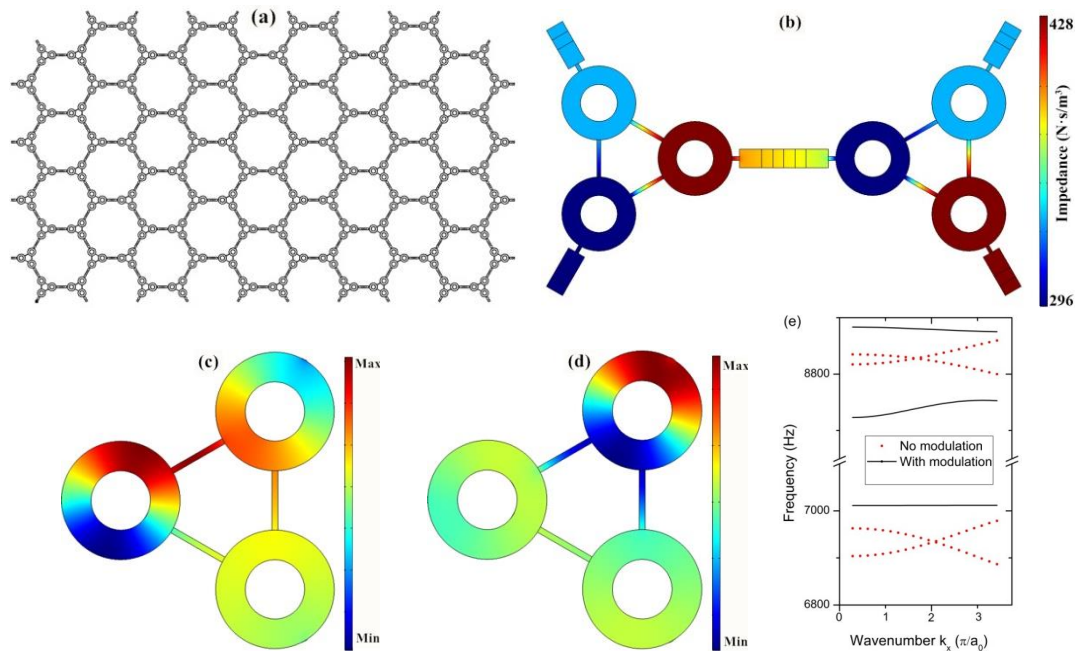


Figure 4-1. (a) The hexagonal lattice of acoustic trimers. Each trimer is composed of three connected hollow circulators and rectangular channels. The inner media is air.

(b) The periodically modulated and distributed acoustic impedance of each circulator, with the modulation scheme of 0 °C, 90 °C and 300 °C throughout the double-trimer lattice. (c) A doubly degenerate dipolar resonance at 6.85-7 kHz. (d) The next resonant range, occurring at 8.6-8.85 kHz, due to one degenerate dipolar resonance. The colour legend denotes the acoustic pressure distribution. (e) Comparison between the band structure with (black curves) or without (red dots) modulation.

A semi-analytical model[137, 155] considering the impedance matching issue for the calculation of the transmission coefficients at output ports 1 and 2 is,

$$T_{0 \rightarrow 1} = \left| \frac{2}{3} \left(\frac{e^{-\frac{4\pi i}{3}}}{1 - \frac{i(w-w_-)}{\gamma_-}} + \frac{e^{-\frac{2\pi i}{3}}}{1 - \frac{i(w-w_+)}{\gamma_+}} \right) \right| \quad (4-1)$$

$$T_{0 \rightarrow 2} = \left| \frac{2}{3} \left(\frac{e^{-\frac{2\pi i}{3}}}{1 - \frac{i(w-w_-)}{\gamma_-}} + \frac{e^{-\frac{4\pi i}{3}}}{1 - \frac{i(w-w_+)}{\gamma_+}} \right) \right| \quad (4-2)$$

where, γ_{\pm} denotes the inverse of related decay times to the input port (port 0), output port 1 and 2, which are located at the azimuthal positions $\varphi = 0, 2\pi/3$ and $4\pi/3$, respectively. Due to symmetry, γ_+ and γ_- are usually equal, i.e. $\gamma_+ = \gamma_- = \gamma$. In order to achieve $T_{0 \rightarrow 1} = 1$ and $T_{0 \rightarrow 2} = 0$ at the frequency $w = w_0$, when the cavity modes are split, the optimal nonreciprocal performance (the ratio of $T_{0 \rightarrow 1}/T_{0 \rightarrow 2}$ is maximum or minimum) can be achieved at $w_{\pm} = w_0 \pm \gamma_{\pm}/\sqrt{3}$. After considering the eigenfrequencies of the right and left-handed modes given by $w_{\pm} = w_0 \pm mc_{eff}/R_{eff}$, we can get the optimal analogous speed (in the condition of optimal nonreciprocal performance) created by impedance modulation is $c_{opt} = \gamma R_{eff}/\sqrt{3}$. The integer number m is the azimuthal order. w_0 is the resonance frequency and $R_{eff} = (R_{inner} + R_{outer})/2$ is the effective radius. This trimer structure can be considered as three interconnected lumped elements, and the related impedance is $Z_i = \rho c = (\rho_0 + \rho_i)(c_0 + c_i)$. We can employ the impedance translation theorem[188] or simulation results to obtain the effective impedance Z_{eff} and the effective density ρ_{eff} for the whole trimer unit, while the effective speed is set as $c_{eff} = \frac{Z_{eff}}{\rho_{eff}} - c_0$. The related design strategy can be based on that.

4.3 Topological performance

As it is shown in Figure 4-2, different groups of temperature-distribution-modulation schemes are applied to investigate nonreciprocal performance in each trimer unit (one input port connecting with two output ports), which is significant to guide the design of topological device. Generally, higher temperature distribution difference exhibits better and wider broadband nonreciprocal performance. In terms of acoustic output energy difference, the related ratio of the the highest temperature output port divided by the middle-high temperature output port can be in the range of 4-100, which means the major acoustic energy would transmit in one direction in peak frequency ranges. Efficient nonreciprocal performance is demonstrated in two resonant frequency regions, even in a small temperature gradient within three metamolecules of each trimer. This investigation certifies an efficient acoustic nonreciprocal performance can be achieved within a wide thermal modulation. The following modulation disorder robustness and impedance matching (see Figure S4-2 in supplementary material) issue are designed based on the efficient nonreciprocal performance within a lattice of acoustic Floquet topological insulators. Moreover, as stated by Alu et al,[47] this type of impedance modulation scheme has the capability of breaking time-reversal symmetry, while this modulation is also too weak to resonantly couple different Floquet orders. The opened band gap has topological nature of the first Chern class[51] as expected, which is characterized by a non-vanishing topological invariant.[126] To understand the topological properties induced by the impedance modulated system a semi-analytical approach based on the derivation of the effective Hamiltonian of the impedance-dependent tight-binding model[53] is proposed (see section 3 of supplementary material). This allows a traditional characterization of this modulated topological system based on topological invariants.

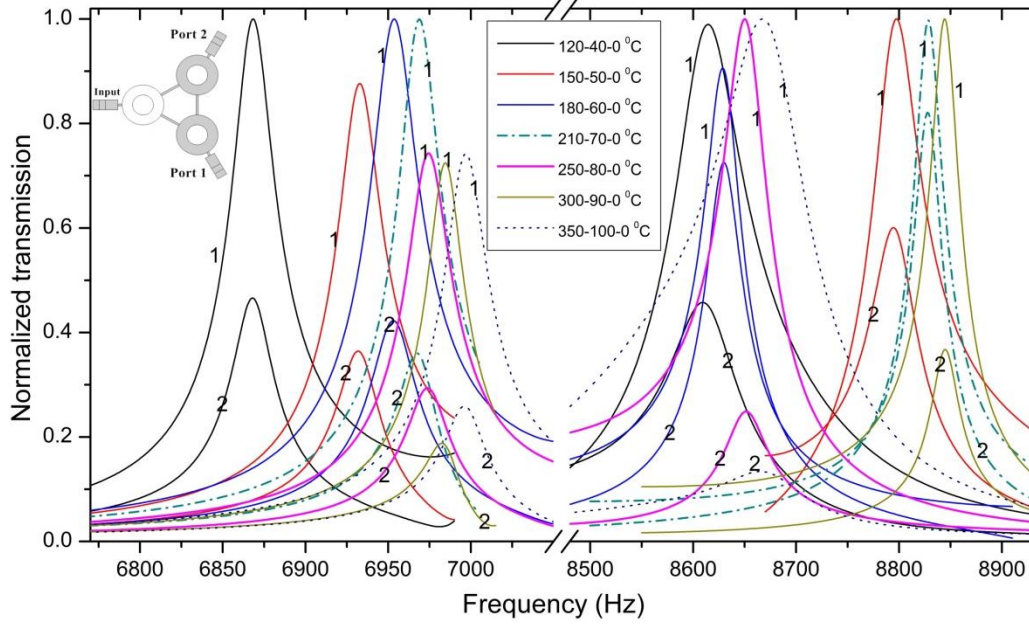


Figure 4-2. Normalized transmission coefficients of pressure at different temperature distributions in a single trimer (the upper left inserted trimer structure), as the temperature distribution of the acoustic input metamolecule remains is 0 °C, while two outputs are shown in the above legend. Curves with same colour represents the output values in two output ports, for the highest temperature output port relates to the upper curve (port 1) and the middle-high temperature output port relates to the lower curve (port 2).

As it is shown in Figure 4-3, the acoustic transmission edge states based on Floquet topological insulators are robust against impedance modulation disorders. This extraordinary property is demonstrated by this input-output numerical experiment. In Figure 4-3(a), the impedance modulation scheme of each double-trimer lattice is perfectly ordered with mirror symmetry vertically, as the colours of red, green and yellow represent acoustic impedances induced by specific increasing temperatures. This regular array is compared with the disordered scenario as shown in Figure 4-3(c), whose trimers in the double-trimer lattice are not mirror symmetric but with anticlockwise rotating strategy. However, as it is shown in Figure 4-3(b, d), the acoustic intensity distributions all display the route of one-way edge transmission, demonstrating the topological protection is not affected by the modulation scheme within the lattice. Small part of the acoustic energy transmits into the bulk because a

Floquet insulators system in ideal condition should have infinite units to avoid reflection in edge, or the temperature modulation should be further improved to achieve better effect. The handedness of the modulation scheme within the trimers mostly defines the topological properties of this lattice structure. Thus, our modulation scheme based on the change of temperature in each metamolecule does not have to be specific or uniform throughout the lattice structure. The strategy of changing temperature owns advantages in realizing dynamic control and possibility of miniaturization for topological insulator structures. Fundamentally, the on-site part of the Hamiltonian can decouple the effect of the modulation from the phase of the Bloch state.[189] This is possible as the resonant nature of trimers guarantees that the on-site energy is confined within each resonator. Moreover, by tailoring boundaries with or without modulation, excitation of a one-way edge mode and its propagation along an irregularly shaped domain wall are observed (section 3 of supplementary material). Our design based on Floquet topological insulators, takes a significant step towards the practical applications of topologically protected, broadband and dynamic controlling acoustic systems.

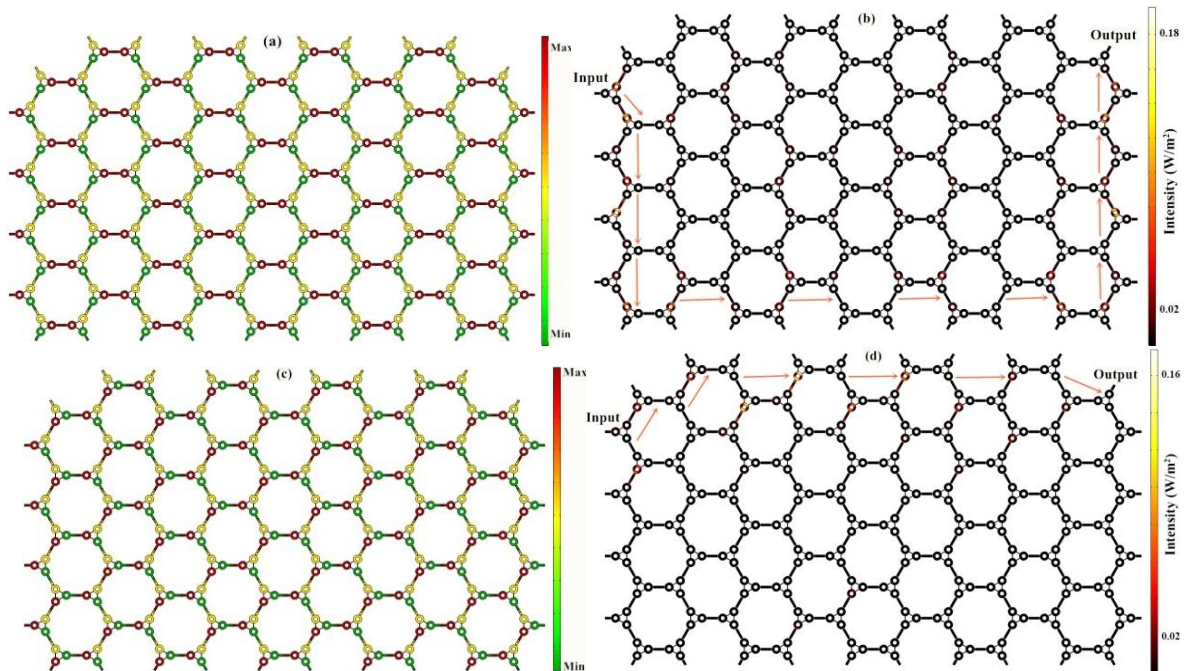


Figure 4-3. (a) The simplified modulation scheme for two trimers in the double-trimer lattice are mirror symmetric with each other, as the colours of red, yellow and green represent acoustic impedances induced by the temperatures of 0 °C, 300 °C and 90 °C, respectively. (b) The one-way edge transmission in the modulation scheme of (a), as the arrows show a lower transmission edge route. (c) The modulation scheme for every

double-trimer lattice is not mirror symmetric, while the right trimer is anticlockwise rotating around the left trimer. (d) The edge transmission in the modulation scheme of (c), as the arrows also show an upper transmission edge route.

In this work, the design of the Floquet topological insulator systems based on the thermal modulation is applied to demonstrate efficient topological performance with the possibilities of broadband transmission, dynamic control and miniaturization. Different from the previously studied modulation methods, such as introducing fluid flow within cavities or controlling the volume of each metamolecule, the designed modulation disorder systems and topologically protected edge mode directly control the temperature in each metamolecule. This helps to realize different effects of acoustic impedance matching for trimer units, which can host gapless edge states. This unique controlling strategy can expand the engineering toolkit of acoustic topological applications, especially in the area of miniaturization of airborne acoustics, as thermal control can support lumped elements to generate the effect of breaking time-reversal symmetry.

4.4 Supplementary material

4.4.1. Acoustic transmission model configuration and simulation

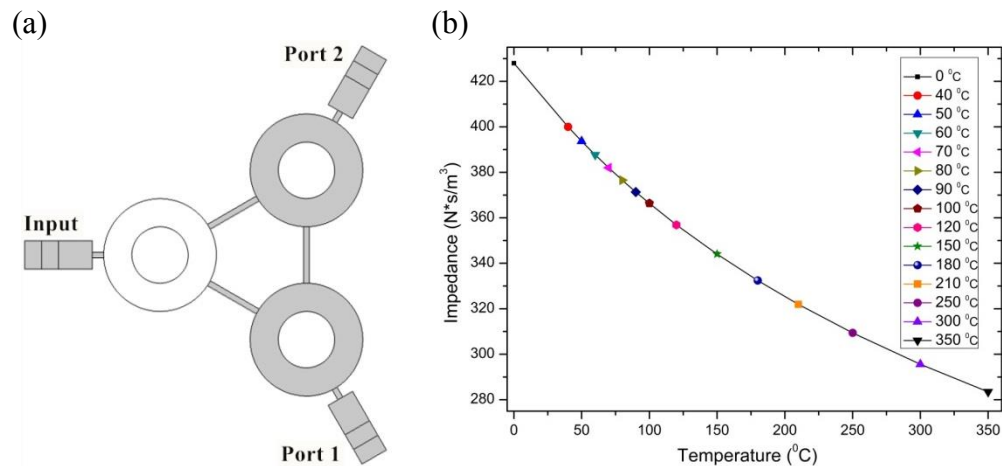


Figure S4-1| Detailed model configuration and impedance. (a) This trimer unit has one input port and two output ports. (b) The acoustic impedance changes in different temperature.

As shown in Figure S4-1(a), the inner and outer radii of the hollow circulator are set as 5 mm and 10 mm, respectively. The distance between two closest hollow circulators is 30 mm. The interconnected channel within trimer structure is with the width of 1 mm. For the channel connecting two trimer structures, the width is 5 mm and the length is 24 mm. There are one input port and two output ports.

For the thermal simulation, we employed the simulation of thermal modulation, considering the surface radiation and air convection inside all the hollow structures. Our numerical model includes predefined Multiphysics coupling effect for the non-isothermal flow in which the density depends on temperature. Also, this model couples the compressible flow ($Ma < 0.3$) with heat transfer in fluid [175, 178], and the effect of thermal radiation. The Non-Isothermal Flow and Conjugate Heat Transfer interfaces incorporate the fully compressible formulation of the continuity and momentum equations. Some basic governing equations of heat transfer with radiation and compressible flow are written as,

$$\rho C_p \left(\frac{\partial T}{\partial t} + \mathbf{u} \cdot \nabla T \right) + \nabla \cdot [-k \nabla T + \varepsilon(G - n^2 \sigma T^4)] = \alpha_p T \left(\frac{\partial p}{\partial t} + \mathbf{u} \cdot \nabla p \right) + \tau : \nabla \mathbf{u} + \mathbf{Q} \quad (\text{S4-1})$$

$$\rho \frac{\partial \mathbf{u}}{\partial t} + \rho(\mathbf{u} \cdot \nabla) \mathbf{u} = \nabla \cdot \left[-p \mathbf{I} + \mu(\nabla \mathbf{u} + (\nabla \mathbf{u})^T) - \frac{2}{3} \mu(\nabla \cdot \mathbf{u}) \mathbf{I} \right] + \mathbf{F} \quad (\text{S4-2})$$

$$\frac{\partial \rho}{\partial t} + \nabla \cdot (\rho \mathbf{u}) = 0, \quad (\text{S4-3})$$

where, ρ is density, C_p is the specific heat capacity at constant pressure, T is the absolute temperature, \mathbf{u} is the velocity vector, k is the thermal conductivity, ε is the emissivity, G is the incoming radiative flux, n is the refractive index, σ is the Stefan–Boltzmann constant, α_p is the coefficient of thermal expansion, τ is the viscous stress tensor, \mathbf{Q} contains heat sources other than viscous dissipation, and \mathbf{F} is the body force vector.

By adjusting heat flux to different lumped element in each trimer, we can achieve relative distributive constant temperatures. In Figure S4-1(b), the acoustic impedance as the change of temperature is displayed. We can easily find that the modulation of each trimer can be tens of percents for impedance. For the full-wave numerical experiment of acoustic topological performance, we coupled the simulated thermal modulation distributions of air density and temperature with full-wave acoustic simulation to achieve the acoustic transmission process.

4.4.2. Acoustic analogue of couple-mode theory

According to the temporal coupled-mode theory[137, 155] based on Fano resonance[137] in optical resonators, and also in combination of the 120-degree rotational symmetry this trimer unit, we can obtain the equation (S4-4). Here, \mathbf{K} and \mathbf{D} , represents the coupling coefficients between the resonances and the waves at the azimuthal positions $0, 2\pi/3$ and $4\pi/3$, which corresponds to the input port, port 1 and port 2, respectively. This model is valid only when the characteristic length of the circulator is far smaller than the resonance frequency, which is confirmed in the simulation results.

$$\mathbf{K}^* = \mathbf{D} = \left\{ \begin{array}{cc} \sqrt{2\gamma_+/3} & \sqrt{2\gamma_-/3} \\ e^{-\frac{2\pi i}{3}} \sqrt{2\gamma_+/3} & e^{\frac{2\pi i}{3}} \sqrt{2\gamma_-/3} \\ e^{-\frac{4\pi i}{3}} \sqrt{2\gamma_+/3} & e^{\frac{4\pi i}{3}} \sqrt{2\gamma_-/3} \end{array} \right\} \quad (\text{S4-4})$$

The equation (S4-4) can then be substituted into the temporal coupled-mode theory consisting of three resonator coupled with 3 ports. Where the amplitudes a_+ and a_- of the clockwise and counterclockwise modes of this acoustic trimer under angular-momentum biasing can be denoted as:

$$\frac{da_+}{dt} = (-iw_+ - \gamma_+)a_+ + \sqrt{\frac{2\gamma_+}{3}}S_1^+ + e^{-\frac{2\pi i}{3}}\sqrt{\frac{2\gamma_+}{3}}S_2^+ + e^{-\frac{4\pi i}{3}}\sqrt{\frac{2\gamma_+}{3}}S_3^+ \quad (\text{S4-5})$$

$$\frac{da_-}{dt} = (-iw_- - \gamma_-)a_- + \sqrt{\frac{2\gamma_-}{3}}S_1^+ + e^{\frac{2\pi i}{3}}\sqrt{\frac{2\gamma_-}{3}}S_2^+ + e^{\frac{4\pi i}{3}}\sqrt{\frac{2\gamma_-}{3}}S_3^+, \quad (\text{S4-6})$$

where S_1^+, S_2^+ and S_3^+ are the excitation signals at related ports. Here, S_1^+, S_2^+ and S_3^+ are signals from the input port, port 1 and port 2, respectively. The output signals S_1^-, S_2^- and S_3^- can be derived from the interferences of resonance-assisted coupling, coupling through a direct pathway of the incoming and outgoing waves. The related equations of output signals are shown as:

$$S_1^- = -S_1^+ + \sqrt{\frac{2\gamma_+}{3}}a_+ + \sqrt{\frac{2\gamma_-}{3}}a_- \quad (\text{S4-7})$$

$$S_2^- = -S_2^+ + e^{\frac{2\pi i}{3}}\sqrt{\frac{2\gamma_+}{3}}a_+ + e^{-\frac{2\pi i}{3}}\sqrt{\frac{2\gamma_-}{3}}a_- \quad (\text{S4-8})$$

$$S_3^- = -S_3^+ + e^{\frac{4\pi i}{3}}\sqrt{\frac{2\gamma_+}{3}}a_+ + e^{-\frac{4\pi i}{3}}\sqrt{\frac{2\gamma_-}{3}}a_- \quad (\text{S4-9})$$

Here, we assume the excitation is harmonic and only works input port for $S_1^+ = e^{-i\omega t}$, $S_2^+ = S_3^+ = 0$. For the variable change of amplitudes $\alpha_{\pm} = a_{\pm}e^{-i\omega t}$, we can achieve the following equations:

$$-i\omega a_+ = (-i\omega_+ - \gamma_+)a_+ + \sqrt{\frac{2\gamma_+}{3}} \quad (\text{S4-10})$$

$$-i\omega a_- = (-i\omega_- - \gamma_-)a_- + \sqrt{\frac{2\gamma_-}{3}} \quad (\text{S4-11})$$

Then we can achieve the solutions as:

$$\alpha_{\pm} = i\sqrt{\frac{2\gamma_{\pm}}{3}} / (\omega - \omega_{\pm} + i\gamma_{\pm}) \quad (\text{S4-12})$$

$$S_{11} = -1 + \sqrt{\frac{2\gamma_+}{3}}\alpha_+ + \sqrt{\frac{2\gamma_-}{3}}\alpha_- \quad (\text{S4-13})$$

$$S_{21} = e^{\frac{2\pi i}{3}}\sqrt{\frac{2\gamma_+}{3}}\alpha_+ + e^{-\frac{2\pi i}{3}}\sqrt{\frac{2\gamma_-}{3}}\alpha_- \quad (\text{S4-14})$$

$$S_{31} = e^{\frac{4\pi i}{3}}\sqrt{\frac{2\gamma_+}{3}}\alpha_+ + e^{-\frac{4\pi i}{3}}\sqrt{\frac{2\gamma_-}{3}}\alpha_- \quad (\text{S4-15})$$

where, γ_{\pm} denotes the inverse of related decay times to the Ports 0, 1 and 2, which are located at the azimuthal positions $\varphi = 0, 2\pi/3$ and $4\pi/3$, respectively. Due to symmetry, γ_+ and γ_- are usually equal, i.e. $\gamma_+ = \gamma_- = \gamma$. In order to achieve $T_{0 \rightarrow 1} = 1$ and $T_{0 \rightarrow 2} = 0$ at the frequency $\omega = \omega_0$ when the cavity modes are split, optimal topological performance can be achieved at $\omega_{\pm} = \omega_0 \pm \gamma/\sqrt{3}$. After considering the eigenfrequencies of the right and left-handed modes given by $\omega_{\pm} = \omega_0 \pm m c_{\text{eff}}/R_{\text{eff}}$, we can get the optimal analogous speed created by impedance modulation is $c_{\text{opt}} = \gamma R_{\text{eff}}/\sqrt{3}$. The integer number m is the azimuthal order. ω_0 is the resonance frequency and R_{eff} is the effective radius, where effective acoustic speed changes with air temperature in the form of $\sqrt{k' \cdot p/\rho}$, as k' is the ratio of specific heat. This trimer structure can be considered as three lumped elements, and the related impedance is $Z_i = \rho c = (\rho_0 + \rho_i)(c_0 + c_i)$. We can employ impedance translation theorem[188] or simulation result to get the effective impedance Z_{eff} and effective density ρ_{eff} , then $c_{\text{eff}} = \frac{Z_{\text{eff}}}{\rho_{\text{eff}}} - c_0$. Related design strategy can be based on that by considering the factors of the size,

geometry type and temperature distribution, etc. Then we can get the transmission coefficients at ports 1 and 2,

$$T_{0 \rightarrow 1} = \left| \frac{2}{3} \left(\frac{e^{-\frac{4\pi i}{3}}}{1 - \frac{i(w-w_-)}{\gamma_-}} + \frac{e^{-\frac{2\pi i}{3}}}{1 - \frac{i(w-w_+)}{\gamma_+}} \right) \right| \quad (\text{S4-16})$$

$$T_{0 \rightarrow 2} = \left| \frac{2}{3} \left(\frac{e^{-\frac{2\pi i}{3}}}{1 - \frac{i(w-w_-)}{\gamma_-}} + \frac{e^{-\frac{4\pi i}{3}}}{1 - \frac{i(w-w_+)}{\gamma_+}} \right) \right| \quad (\text{S4-17})$$

4.4.3. Topological protected edge mode and analysis

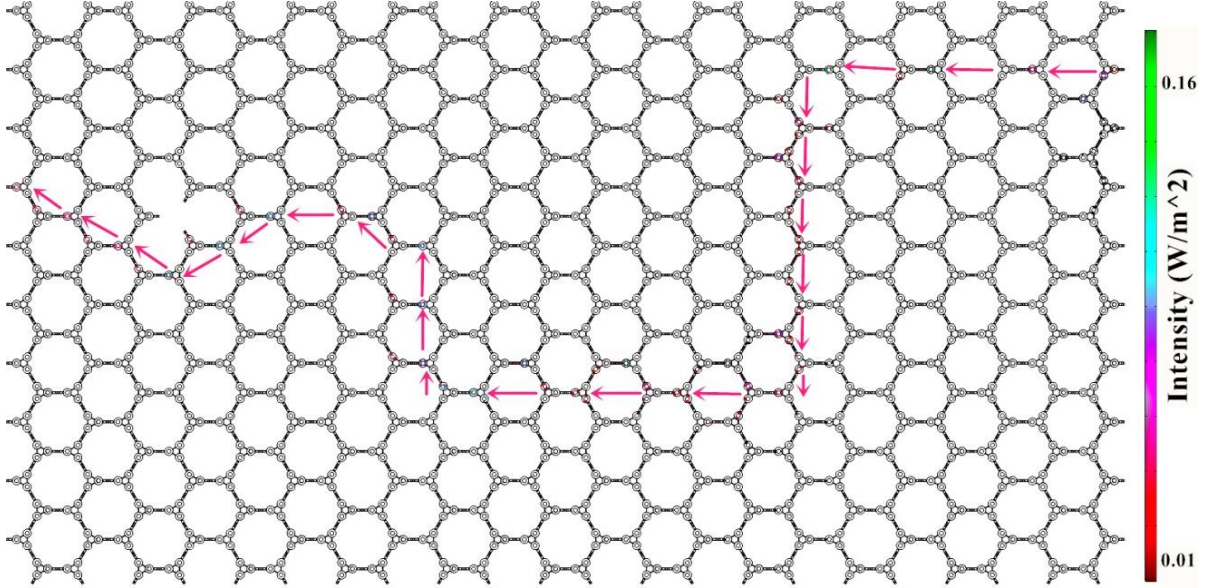


Figure S4-2| Topological protected acoustic edge mode. Excitation of a one-way edge mode and its propagation along an irregularly shaped domain wall.

As shown in Figure S4-2, the top structure consists of units without modulation, and the down structure consists of units with the modulation of Figure 4-3(c). It shows the possibility of creating dynamically reconfigurable and backscattering immune nonreciprocal waveguides in temperature modulation.

This designed geometry can be mapped onto a tight-binding Hamiltonian related to a hexagonal lattice with nearest-neighbour hopping, which is modified to consider the interconnected waveguides of the metamolecules

$$\hat{H} = \sum_m \hat{\epsilon}_m(Z) |\mathbf{m}\rangle \langle \mathbf{m}| + \sum_{m,n} \hat{J} |\mathbf{n}\rangle \langle \mathbf{m}| + \hat{J}^* |\mathbf{m}\rangle \langle \mathbf{n}|, \quad (\text{S4-18})$$

where $|m\rangle = |m_1, m_2, m_3\rangle$ is a vector whose three parts correspond to the three acoustic circulators consisting in each node of the hexagonal lattice. The impedance-independent hopping terms are defined by a diagonal 3×3 matrix $\hat{J}_m = \hat{J}\hat{I}$, while the on-site term can be defined as,

$$\hat{\epsilon}_m = \begin{pmatrix} w_0 + \delta w_1(Z) & k & k^* \\ k^* & w_0 + \delta w_2(Z) & k \\ k & k^* & w_0 + \delta w_3(Z) \end{pmatrix}, \quad (\text{S4-19})$$

where $\delta w_1(Z)$, $\delta w_2(Z)$, and $\delta w_3(Z)$ are the impedance modulation for each component. The related parameters introduced here are based on the form of the Hamiltonian: w_0 is the on-site energy (the lowest resonance frequency of acoustic circulators), and k is the on-site coupling between acoustic circulators of the same trimer.

Topological invariant of each acoustic band can be extracted by full-wave finite-element simulation in equations (S4-15 and S4-16), that is, Chern numbers, $C_n = \frac{1}{2\pi} \iint (\partial_{k_x} A_y - \partial_{k_y} A_x) d^2k$. Here, the numerically simulated eigenstates $|p_n\rangle$ of the effective Hamiltonian \hat{H}_{eff} and the Berry connection $A = -i\langle p_n | \partial_k | p_n \rangle$ are employed. The integration of Berry curvature over the entire Brillouin zone indicates the four interested bands yielding the Chern number $C_n = \{\pm 1, 0, 0, \mp 1\}$ for the right-handedness/left-handedness modulation in this trimer structure.

Chapter 5

5 Study of acoustic wave propagation in micro- and nanochannels

In order to investigate the topological acoustics in ultrasonic or in a micro- or nanostructure to realize miniaturization, an analytical model that can effectively clarify the acoustic transmission mechanism in micro- and nanochannels is necessary. Moreover, the acoustic wave propagating through porous nanomaterials like aerogels, MEMS devices, high-frequency acoustic transmission devices or near-vacuum systems, possesses relatively high Knudsen numbers, normally in the transition regime ($0.1 < Kn < 10$). In this regime, the characteristic length of micro- and nanochannels is comparable with the mean free path of monatomic gases, in which the classical continuum theory breaks down. In this paper, a theoretical model with the second-order slip boundary is proposed to describe acoustic wave propagation in micro- and nanochannels. The proposed theoretical model provides analytical solutions for the complex wavenumber, attenuation coefficient and other related transmission variables as function of a Knudsen number in the early transition regime ($0.1 < Kn < 1.0$), which are valuable for understanding acoustics at micro- and nanoscales. In addition, numerical simulations using the molecular-based DSMC method for dilute argon gas are carried out to validate the model and its analytical results. Findings suggest that such a model can effectively predict the acoustic behaviour in micro- and nanochannels. It is noted here, this Chapter is based on author's publication: Liu X, Cai X, Guo Q, et al. Study of acoustic wave propagation in micro-and nanochannels[J]. Wave Motion, 2018, 76: 51-60. And all the figures are used with the permission from ref. [128].

5.1 Introduction

Advancing the understanding of wave propagation through rarefied gases in porous nanomaterials, MEMS-like inertial sensors, resonant filters, and actuators[190, 191]-have been increasingly in demand. Continuum-based flow models have been often used to study the acoustic transmission issues analytically and numerically[188]. However, the extensive development of acoustical porous nanomaterials and miniaturization of MEMS devices at sub-atmospheric pressures, which cannot be modelled with sufficient accuracy by traditional

continuum theory, demand a more fundamental understanding of acoustics at micro- and nanoscales. In contrast, an analytical theory or model is always preferable and valuable for practical uses.

A theoretical model that is able to describe acoustic transmission in the transition regime can be applied to investigate sound propagation in micro- and nanostructures or in rarefied gas conditions, and therefore provide guidance in the design of nanomaterials and micro- or nanodevices. A detailed analysis of such phenomenon requires consideration of the rarefied effect, which is denoted by the Knudsen number as $Kn = \lambda/H$, where λ is the mean free path for a specific gas and H is the characteristic hydrodynamic length. Based on the Knudsen number, gas flow can be classified into three major flow regimes: the continuum regime ($Kn < 0.1$), where the flow field can be described accurately by classical continuum theories; the transition regime ($0.1 < Kn < 10$), where continuum-theory-based descriptions fail because the ratio of gas-structure collisions to intermolecular collisions becomes significant; and the free-molecular regime ($Kn > 10$), where there are nearly no collisions among the molecules[192].

Many MEMS devices and nanomaterials like aerogels fall in the early transition regime. The increasing popularity of nanomaterials and applications of MEMS devices demand more investigations of acoustics in the transition regime. Furthermore, these investigations can be applied to cases where either characteristic time or length scale is assumed to be smaller than that of the collision period or the mean free path of a specific gas, respectively. Such conditions can be found in the high-frequency acoustic transmission or near-vacuum systems[193]. Recently, realizations of negative effective density and slower effective acoustic speed of some acoustic metamaterials and lightweight sound absorbing materials like aerogel[139] also demand full investigation of acoustic transmission in the transition regime. In the area of topological acoustics[33], when the characteristic hydrodynamic length approaches the nanoscale, the related analytical theory of acoustics is also very important. Even for classical resonance structures, the analysis of acoustic mass, resistance and compliance may show some differences at the micro- and nanoscales. These potential applications indicate the importance of the study of acoustic wave propagation in the transition regime.

The pioneering theoretical and experimental research for acoustic wave propagation in the non-continuum regime was done by Greenspan[194] and Meyer et al.[195] in the 1950s, and has since attracted many researchers to study related issues. Initially, theoretical works were focused on acoustic propagation in infinite or semi-infinite geometries, where one moving boundary works as an acoustic source[193, 196, 197], and specific propagation properties like damping effects, wave speed and wavenumber in different external conditions (temperature, gases type and humidity) were studied. Afterwards, different geometrical cross-sections and gas-structure interaction models were proposed to investigate acoustic wave propagation in the transition regime analytically and numerically[95, 96]. Later, contributions were made on a confined configuration, setting one stationary boundary as a “resting receiver” to study the effects of acoustic wave reflection and other related transmission issues[198-200]. The majority of studies in this area have assumed linearized small-amplitude acoustic wave solutions, while few have examined nonlinear large-amplitude issues[201].

To investigate wave propagation in small confined geometries with specific boundary conditions, Hadjiconstantinou[91] in 2003 developed a model with the first-order slip boundary condition and provided an analytical solution for acoustic wave propagation in micro- and nanochannels, which was an extension of Lamb’s continuum treatment[92, 93]. In 2005, considering the effects of the Knudsen layer and using the second-order velocity boundary condition, Hadjiconstantinou[94] solved the oscillatory shear-driven Couette flow problem using the Navier-Stokes approximation and achieved good agreement with DSMC results up to $Kn \approx 0.4$. Kozlov et al.[95] investigated acoustical properties in pores of simple geometries with the first-order approximation and validated their results with experimental data of dynamic density at low frequencies. Umnova et al.[96] developed an analytical model to describe acoustic propagation in microfibrinous materials while accounting for the slip boundary effect, where the homogenous method used was also verified by finite element method (FEM) simulation. In terms of numerical investigation, various simulation methods have been proposed, such as the linearized Boltzmann method[97-99], Lattice Boltzmann method[100-102], Bhatnagar–Gross–Krook (BGK) model[103, 104], molecular dynamics (MD) model[105-107], and DSMC[80, 108]. Based on our literature survey, the DSMC method, initially proposed by G. A. Bird[80], is the most widely used tool for the simulation

of acoustic wave propagation at the micro- and nanoscales and is renowned for its accuracy and time efficiency. Derivative DSMC methods, such as Wang and Xu's unified gas-kinetic scheme DSMC (UGKS-DSMC)[109], Fan and Shen's information preserving DSMC (IP-DSMC)[110], Mohssen and Hadjiconstantinou's Low-Variance Deviational Simulation Monte Carlo (LVDSMC)[111], were proposed to improve the performance of the traditional DSMC method. All these works mentioned above can only extend the traditional continuum theory up to $Kn \approx 0.4$ or even smaller for the acoustic wave propagation in micro- and nanochannels, so there is still a need to develop an analytical solution suitable for higher Knudsen numbers.

In this paper, we investigate acoustic wave propagation in micro- and nanochannels that fall in the transition regime. Specifically, an accurate and easy-to-use theoretical model and associated analytical solutions is developed using the second-order velocity and temperature slip boundary conditions, and verified by DSMC simulations. Based on the modified acoustic slip surface definition of the second-order slip boundary condition in gas flow, we develop a theoretical and analytical model that is able to provide a detailed description of acoustic wave propagation at relatively high Kn numbers, up to 1.0. Based on this model, we can extract properties such as the acoustic propagation constant, complex effective density, effective acoustic speed and characteristic impedance. A DSMC program based on Bird's DS2V simulation tool is developed to validate our analytical results in the transition regime.

5.2 Theory for acoustic wave propagation in narrow channels

The basic wave propagation theory in narrow channels is derived from Hadjiconstantinou's method[91], and some data setups are based on Hadjiconstantinou and Garcia's paper[202]. Specifically, the long-wavelength approximation is used to assume that the axial component of the viscous term is negligible, and the pressure is assumed to be uniform in the cross-section such that the velocity and temperature interaction fields are decoupled. Also, the Maxwell diffusive model is used to model the gas-structure interactions in a two-dimensional long smooth channel, where the channel length L is much longer than the height H (see Figure 5-1).

Based on the acoustic property of fluctuation, the gas velocity, pressure, density, temperature fields is defined respectively as

$$u(x, y, t) = \tilde{u}(x, y) \exp(i\omega t), \quad (5-1a)$$

$$P(x, t) = \tilde{P}(x) \exp(i\omega t) + P_0, \quad (5-1b)$$

$$\rho(x, y, t) = \tilde{\rho}(x, y) \exp(i\omega t) + \rho_0, \quad (5-1c)$$

$$T(x, y, t) = \tilde{T}(x, y) \exp(i\omega t) + T_0, \quad (5-1d)$$

where P_0, ρ_0, T_0 are the equilibrium values of pressure, density and temperature for gas flow in the channel, respectively. $\tilde{u}(x, y), \tilde{P}(x), \tilde{\rho}(x, y), \tilde{T}(x, y)$ are defined as the fluctuation amplitudes of velocity, pressure, density and temperature, respectively.

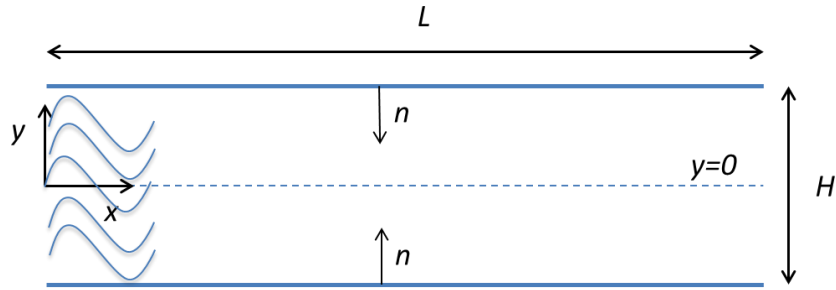


Figure 5-1. Narrow channel geometry for acoustic wave propagation from the left to right side, exhibiting fully diffuse reflection on the upper and lower walls.

As stated in Lamb's approach[92], these narrow micro- and nanochannels can be assumed to be a quasi-static and isothermal system. Thus, as demonstrated by Hadjiconstantinou[91], the propagation characteristics can be determined by substituting the pressure gradient with the gas average particle displacement ξ , as shown below:

$$\tilde{u}_b = -\frac{1}{R} \frac{d\tilde{P}}{dx}, \quad (5-2a)$$

$$\frac{dP}{dx} = -\left(\frac{\partial P}{\partial \rho}\right)_{av} \rho_0 \frac{\partial^2 \xi}{\partial x^2}, \quad (5-2b)$$

where R is defined as the flow resistance and \tilde{u}_b is the gas bulk velocity in the cross-section of the narrow channel. $(\partial P/\partial \rho)_{av}$ denotes that this derivative is an average value. Moreover, assuming negligible edge effect in a long narrow channel undergoing the isothermal propagation process, the related equations for the steady state can be derived, as shown below:

$$i\omega\xi = \frac{\rho_0(\partial P/\partial \rho)_T}{R} \frac{\partial^2 \xi}{\partial x^2}, \quad (5-3)$$

$$\beta^2 \equiv (m + ik)^2 = \frac{i\omega R}{P_0}, \quad (5-4)$$

where β ($u_b \propto \exp(-\beta x)$) is defined as the complex propagation constant, $k = 2\pi/l$ is the complex wavenumber, m is the attenuation coefficient and l is the complex wavelength.

When an acoustic wave transmits through a narrow channel, the fluid inertia and heat conduction will affect the transmission equations. The long-wavelength approximation issue is corrected for by solving the linearized momentum and energy equations. The linearized momentum equation transformed by amplitude \tilde{u} and \tilde{P} is

$$\frac{\partial^2 \tilde{u}}{\partial y^2} + \phi^2 \tilde{u} = \frac{1}{\mu} \frac{d\tilde{P}}{dx}, \quad (5-5)$$

where $\phi^2 = -i\rho_0\omega/\mu$. Based on the discussion in Stinson et al.[93], the assumption of a constant pressure field in the cross-section of the channel and negligible axial component of the viscous term requires $|\phi^2| \gg |\beta^2|$ and $|\beta H| \ll 1$.

The linearized energy equation transformed by amplitudes \tilde{T} and \tilde{P} is

$$\frac{\partial^2 \tilde{T}}{\partial y^2} + \psi^2 \tilde{T} = \psi^2 \frac{(\gamma-1)T_0}{\gamma P_0} \tilde{P}, \quad (5-6)$$

where $\psi^2 = -\frac{i\rho_0 c_p}{\kappa} = \phi^2 Pr$, κ is the thermal conductivity, c_p is the specific heat in constant pressure, Pr is the Prandtl number and γ is the ratio of specific heats.

5.3 The complete solutions based on slip boundary conditions

The solutions of Boltzmann equations by Cercignani[203] and Hadjiconstantinou[91] proved that, for $Kn < 0.1$, the accurate hydrodynamic fields of bulk flow properties can be achieved with the continuum description of specific slip boundary conditions. Due to the existence of the Knudsen layer near the boundary wall in the transition regime, whose thickness is normally 1.5λ , the continuum description will not be accurate[204]. Consequently, some modifications must be made to extend the continuum theories for a convenient calculation of acoustic propagation in a narrow channel. Hadjiconstantinou[91] used the first-order slip boundary condition to make the analytical calculation effective around $Kn = 0.1$. Here, we use second-order slip boundary conditions to extend the analytical calculations of acoustic propagation to the transition regime. For engineering applications, the momentum accommodation coefficient is set to be unity, so that the general form yields

$$u - U_{wall} = C_1\lambda \left(\frac{\partial u}{\partial n}\right)_{wall} - C_2\lambda^2 \left(\frac{\partial^2 u}{\partial n^2}\right)_{wall}, \quad (5-7)$$

$$T - T_{wall} = C_3\lambda \left(\frac{\partial T}{\partial n}\right)_{wall} + C_4\lambda^2 \left(\frac{\partial^2 T}{\partial n^2}\right)_{wall}, \quad (5-8)$$

where C_1, C_2, C_3 and C_4 represent slip coefficients, U_{wall} and T_{wall} are the wall velocity and temperature, respectively. Based on the condition of symmetric channel and velocity slip boundary conditions at walls, the solution of the momentum equation in acoustic propagation is

$$\tilde{u} = \frac{1}{\mu\phi^2} \frac{d\bar{P}}{dx} \left(1 + \frac{\cos\phi y}{C_1\lambda\phi\sin\frac{\phi H}{2} + C_2\lambda^2\phi^2\cos\frac{\phi H}{2} - \cos\frac{\phi H}{2}} \right), \quad (5-9)$$

and thus the bulk velocity is

$$\tilde{u}_b = \frac{1}{H} \int_{-\frac{H}{2}}^{\frac{H}{2}} \tilde{u} dy = \frac{1}{\mu\phi^2} \frac{d\bar{P}}{dx} \left(1 + \frac{2}{H\phi} \frac{1}{C_1\lambda\phi + C_2\lambda^2\phi^2\cot\frac{\phi H}{2} - \cot\frac{\phi H}{2}} \right) = -\frac{1}{R} \frac{d\bar{P}}{dx}. \quad (5-10)$$

Similarly, based on the condition of symmetric channel and temperature jump boundary conditions at the walls, the solution of the energy equation in acoustic propagation is

$$\tilde{T}(x, y) = \frac{(\gamma-1)}{\gamma} \tilde{P} \frac{T_0}{P_0} \left(1 + \frac{\cos\psi y}{C_3 \lambda \psi \sin \frac{\psi H}{2} - C_4 \lambda^2 \psi^2 \cos \frac{\psi H}{2} - \cos \frac{\psi H}{2}} \right), \quad (5-11)$$

and the average temperature for every cross-section in the channel is

$$\tilde{T}_{av}(x) = \frac{1}{H} \int_{-\frac{H}{2}}^{\frac{H}{2}} \tilde{T} dy = \frac{(\gamma-1)}{\gamma} \tilde{P} \frac{T_0}{P_0} \left(1 + \frac{2}{\psi H} \frac{1}{C_3 \lambda \psi - C_4 \lambda^2 \psi^2 \cot \frac{\psi H}{2} - \cot \frac{\psi H}{2}} \right). \quad (5-12)$$

During no-slip isothermal flow, following Lamb's analysis, we have $|\psi H/2| \sim |\phi H/2| \rightarrow 0$, $\frac{\rho_0}{P_0} (\partial P / \partial \rho)_{av} \rightarrow 1$ ($\tilde{T} \rightarrow 0$). Assuming an ideal gas, based on the equation of state and the fact that $\tilde{P}_{av} = \tilde{P}$, we find

$$\frac{\rho_0}{P_0} \left(\frac{\partial P}{\partial \rho} \right)_{av} = \frac{1}{1 - \frac{P_0}{T_0} \left(\frac{\partial \tilde{T}}{\partial \tilde{P}} \right)_{av}} = \frac{1}{1 - \frac{(\gamma-1)}{\gamma} \left(1 + \frac{2}{\psi H} \frac{1}{C_3 \lambda \psi - C_4 \lambda^2 \psi^2 \cot \frac{\psi H}{2} - \cot \frac{\psi H}{2}} \right)}. \quad (5-13)$$

Finally, the complete solution for propagation constant in this narrow channel is

$$\beta^2 \equiv (m + ik)^2 = \frac{i\omega R}{\rho_0 \left(\frac{\partial P}{\partial \rho} \right)_{av}} = - \frac{i\omega \mu \phi^2 \left[1 - \frac{(\gamma-1)}{\gamma} \left(1 + \frac{2}{\psi H} \frac{1}{C_3 \lambda \psi - C_4 \lambda^2 \psi^2 \cot \frac{\psi H}{2} - \cot \frac{\psi H}{2}} \right) \right]}{P_0 \left(1 + \frac{2}{H\phi} \frac{1}{C_1 \lambda \phi + C_2 \lambda^2 \phi^2 \cot \frac{\phi H}{2} - \cot \frac{\phi H}{2}} \right)} \quad (5-14)$$

where the viscosity based mean free path $\lambda = 4\bar{c}\mu/(5P_0)$, in which $\bar{c} = \sqrt{8k_b T/(\pi m_m)}$ is defined as the average gas molecular speed, m_m is the molecular mass, k_b is the Boltzmann constant and μ is the gas dynamic viscosity.

Although very few investigations have focused on acoustic wave transmission at the micro- and nanoscales, there have been many studies conducted in the area of gas flow at narrow channels. Our study has been informed by previous studies listed in Table 5-2, which shows different slip coefficients deriving from past research on gas flow.

Radtke and Hadjiconstantinou[205] used the LVDSMC method based on the BGK model and HS model to consider the corresponding constant volumetric heating implementation,

which makes the second-order velocity and temperature slip boundary conditions effective in the transition regime. Hadjiconstantinou[91] applied the solution of the linearized Boltzmann equation by Sone, Ohwada & Aoki[206] to obtain the first-order slip coefficients of acoustic propagation in a narrow channel. Li et al.[207] combined the effective relaxation time in the lattice Boltzmann model with Bosanquet-type effective viscosity to achieve an accurate slip boundary condition. Aubert and Colin[208] showed a strong correlation between experimental results and the predictions from the first-order slip boundary condition, and used the reflection coefficient and corresponding mass flow rate to calculate the second-order slip coefficients. Wu[209] derived an improved second-order slip model from kinetic theory, which was also verified by the numerical result of the linearized Boltzmann equation. For all of above studies, the related experimental results were consistent with the analytical predictions.

Table 5-2. Values of different slip coefficients

References	C_1	C_2	C_3	C_4	Remark
Radtke and Hadjiconstantinou	1.11	0.61	1.1545	-1.1	BGK model, LVDSMC, volumetric heating
Radtke and Hadjiconstantinou	1.11	0.61	2.127	-2.4347	HS model, LVDSMC, volumetric heating
Hadjiconstantinou	1.1	0	2.0681	0	LBE
Li et al.	1.0	0.8	0	0	LB model
Aubert and Colin	1.0	1.125	0	0	N-S equation
Wu	1.333	0.25	0	0	Kinetic-based theory
Hadjiconstantinou	0	0	0	0	No-slip boundary condition

5.4 DSMC for the verification of acoustic wave propagation in a narrow channel

DSMC method uses simulation molecules to represent a large amount of real molecules based on probabilistic simulation to solve Boltzmann equation for finite Knudsen number gas flows. Specially, molecule-surface collisions are calculated through probabilistic and phenomenological methods. In this simulation process, molecules are moved and collided in a realistic manner which could be directly coupled to physical space and time such that all the unsteady flow characteristics can be simulated. As is shown by Wagner[210], at the limit of infinitesimal discretization and huge amount of numerical particles, the DSMC solution is consistent with the solution of the Boltzmann equation, provided that the time step is sufficiently small and enough ensemble samples are taken. Furthermore, the Chapman-Enskog expansion theory[211, 212] can provide a solution for the Boltzmann equation in the continuum form of the conservation theory. A detailed description of DSMC is provided by Bird[80], which includes all the gas-structure interaction models, gas collision models and sampling techniques.

In this paper, the simulation of acoustic wave propagation in a narrow channel is based on the codes distributed by Bird's research group. Using the DSMC program, the monatomic gaseous argon (hard-sphere diameter is $\sigma = 3.66 \times 10^{-10} m$ and molecular mass is $m_m = 6.63352 \times 10^{-26} kg$) is modelled in a two-dimensional channel with fully accommodating Maxwell gas-structure interactions based on the variable hard sphere (VHS) collision model. The gas pressure and temperature are set as $P = 1.013 \times 10^5 Pa$ and $T = 273.15 K$, respectively. The mean free path is calculated as $\lambda = 6.31 \times 10^{-8} m$.

The wave amplitude should be small enough to avoid nonlinear effects[202]. Especially in the case that the velocity amplitude $v \ll c/R''$, $R'' = c^2\rho/w\mu$, where R'' is defined as the acoustic Reynolds number, ρ is the gas density, μ is the viscosity and c is acoustic speed, the viscous term can dominate the nonlinear term. At the high frequency range, the attenuation coefficient can be fairly high, such that the simulation domain does not need to be large to be effective, which serves to reduce computation time. In this paper, the simulated angular frequency is set to $6 \times 10^8 rad/s$, which corresponds to $4 < R'' < 20$, and thus the

reasonable velocity amplitude should be around $v_0 \approx 0.025c$ to avoid nonlinear effects. Correspondingly, the velocity is set to 10 m/s.

For the setup of program design, the oscillatory piston boundary wall is activated during half of the period as a sound source at $x = 0$. During this unsteady flow, the time average calculation in steady flow is replaced by the ensemble average at every time step. To minimize the error produced by sampling, five cells per mean free path, five steps per collision time and two steps per transit time are chosen. Also, the nearest neighbour collision model is used to achieve required accuracy with fewer simulated particles. To ensure that each distributed cell size is less than 0.1λ and the mean number of particles per cell exceeds 100 in order to obtain satisfactory accuracy[202], the numerical time step in this unsteady simulation should be significantly small, that is, $\Delta t \ll \lambda/\sqrt{2k_bT/m_m}$. Moreover, when it comes to the fluctuation issue, in order to guarantee enough acoustic resolution, the time step chosen should also satisfy $\Delta t \ll 2\pi/\omega$. Here, we set $\Delta t = 0.1\lambda/\sqrt{2k_bT/m_m}$, such that the largest Δt is $1.8713 \times 10^{-11} s$, which is much smaller than $2\pi/\omega \approx 1.0472 \times 10^{-8} s$. Seven cases for $Kn = 0.1, 0.2, 0.4, 0.5, 0.7, 0.8, 1.0$ are simulated and compared with the analytical results from Eq. (5-14) based on the attenuation coefficient, which defines the performance of acoustic energy dissipation in this channel as shown in Figure 5-2.

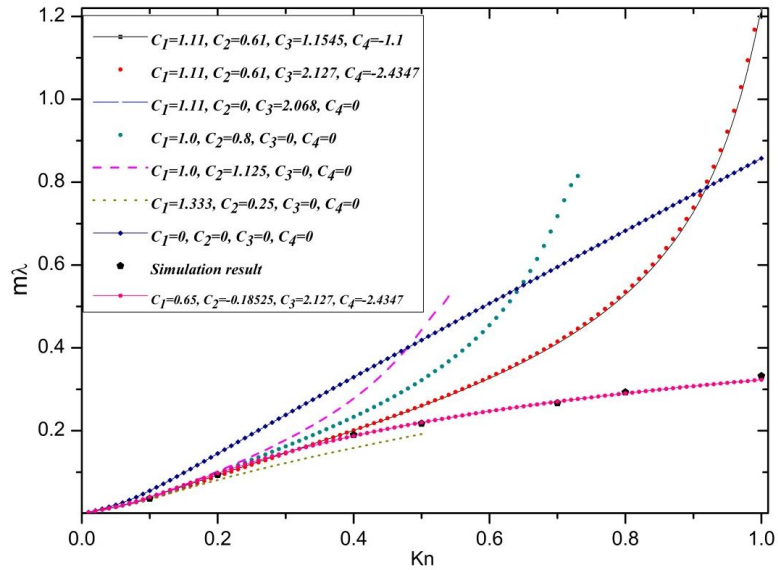


Figure 5-2. Comparison between the simulation result and the analytical predictions of different slip models on attenuation coefficient for $w = 6 \times 10^8 \text{ rad/s}$.

As shown in Figure 5-2, all the above models show strong similarity to each other when $Kn < 0.1$. Beyond that range, for $0.1 < Kn < 1.0$, Hadjiconstantinou's first-order slip model and Wu's kinetic-based model show a relative better approximation than other models compared to the simulation results. Two standard second-order models of rarefied gas flow based on BGK model and HS model provided by Radtke and Hadjiconstantinou have shown relative big difference compared to our simulation result, although BGK model shows a similar trend for the attenuation coefficient. Here we propose a new second-order slip model based on the fact of the oscillatory property for acoustic wave propagation in micro- and nanochannels, especially near the walls. The oscillatory wave will raise the slip velocity, and also lead to a high shear rate, which means that the velocity distribution of a slip layer using the classical second-order velocity slip boundary condition proposed by Karniadakis and Beskok[213] is not suitable. Zhang et al.[214] proposed an adjustment second-order velocity slip model, which is in the form of

$$u_s - U_{wall} = \frac{1-(1-C)\sigma_v}{\sigma_v} \left[\lambda \left(\frac{\partial u}{\partial n} \right)_{wall} + \frac{(1-C)}{2} \lambda^2 \left(\frac{\partial^2 u}{\partial n^2} \right)_{wall} \right]. \quad (5-15)$$

Eq. (5-15) comes from the idea that the contribution of the slip velocity between the Knudsen layer and wall surface should be inversely proportional to the distance of the slip layer from the Knudsen layer versus the distance of the slip layer from the wall surface. σ_v is defined as the tangential momentum accommodation coefficient (TMAC). The coefficient $C = \xi_s/\lambda$ ($C \in [0,1]$), in which ξ_s represents the distance between the slip surface and the wall, is comparable to the mean free path, which should not be neglected.

Here, we import an acoustic perturbation coefficient A , which will reduce the contribution of agglomeration near the wall surface. Based on this fact, the value of A should be larger than 1, so the related particle number density is

$$n_\lambda = ACn_s, \quad n_w = (1 - AC)n_s, \quad (5-16)$$

where n_λ represents particles from the Knudsen layer, n_w represents particles from the wall surface, and n_s denotes particles in the slip surface.

According to the tangential momentum conservation in the slip surface, there are

$$u_s = [AC + (1 - AC)(1 - \sigma_v)]u_\lambda + (1 - AC)\sigma_v u_w, \quad (5-17)$$

after u_λ is expanded by Taylor series of u_s , combining Eq. (5-17) with the related result, we can get the final new second-order slip model, which considers the effect of acoustic perturbation

$$u_s - U_{wall} = \frac{1-(1-AC)\sigma_v}{\sigma_v} \left[\lambda \left(\frac{\partial u}{\partial n} \right)_{wall} + \frac{(1-AC)}{2} \lambda^2 \left(\frac{\partial^2 u}{\partial n^2} \right)_{wall} \right]. \quad (5-18)$$

According to Zhang's and Bao's[215] simulation results, the value of C varies with Knudsen number, so we use an average value of C=0.43. Finger[216] had defined the TMAC as being in the range of 0.85-1.06. Here, we will set $\sigma_v = 1.0$ to satisfy common engineering applications. The simulation of acoustic transmission by Denize Kalempa[217] at the frequency around $6 \times 10^8 \text{ rad/s}$ shows less particle condensation distribution along the wall surface, which confirms that we can set A=1.51163. Based on Eq. (5-18), the velocity slip coefficients of C_1 and C_2 are equal to 0.65 and -0.18525, respectively, and the temperature slip coefficients remain the same values as the HS model of Radtke and Hadjiconstantinou[205]. With this second-order slip model, the analytical result of the new model agrees well with the simulation result. Moreover, it also agrees well with the solution of Boltzmann equation from Cercignani[203] based on the concept of the proportionality coefficient.

5.5 Properties of the new second-order slip model

For practical applications, it is important to express this new second-order slip model in terms of parameters related to acoustic transmission. Some parameters such as complex effective density, effective damping coefficient, effective acoustic speed and characteristic impedance are investigated in comparison with the related parameters of the no-slip model and Hadjiconstantinou's first-order model[91], which reveals some transmission differences at the micro- and nanoscales.

Eq. (5-10) can be rewritten in the form of complex effective density and effective damping coefficient[188]

$$\tilde{u}_b = \frac{d\tilde{P}}{dx} (i\omega\rho + R') = -\frac{1}{R} \frac{d\tilde{P}}{dx}, \quad (5-19)$$

and thus the complex effective density can be denoted as

$$\rho = Im \left[\frac{1}{w\mu\phi^2} \left(1 + \frac{2}{H\phi} \frac{1}{C_1\lambda\phi + C_2\lambda^2\phi^2 \cot\frac{\phi H}{2} - \cot\frac{\phi H}{2}} \right) \right], \quad (5-20)$$

and the effective damping coefficient can be denoted as

$$R' = Re \left[\frac{1}{\mu\phi^2} \left(1 + \frac{2}{H\phi} \frac{1}{C_1\lambda\phi + C_2\lambda^2\phi^2 \cot\frac{\phi H}{2} - \cot\frac{\phi H}{2}} \right) \right]. \quad (5-21)$$

From Eq. (5-14), the effective acoustic speed is defined as $c = w/k$, where k is the complex wavenumber. Thus c can be defined as

$$c = \frac{w}{Im \left\{ \frac{iw\mu\phi^2 \left[1 - \frac{(\gamma-1)}{\gamma} \left(1 + \frac{2}{\psi H} \frac{1}{C_3\lambda\psi - C_4\lambda^2\psi^2 \cot\frac{\psi H}{2} - \cot\frac{\psi H}{2}} \right) \right]}{P_0 \left(1 + \frac{2}{H\phi} \frac{1}{C_1\lambda\phi + C_2\lambda^2\phi^2 \cot\frac{\phi H}{2} - \cot\frac{\phi H}{2}} \right)} \right\}}, \quad (5-22)$$

and the characteristic impedance can be defined as $Z = \rho c$, so Z can be written as

$$Z = w * \frac{Im \left[\frac{1}{w\mu\phi^2} \left(1 + \frac{2}{H\phi} \frac{1}{C_1\lambda\phi + C_2\lambda^2\phi^2 \cot\frac{\phi H}{2} - \cot\frac{\phi H}{2}} \right) \right]}{Im \left\{ \frac{iw\mu\phi^2 \left[1 - \frac{(\gamma-1)}{\gamma} \left(1 + \frac{2}{\psi H} \frac{1}{C_3\lambda\psi - C_4\lambda^2\psi^2 \cot\frac{\psi H}{2} - \cot\frac{\psi H}{2}} \right) \right]}{P_0 \left(1 + \frac{2}{H\phi} \frac{1}{C_1\lambda\phi + C_2\lambda^2\phi^2 \cot\frac{\phi H}{2} - \cot\frac{\phi H}{2}} \right)} \right\}}, \quad (5-23)$$

Figure 5-3 shows a comparison of the new second-order slip model, no-slip model and first-order slip model concerning the relative complex effective density as a function of Knudsen number. The no-slip model achieves a larger complex effective density compared to the slip models throughout the calculated Knudsen number range, due to more particle condensation near the wall surface. Moreover, at around $Kn = 0.07$, there is a peak for both slip models. For the new second-order slip model, the effective density is slightly less than the static density when $Kn > 0.28$, which may be due to a change in slip velocity that is large enough to offset the particle condensation effect in this narrow channel. However, for the no-slip model, the complex effective density stabilizes at a higher Knudsen number and is always larger than the static density.

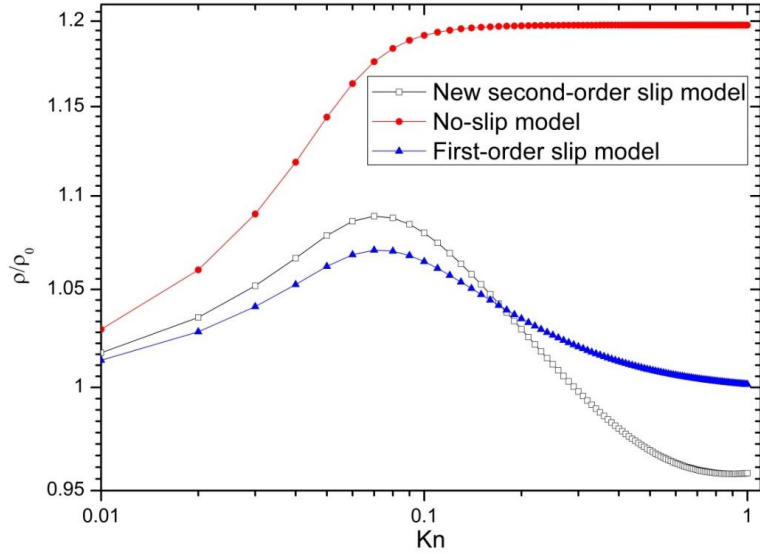


Figure 5-3. Comparison of the new second-order slip model, no-slip model and first-order slip model for the relative complex effective density.

Figure 5-4 shows a comparison of the new second-order slip model, no-slip model and first-order slip model concerning the effective damping coefficient, which represents the performance of acoustic resistance along the channel, as a function of Knudsen number. In this figure, due to the higher energy dissipation, the no-slip model achieves a higher effective damping coefficient compared to the slip models throughout the calculated Knudsen number range and this deviation from the slip models increases as the Knudsen number increases. The new second-order slip model shows similar result compared to the first-order slip model.

Figure 5-5 shows a comparison of the new second-order slip model, no-slip model and first-order slip model concerning the relative effective acoustic speed as a function of Knudsen number. The existence of slip velocity decreases the effective density, and thus both slip models achieve a higher effective acoustic speed than the no-slip model throughout the calculated Knudsen number range and their deviation from the no-slip model increases as the Knudsen number increases. Also, the effective acoustic speed is consistently less than the normal acoustic speed in infinite space.

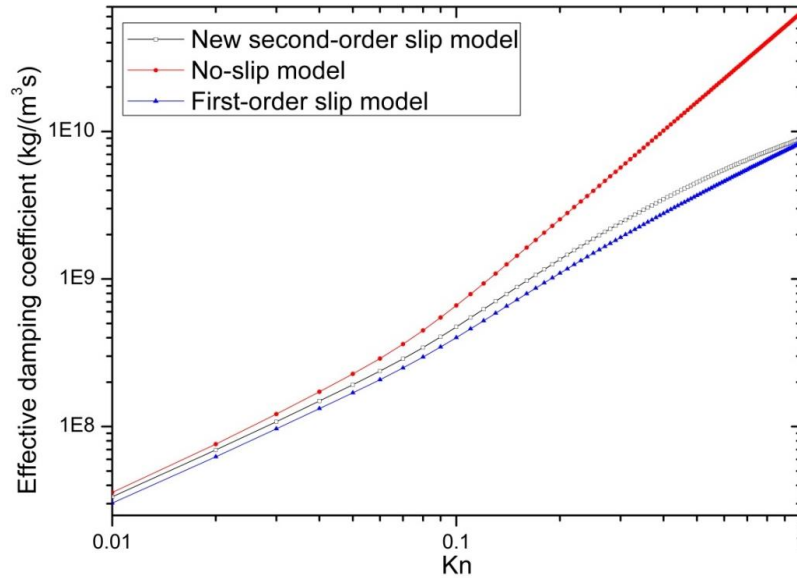


Figure 5-4. Comparison of the new second-order slip model, no-slip model and first-order slip model for the effective damping coefficient R' .

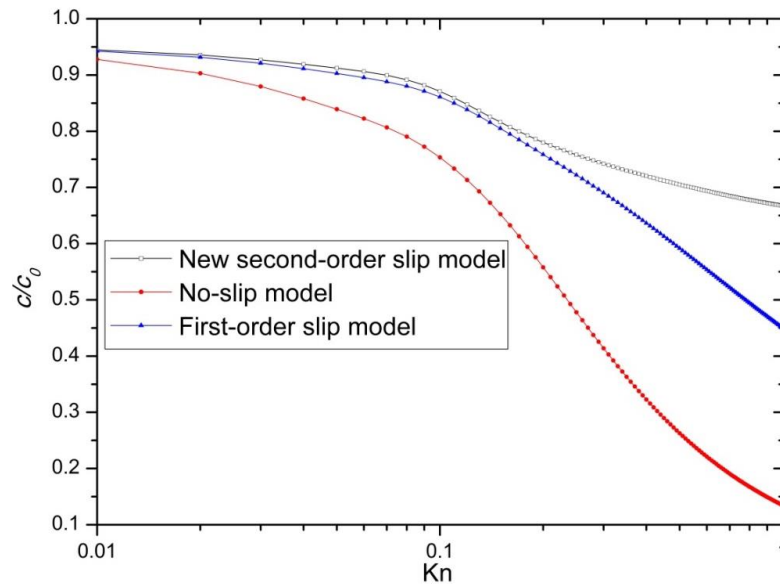


Figure 5-5. Comparison of the new second-order slip model, no-slip model and first-order slip model for the relative effective acoustic speed.

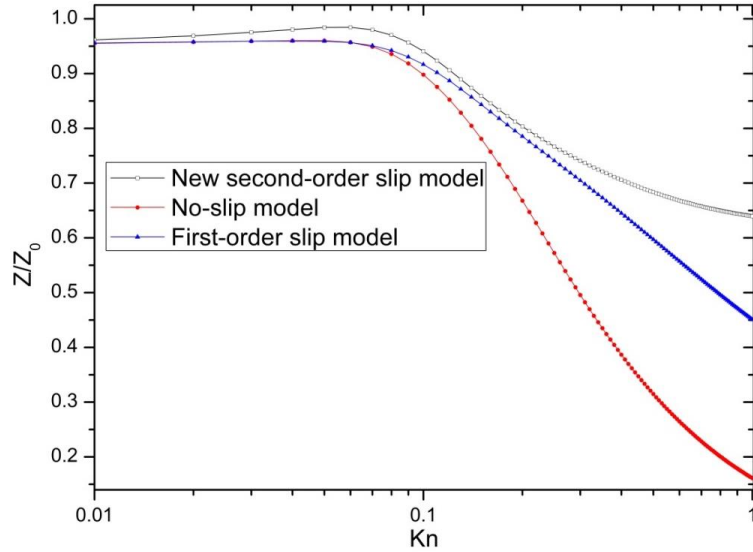


Figure 5-6. Comparison of the new second-order slip model, no-slip model and first-order slip model for the relative characteristic impedance.

Figure 5-6 shows a comparison of the new second-order slip model, no-slip model and first-order slip model concerning the relative characteristic impedance as a function of Knudsen number. Both slip models achieve higher characteristic impedance than the no-slip model throughout the calculated Knudsen number range and their deviation from the no-slip model increases as the Knudsen number increases. Also, the characteristic impedance is consistently less than the normal one in infinite space. Moreover, at around $Kn=0.07$, there is a peak for the new second-order slip model. This figure also indicates that the difference in the characteristic impedance for nanoporous structure and infinite space is negligible at relative low Knudsen numbers, which can lead to reconsideration in the design of some acoustic absorption structures.

5.6 Conclusions

In this paper, we develop a new model based on the second-order velocity and temperature slip boundary conditions and obtain an analytical solution for acoustic wave propagation in micro- and nanochannels, which is validated by DSMC simulation results. This theoretical model, which extends to the non-continuum regime, remains robust and reasonably accurate up to $Kn \approx 1.0$. Thus, with a high angular frequency of $\omega = 6 \times 10^8 \text{ rad/s}$, the acoustical properties of argon gas in the range of $0.1 < Kn < 1.0$ can be solved by our analytical method,

covering a wider range of Knudsen numbers as compared to Hadjiconstantinou's first-order slip model[91]. For different frequencies, as shown in related simulation results, the slip surface coefficient C keeps constant in different frequencies, while the acoustic perturbation coefficient A can be smaller as the frequency goes higher. When comes to a relative lower frequency range, the coefficients C and A are almost invariable. So it would be easy and convenient to achieve related slip coefficients for the dependency of frequencies. These kinds of models are highly desirable because they allow the analytical study of acoustic wave propagation in micro- and nanoscales, which is more efficient and convenient than molecular-based numerical simulation methods. Results corresponding to different slip models have been compared to the simulation results and show different attenuation properties as the Knudsen number changes. Highly practical and useful parameters such as complex effective density, effective damping coefficient, effective acoustic speed and characteristic impedance are investigated in comparison to their counterparts in the no-slip model and first-order slip model.

The newly developed model and the analytical solutions obtained from it show great potential in advancing our fundamental understanding of acoustics in porous nanomaterials such as aerogel, MEMS devices, metamaterial and small resonance structures. This can in turn improve the design of such acoustical nanomaterials and devices. Even for more complex topological acoustics, which often require full investigation of acoustic diffraction, scattering, resonance, etc., the newly developed model can provide very useful information and guidance.

6 Conclusion and Future Work

6.1 Conclusion

The discovery of topological acoustics advances the potential development of noise attenuation, ultrasonic imaging, sound manipulation, and information delivering, etc. Tremendous efforts have been made to develop practical topological acoustic devices or systems. In recent years, ideas and methodologies from condensed-matter physics, such as the QHE, the QSHE, and the QVHE, combined with the configurations of sonic crystals and metamaterials, have been utilized and thoroughly investigated to achieve topologically protected acoustic transmission. However, many of these studies are still in their infancy and mostly rely on bulky, noisy, overly complicated, untunable and narrow-band-effective facilities, which severely block the development of practical acoustic applications. It is therefore highly desirable but challenging to design more practical topological acoustic devices or systems, including backscattering immune, tunable, broadband and miniaturized topological acoustic properties. My PhD work has focused on developing novel modulation mechanisms, versatile configurable lattice structures, and microscale acoustic transmission mechanisms for airborne topological acoustics, aimed at solving the aforementioned challenges in practical acoustic applications.

Acoustic analogues of the QHE, the QSHE and the QVHE, configured to form different types of sonic crystals or metamaterial structures, have their unique advantages and disadvantages. For example, acoustic analogues of the QHE for airborne topological acoustics have their advantages in nonreciprocal performance in a single unit cell and relatively good dynamic control performance, while still requiring bulky external airflow importing equipment, which makes it difficult to realize broadband and miniaturized topological acoustic properties. To overcome these defects and make these systems more practical in real applications, a design using heat-induced natural convection to form a steady air-flow circulation is proposed. Utilizing natural convection to import airflow rather than a fan or other mechanical equipment to induce airflow can effectively reduce the dimensions of the acoustic system and realize wide-band dynamically controlling performance, which can also break the time-reversal symmetry and achieve robust nonreciprocal acoustic propagation in a ring resonator. Specifically, in my work, a circulator with 120-degree rotational

symmetry of its three-port coaxial cylinders associated with three corresponding rectangular waveguides was designed. The distribution of a temperature gradient in a vertically placed ring circulator creates a steady circulating air-flow field due to the effect of buoyancy force. Meanwhile, velocity and flow direction in the circulator can be easily tuned by adjusting temperature distribution. In this scenario, no extra noise would be generated as no moving components are employed in the whole setup, which can facilitate its applications by conducting more accurate control and miniaturizing the whole structure. My design, a compact configuration without moving parts, creates a new paradigm for the application of nonreciprocal acoustics, which reduce the difficulty in device/material fabrication. Moreover, I further demonstrate that the nonreciprocal resonators with different interior circulator configurations, can exhibit excellent nonreciprocal acoustic propagation performance empowered by the heat-induced natural convection. This study also shows great potential for the insulation of any interior structures in acoustic circulators.

As for the acoustic analogue of the QSHE for the airborne topological acoustics, this type of design has its advantages in miniaturization while maintaining drawbacks in dynamic controlling and broadband acoustic transmission manipulation. The analogous pseudospin-down mode and pseudospin-up mode lock the acoustic wave in edges or specific transmission routes. This special modulation requirement makes it difficult to realize dynamic control, which often needs extra equipment and processes to manipulate the lattice array. To improve the performance of the QSHE based topological acoustic system, an airborne Floquet topological insulator system based on the modulation of acoustic impedance was designed. This modulation scheme possesses the ability to eliminate impedance matching challenges. This was achieved in an acoustic double-trimer lattice whose impedance matching is modulated by separating temperature distributions in each metamolecule, demonstrating the acoustic analogue of Floquet topological insulators. Different from Alu's on-site rotating modulation scheme in liquid, we demonstrate that the temperature-based modulation of acoustic impedance matching can function well in airborne topological acoustic systems, especially for the miniaturization of these systems. This opens a new avenue for practical applications of acoustic topological insulators. Specifically, for this modulation strategy, different temperatures can induce different acoustic impedances as density and acoustic speed change in distributed metamolecules of each trimer. As the

airborne acoustic impedance of metamolecules can be modulated effectively, up to tens of percents, this method opens the possibility of designing topologically protected, broadband, noiseless, dynamic controlling, and miniaturized (approximately 1/10 of other models in size, due to the existence of lumped impedance matching units) acoustic topological systems, including a broadband acoustic topological insulator, and a nonreciprocal acoustic array that is robust to impedance disorders.

As for the acoustic analogue of the QVHE for airborne topological acoustics, this type of design has its advantages in miniaturization while maintaining limited performance in dynamic controlling and broadband acoustic transmission. A design realizing tunable and broadband acoustic topological edge states in a flow-free resonator system with a millimeter order of magnitude for each small unit, which is based on the QVHE, was proposed. This two-dimensional periodic acoustic counterpart of a gapped graphene monolayer can be considered a tight-binding model. By designing tunable inner radii of adjacent hollow circulators to realize versatile combinations of chiral on-site rotating modulation schemes, the existence of a topological transition is demonstrated, which is characterized by the opposite valley Chern numbers. Different from breaking translational symmetries and point groups in pseudomagnetic fields, we mimic the QVHE-based valley states as opposed to spin states. Specifically, the mirror-symmetry-breaking property is accomplished by dynamically adjusting the inner radii of the six hollow circulators in each primitive cell. This induces inversed band modulation in different valley pseudospin degrees of freedom. Moreover, the tunable inner radius in each circulator can allow us to adjust this type of acoustic topological property with wide effective frequency ranges and configurable transmitting routes. Full-wave simulations of band structure analysis and acoustic propagation were conducted and used to display these fascinating physics of topological acoustics with versatile potential applications.

In order to realize the miniaturization of topological acoustic systems in a smaller scale compared to the existing dimensional magnitude, further investigation of the acoustic transmission mechanism in micro- and nanoscale is needed. Chapter 5 proposes a theoretical model with the second-order slip boundary to describe the acoustic wave propagation in micro- and nanochannels. The proposed theoretical model provides analytical solutions for the complex wavenumber, attenuation coefficient and other related transmission variables as

a function of the Knudsen number in the early transition regime ($0.1 < \text{Kn} < 1.0$), which are valuable for understanding acoustics at micro- and nanoscales. In addition, numerical simulations using the molecular-based DSMC method for dilute argon gas are carried out to validate the model and its analytical results. Findings suggest that such a model can effectively predict the acoustic behaviour in micro- and nanochannels, which is important for the future research about topological acoustics in ultrasonic or in a small structure to realize miniaturization.

6.2 Future work

The development of topological acoustics is still in its infancy, although many researchers have been working on this area in recent years. Different methods or designs based on the QHE, the QSHE or the QVHE have their own advantages and disadvantages, which lead to the need to design more practical topological acoustic devices or systems, including backscattering immune, tunable, broadband and miniaturized topological acoustic applications. These related applications include sound attenuation, ultrasonic imaging, information delivering, and acoustic cloaking, etc. My PhD work improves the performance of topological acoustic systems by introducing new modulation mechanisms and lattice arrays. However, tremendous efforts are still needed to put topological acoustic designs into practice.

Specifically, for my current work, optimizing the geometrical lattice array in the form of SCs or metamaterials in combination with thermal modulation is being investigated. Smaller dimensions and easier to reconfigure lattice arrays to realize wider functional frequency ranges are key optimizing objectives. Moreover, experimentally realizing programmable dynamic control of the thermal modulation in a miniaturized system is necessary in related acoustic applications. Also, we are working on using machine learning to investigate multiple variables, such as air velocity, structure geometry and temperature distribution, to optimize muffler and topological acoustic performance.

As for the future work, application-driven research is always needed. For ultrasonic imaging or information delivering, miniaturization plays a key role, which requires versatile control equipment and modulation mechanisms. The existing fan-induced airflow with a bulky structure is not applicable, and even for the QVHE based topological analogues, the

tunability of the unit cell using the mechanical method has a limited working frequency range and requires a complex supporting system. That means more advanced modulation strategies are needed. For sound attenuation and cloaking, optimized and frequency-dependent structure design is important in adapting to the requirements of different frequency ranges. Moreover, a complete theory guiding SCs and metamaterial design is strongly needed, especially for miniaturized structures. As for other applications of topological acoustics, such as acoustic MEMS sensors and on-chip filters, properties related to miniaturization and programmable tunability need further investigated.

Also, strategies used in photonic and electronic topological systems can still inspire and promote research in topological acoustics, as they have been developed over a longer time. The related research will continuously provide ideas and methodologies regarding sound manipulation and mechanical vibration to spearheaded novel wave physics. In many acoustic applications, combining acoustics with elasticity has more technological oriented applications and challenges. Therefore, realizing defect insensitive and topological robust wave manipulating, signal splitting and buffering, reveals new avenues for the improvement of on-chip filters in mobile phones, surface acoustic sensors, bio-chemical sensing robustness, and coupling efficiency in touchscreens. To handle the aforementioned challenges, efforts in shrinking the topological acoustical and mechanical geometries into a micro scale with novel relevant performance and properties should fully take advantage of topologically robust acoustic manipulation for unprecedented possibilities and routes for phononic technologies.

References

1. Blundell, S., *Magnetism in condensed matter*. 2003, AAPT.
2. Read, N., *Topological phases and quasiparticle braiding*. *Physics today*, 2012. **65**(7): p. 38.
3. Klitzing, K.v., G. Dorda, and M. Pepper, *New method for high-accuracy determination of the fine-structure constant based on quantized Hall resistance*. *Physical Review Letters*, 1980. **45**(6): p. 494.
4. Laughlin, R.B., *Quantized Hall conductivity in two dimensions*. *Physical Review B*, 1981. **23**(10): p. 5632.
5. Thouless, D.J., et al., *Quantized Hall conductance in a two-dimensional periodic potential*. *Physical Review Letters*, 1982. **49**(6): p. 405.
6. Benchabane, S., et al., *Evidence for complete surface wave band gap in a piezoelectric phononic crystal*. *Physical Review E*, 2006. **73**(6): p. 065601.
7. Sachdev, S., *Quantum phase transitions*. *Handbook of Magnetism and Advanced Magnetic Materials*, 2007.
8. Hatsugai, Y., *Chern number and edge states in the integer quantum Hall effect*. *Physical Review Letters*, 1993. **71**(22): p. 3697-3700.
9. Moore, J.E. and L. Balents, *Topological invariants of time-reversal-invariant band structures*. *Physical Review B*, 2007. **75**(12): p. 121306.
10. Berry, M.V., *Quantal phase factors accompanying adiabatic changes*. *Proceedings of the Royal Society of London. A. Mathematical and Physical Sciences*, 1984. **392**(1802): p. 45-57.
11. Monkhorst, H.J. and J.D. Pack, *Special points for Brillouin-zone integrations*. *Physical review B*, 1976. **13**(12): p. 5188.
12. Ihm, J., A. Zunger, and M.L. Cohen, *Momentum-space formalism for the total energy of solids*. *Journal of Physics C: Solid State Physics*, 1979. **12**(21): p. 4409.
13. Haldane, F.D.M., *Model for a quantum Hall effect without Landau levels: Condensed-matter realization of the "parity anomaly"*. *Physical Review Letters*, 1988. **61**(18): p. 2015.
14. Kane, C.L. and E.J. Mele, *Quantum spin Hall effect in graphene*. *Physical review letters*, 2005. **95**(22): p. 226801.
15. Fu, L., C.L. Kane, and E.J. Mele, *Topological insulators in three dimensions*. *Physical review letters*, 2007. **98**(10): p. 106803.
16. Qi, X.-L. and S.-C. Zhang, *Topological insulators and superconductors*. *Reviews of Modern Physics*, 2011. **83**(4): p. 1057.
17. Bernevig, B.A., T.L. Hughes, and S.-C. Zhang, *Quantum spin Hall effect and topological phase transition in HgTe quantum wells*. *Science*, 2006. **314**(5806): p. 1757-1761.
18. Nakada, K., et al., *Edge state in graphene ribbons: Nanometer size effect and edge shape dependence*. *Physical Review B*, 1996. **54**(24): p. 17954.
19. Cooper, A., et al., *Time-resolved magnetic sensing with electronic spins in diamond*. *Nature communications*, 2014. **5**: p. 3141.
20. Sheng, L., et al., *Nondissipative spin Hall effect via quantized edge transport*. *Physical review letters*, 2005. **95**(13): p. 136602.
21. Yao, W., D. Xiao, and Q. Niu, *Valley-dependent optoelectronics from inversion symmetry breaking*. *Physical Review B*, 2008. **77**(23): p. 235406.
22. Ju, L., et al., *Topological valley transport at bilayer graphene domain walls*. *Nature*,

2015. **520**(7549): p. 650.
23. Haldane, F., *Berry curvature on the Fermi surface: anomalous Hall effect as a topological Fermi-liquid property*. Physical review letters, 2004. **93**(20): p. 206602.
 24. Nayak, C., et al., *Non-Abelian anyons and topological quantum computation*. Reviews of Modern Physics, 2008. **80**(3): p. 1083.
 25. Sau, J.D., et al., *Generic new platform for topological quantum computation using semiconductor heterostructures*. Physical review letters, 2010. **104**(4): p. 040502.
 26. Bonderson, P., M. Freedman, and C. Nayak, *Measurement-only topological quantum computation*. Physical review letters, 2008. **101**(1): p. 010501.
 27. Yao, X.S. and L. Maleki, *Optoelectronic oscillator for photonic systems*. IEEE journal of Quantum Electronics, 1996. **32**(7): p. 1141-1149.
 28. Oshikawa, M., M. Yamanaka, and I. Affleck, *Magnetization plateaus in spin chains: "Haldane gap" for half-integer spins*. Physical review letters, 1997. **78**(10): p. 1984.
 29. Higgs, P.W., *Broken symmetries and the masses of gauge bosons*. Physical Review Letters, 1964. **13**(16): p. 508.
 30. Novoselov, K.S., et al., *Two-dimensional gas of massless Dirac fermions in graphene*. nature, 2005. **438**(7065): p. 197.
 31. Fleury, R., et al., *Sound isolation and giant linear nonreciprocity in a compact acoustic circulator*. Science, 2014. **343**(6170): p. 516-519.
 32. Ni, X., et al., *Topologically protected one-way edge mode in networks of acoustic resonators with circulating air flow*. New Journal of Physics, 2015. **17**(5): p. 053016.
 33. Yang, Z., et al., *Topological acoustics*. Physical review letters, 2015. **114**(11): p. 114301.
 34. Khanikaev, A.B., et al., *Topologically robust sound propagation in an angular-momentum-biased graphene-like resonator lattice*. Nature communications, 2015. **6**.
 35. Chen, Z.-G. and Y. Wu, *Tunable topological phononic crystals*. Physical Review Applied, 2016. **5**(5): p. 054021.
 36. Chen, Z.-G., et al., *Acoustic frequency filter based on anisotropic topological phononic crystals*. Scientific reports, 2017. **7**(1): p. 15005.
 37. Zhang, X. and Z. Liu, *Extremal transmission and beating effect of acoustic waves in two-dimensional sonic crystals*. Physical review letters, 2008. **101**(26): p. 264303.
 38. Torrent, D. and J. Sánchez-Dehesa, *Acoustic analogue of graphene: observation of Dirac cones in acoustic surface waves*. Physical review letters, 2012. **108**(17): p. 174301.
 39. Torrent, D., D. Mayou, and J. Sánchez-Dehesa, *Elastic analog of graphene: Dirac cones and edge states for flexural waves in thin plates*. Physical Review B, 2013. **87**(11): p. 115143.
 40. Zhu, Y., et al., *Experimental realization of acoustic chern insulator*. arXiv preprint arXiv:1801.07942, 2018.
 41. Sheng, D., et al., *Quantum spin-Hall effect and topologically invariant Chern numbers*. Physical review letters, 2006. **97**(3): p. 036808.
 42. Peng, Y.-G., et al., *Experimental demonstration of anomalous Floquet topological insulator for sound*. Nature communications, 2016. **7**: p. 13368.
 43. He, C., et al., *Topological phononic states of underwater sound based on coupled ring resonators*. Applied Physics Letters, 2016. **108**(3): p. 031904.
 44. Wu, L.-H. and X. Hu, *Scheme for achieving a topological photonic crystal by using dielectric material*. Physical review letters, 2015. **114**(22): p. 223901.

45. Zhang, Z., et al., *Topological creation of acoustic pseudospin multipoles in a flow-free symmetry-broken metamaterial lattice*. Physical review letters, 2017. **118**(8): p. 084303.
46. He, C., et al., *Acoustic topological insulator and robust one-way sound transport*. Nature Physics, 2016. **12**(12): p. 1124.
47. Fleury, R., A.B. Khanikaev, and A. Alu, *Floquet topological insulators for sound*. Nature communications, 2016. **7**.
48. Inoue, J.-i. and A. Tanaka, *Photoinduced transition between conventional and topological insulators in two-dimensional electronic systems*. Physical review letters, 2010. **105**(1): p. 017401.
49. Otterbach, J., et al., *Effective magnetic fields for stationary light*. Physical review letters, 2010. **104**(3): p. 033903.
50. Lindner, N.H., G. Refael, and V. Galitski, *Floquet topological insulator in semiconductor quantum wells*. Nature Physics, 2011. **7**(6): p. 490.
51. Kitagawa, T., et al., *Topological characterization of periodically driven quantum systems*. Physical Review B, 2010. **82**(23): p. 235114.
52. Dóra, B., et al., *Optically engineering the topological properties of a spin Hall insulator*. Physical review letters, 2012. **108**(5): p. 056602.
53. Pasek, M. and Y. Chong, *Network models of photonic Floquet topological insulators*. Physical Review B, 2014. **89**(7): p. 075113.
54. Rycerz, A., J. Tworzydło, and C. Beenakker, *Valley filter and valley valve in graphene*. Nature Physics, 2007. **3**(3): p. 172.
55. Xiao, D., W. Yao, and Q. Niu, *Valley-contrasting physics in graphene: magnetic moment and topological transport*. Physical Review Letters, 2007. **99**(23): p. 236809.
56. Semenoff, G.W., V. Semenoff, and F. Zhou, *Domain walls in gapped graphene*. Physical review letters, 2008. **101**(8): p. 087204.
57. Martin, I., Y.M. Blanter, and A. Morpurgo, *Topological confinement in bilayer graphene*. Physical review letters, 2008. **100**(3): p. 036804.
58. Zhang, F., et al., *Spontaneous quantum Hall states in chirally stacked few-layer graphene systems*. Physical review letters, 2011. **106**(15): p. 156801.
59. Zhang, X., *Observing Zitterbewegung for photons near the Dirac point of a two-dimensional photonic crystal*. Physical review letters, 2008. **100**(11): p. 113903.
60. Zandbergen, S.R. and M.J. de Dood, *Experimental observation of strong edge effects on the pseudodiffusive transport of light in photonic graphene*. Physical review letters, 2010. **104**(4): p. 043903.
61. Dong, J.-W., et al., *Valley photonic crystals for control of spin and topology*. Nature materials, 2017. **16**(3): p. 298.
62. Yang, Y., H. Jiang, and Z.H. Hang, *Topological valley transport in two-dimensional honeycomb photonic crystals*. Scientific reports, 2018. **8**(1): p. 1588.
63. Gao, F., et al., *Topologically protected refraction of robust kink states in valley photonic crystals*. Nature Physics, 2018. **14**(2): p. 140.
64. Lu, J., et al., *Dirac cones in two-dimensional artificial crystals for classical waves*. Physical Review B, 2014. **89**(13): p. 134302.
65. Lu, J., et al., *Valley vortex states in sonic crystals*. Physical review letters, 2016. **116**(9): p. 093901.
66. Ye, L., et al., *Observation of acoustic valley vortex states and valley-chirality locked beam splitting*. Physical Review B, 2017. **95**(17): p. 174106.
67. Lu, J., et al., *Observation of topological valley transport of sound in sonic crystals*.

- Nature Physics, 2017. **13**(4): p. 369-374.
68. Xia, B.-Z., et al., *Observation of valleylike edge states of sound at a momentum away from the high-symmetry points*. Physical Review B, 2018. **97**(15): p. 155124.
 69. Zhang, Z., et al., *Topological acoustic delay line*. Physical Review Applied, 2018. **9**(3): p. 034032.
 70. Wen, X., et al., *Acoustic Dirac degeneracy and topological phase transitions realized by rotating scatterers*. Journal of Applied Physics, 2018. **123**(9): p. 091703.
 71. Huo, S.-y., et al., *Simultaneous multi-band valley-protected topological edge states of shear vertical wave in two-dimensional phononic crystals with veins*. Scientific reports, 2017. **7**(1): p. 10335.
 72. Yang, Y., Z. Yang, and B. Zhang, *Acoustic valley edge states in a graphene-like resonator system*. Journal of Applied Physics, 2018. **123**(9): p. 091713.
 73. Zhang, Z., et al., *Directional Acoustic Antennas Based on Valley - Hall Topological Insulators*. Advanced Materials, 2018. **30**(36): p. 1803229.
 74. Brendel, C., et al., *Pseudomagnetic fields for sound at the nanoscale*. Proceedings of the National Academy of Sciences, 2017. **114**(17): p. E3390-E3395.
 75. Ezawa, M., *Topological Kirchhoff law and bulk-edge correspondence for valley Chern and spin-valley Chern numbers*. Physical Review B, 2013. **88**(16): p. 161406.
 76. Mong, R.S. and V. Shivamoggi, *Edge states and the bulk-boundary correspondence in Dirac Hamiltonians*. Physical Review B, 2011. **83**(12): p. 125109.
 77. Chen, S. and G.D. Doolen, *Lattice Boltzmann method for fluid flows*. Annual review of fluid mechanics, 1998. **30**(1): p. 329-364.
 78. He, X. and L.-S. Luo, *Theory of the lattice Boltzmann method: From the Boltzmann equation to the lattice Boltzmann equation*. Physical Review E, 1997. **56**(6): p. 6811.
 79. McNamara, G.R. and G. Zanetti, *Use of the Boltzmann equation to simulate lattice-gas automata*. Physical review letters, 1988. **61**(20): p. 2332.
 80. Bird, G.A., *Molecular gas dynamics and the direct simulation of gas flows*. 1994.
 81. Bhatnagar, P.L., E.P. Gross, and M. Krook, *A model for collision processes in gases. I. Small amplitude processes in charged and neutral one-component systems*. Physical review, 1954. **94**(3): p. 511.
 82. Qian, Y.-H., D. d'Humières, and P. Lallemand, *Lattice BGK models for Navier-Stokes equation*. EPL (Europhysics Letters), 1992. **17**(6): p. 479.
 83. He, X., S. Chen, and G.D. Doolen, *A novel thermal model for the lattice Boltzmann method in incompressible limit*. Journal of Computational Physics, 1998. **146**(1): p. 282-300.
 84. Chen, Y., H. Ohashi, and M. Akiyama, *Two-parameter thermal lattice BGK model with a controllable Prandtl number*. Journal of scientific computing, 1997. **12**(2): p. 169-185.
 85. Watari, M. and M. Tsutahara, *Two-dimensional thermal model of the finite-difference lattice Boltzmann method with high spatial isotropy*. Physical Review E, 2003. **67**(3): p. 036306.
 86. Yan, G., et al., *A multi - energy - level lattice Boltzmann model for the compressible Navier–Stokes equations*. International Journal for Numerical Methods in Fluids, 2007. **55**(1): p. 41-56.
 87. Kataoka, T. and M. Tsutahara, *Lattice Boltzmann method for the compressible Euler equations*. Physical review E, 2004. **69**(5): p. 056702.
 88. Qu, K., C. Shu, and Y. Chew, *Alternative method to construct equilibrium distribution functions in lattice-Boltzmann method simulation of inviscid compressible flows at*

- high Mach number*. Physical Review E, 2007. **75**(3): p. 036706.
89. Li, Q., et al., *Coupled double-distribution-function lattice Boltzmann method for the compressible Navier-Stokes equations*. Physical Review E, 2007. **76**(5): p. 056705.
 90. Chen, S., D. Martinez, and R. Mei, *On boundary conditions in lattice Boltzmann methods*. Physics of fluids, 1996. **8**(9): p. 2527-2536.
 91. Hadjiconstantinou, N. and O. Simek, *Sound propagation at small scales under continuum and non-continuum transport*. Journal of Fluid Mechanics, 2003. **488**: p. 399-408.
 92. Crandall, I.B., *Theory of vibrating systems and sound*. 1954: D. Van Nostrand Company.
 93. Stinson, M.R., *The propagation of plane sound waves in narrow and wide circular tubes, and generalization to uniform tubes of arbitrary cross - sectional shape*. The Journal of the Acoustical Society of America, 1991. **89**(2): p. 550-558.
 94. Hadjiconstantinou, N.G., *Validation of a second-order slip model for dilute gas flows*. Microscale Thermophysical Engineering, 2005. **9**(2): p. 137-153.
 95. Kozlov, V.F., A.V. Fedorov, and N.D. Malmuth, *Acoustic properties of rarefied gases inside pores of simple geometries*. The Journal of the Acoustical Society of America, 2005. **117**(6): p. 3402-3411.
 96. Umnova, O., D. Tsiklauri, and R. Venegas, *Effect of boundary slip on the acoustical properties of microfibrinous materials*. The Journal of the Acoustical Society of America, 2009. **126**(4): p. 1850-1861.
 97. Lorenzani, S., *Higher order slip according to the linearized Boltzmann equation with general boundary conditions*. Philosophical Transactions of the Royal Society of London A: Mathematical, Physical and Engineering Sciences, 2011. **369**(1944): p. 2228-2236.
 98. Ohwada, T., Y. Sone, and K. Aoki, *Numerical analysis of the shear and thermal creep flows of a rarefied gas over a plane wall on the basis of the linearized Boltzmann equation for hard - sphere molecules*. Physics of Fluids A: Fluid Dynamics (1989-1993), 1989. **1**(9): p. 1588-1599.
 99. Siewert, C., *Viscous-slip, thermal-slip, and temperature-jump coefficients as defined by the linearized Boltzmann equation and the Cercignani–Lampis boundary condition*. Physics of Fluids (1994-present), 2003. **15**(6): p. 1696-1701.
 100. Buick, J. and J. Cosgrove, *Investigation of a lattice Boltzmann model with a variable speed of sound*. Journal of Physics A: Mathematical and General, 2006. **39**(44): p. 13807.
 101. Huang, H., T. Lee, and C. Shu, *Lattice Boltzmann method simulation gas slip flow in long microtubes*. International Journal of Numerical Methods for Heat & Fluid Flow, 2007. **17**(6): p. 587-607.
 102. Chen, S. and Z. Tian, *Simulation of thermal micro-flow using lattice Boltzmann method with Langmuir slip model*. International journal of heat and fluid flow, 2010. **31**(2): p. 227-235.
 103. Loyalka, S., N. Petrellis, and T. Storvick, *Some numerical results for the BGK model: thermal creep and viscous slip problems with arbitrary accommodation at the surface*. Physics of Fluids (1958-1988), 1975. **18**(9): p. 1094-1099.
 104. Chew, Y., X. Niu, and C. Shu, *Three - dimensional lattice Boltzmann BGK model and its application to flows with heat transfer in a rectangular microchannel*. International journal for numerical methods in fluids, 2006. **50**(11): p. 1321-1334.

105. Hansen, J.S. and A. Lemarchand, *Mixing of nanofluids: molecular dynamics simulations and modelling*. Molecular Simulation, 2006. **32**(6): p. 419-426.
106. Waisman, H. and J. Fish, *A space-time multilevel method for molecular dynamics simulations*. Computer methods in applied mechanics and engineering, 2006. **195**(44): p. 6542-6559.
107. Greathouse, J.A., R.T. Cygan, and B.A. Simmons, *Vibrational spectra of methane clathrate hydrates from molecular dynamics simulation*. The Journal of Physical Chemistry B, 2006. **110**(13): p. 6428-6431.
108. Sharma, A. and L.N. Long, *Numerical simulation of the blast impact problem using the Direct Simulation Monte Carlo (DSMC) method*. Journal of Computational Physics, 2004. **200**(1): p. 211-237.
109. Wang, R.-J. and K. Xu, *The study of sound wave propagation in rarefied gases using unified gas-kinetic scheme*. Acta Mechanica Sinica, 2012. **28**(4): p. 1022-1029.
110. Shen, C., J. Fan, and C. Xie, *Statistical simulation of rarefied gas flows in micro-channels*. Journal of Computational Physics, 2003. **189**(2): p. 512-526.
111. Al-Mohssen, H.A. and N.G. Hadjiconstantinou, *Low-variance direct Monte Carlo simulations using importance weights*. ESAIM: Mathematical Modelling and Numerical Analysis, 2010. **44**(5): p. 1069-1083.
112. Song, G.Y., et al., *Broadband fractal acoustic metamaterials for low-frequency sound attenuation*. Applied Physics Letters, 2016. **109**(13): p. 131901.
113. Lewińska, M., et al., *The attenuation performance of locally resonant acoustic metamaterials based on generalised viscoelastic modelling*. International Journal of Solids and Structures, 2017. **126**: p. 163-174.
114. Ma, F., J.H. Wu, and M. Huang, *Resonant modal group theory of membrane-type acoustical metamaterials for low-frequency sound attenuation*. the European physical journal applied physics, 2015. **71**(3): p. 30504.
115. Lee, H., et al., *Extreme stiffness hyperbolic elastic metamaterial for total transmission subwavelength imaging*. Scientific reports, 2016. **6**: p. 24026.
116. Amireddy, K.K., K. Balasubramaniam, and P. Rajagopal, *Deep subwavelength ultrasonic imaging using optimized holey structured metamaterials*. Scientific reports, 2017. **7**(1): p. 7777.
117. Amireddy, K.K., K. Balasubramaniam, and P. Rajagopal, *Porous metamaterials for deep sub-wavelength ultrasonic imaging*. Applied Physics Letters, 2018. **113**(12): p. 124102.
118. Zhu, X., et al., *Acoustic cloaking by a superlens with single-negative materials*. Physical review letters, 2011. **106**(1): p. 014301.
119. Norris, A.N., *Acoustic cloaking*. Acoust. Today, 2015. **11**(1): p. 38-46.
120. Cummer, S.A., J. Christensen, and A. Alù, *Controlling sound with acoustic metamaterials*. Nature Reviews Materials, 2016. **1**(3): p. 16001.
121. Liu, X., Q. Guo, and J. Yang, *Tunable acoustic valley edge states in a flow-free resonator system*. Applied Physics Letters, 2019. **115**(7): p. 074102.
122. Hasan, M.Z. and C.L. Kane, *Colloquium: topological insulators*. Reviews of modern physics, 2010. **82**(4): p. 3045.
123. Hsieh, D., et al., *A topological Dirac insulator in a quantum spin Hall phase*. Nature, 2008. **452**(7190): p. 970.
124. Von Klitzing, K., *The quantized Hall effect*. Reviews of Modern Physics, 1986. **58**(3): p. 519.
125. Laughlin, R.B., *Anomalous quantum Hall effect: an incompressible quantum fluid*

- with fractionally charged excitations*. Physical Review Letters, 1983. **50**(18): p. 1395.
126. Fleury, R., A.B. Khanikaev, and A. Alu, *Floquet topological insulators for sound*. Nature communications, 2016. **7**: p. 11744.
 127. Liu, X., Q. Guo, and J. Yang, *Miniaturization of Floquet topological insulators for airborne acoustics by thermal control*. Applied Physics Letters, 2019. **114**(5): p. 054102.
 128. Liu, X., et al., *Study of acoustic wave propagation in micro- and nanochannels*. Wave Motion, 2018. **76**: p. 51-60.
 129. LIU, X., et al., *Robust nonreciprocal acoustic propagation in a compact acoustic circulator empowered by natural convection*. New Journal of Physics, 2019.
 130. Haldane, F. and S. Raghu, *Possible realization of directional optical waveguides in photonic crystals with broken time-reversal symmetry*. Physical review letters, 2008. **100**(1): p. 013904.
 131. Hafezi, M., et al., *Robust optical delay lines with topological protection*. Nature Physics, 2011. **7**(11): p. 907.
 132. Lu, L., J.D. Joannopoulos, and M. Soljačić, *Topological photonics*. Nature Photonics, 2014. **8**(11): p. 821.
 133. Süsstrunk, R. and S.D. Huber, *Observation of phononic helical edge states in a mechanical topological insulator*. Science, 2015. **349**(6243): p. 47-50.
 134. Mousavi, S.H., A.B. Khanikaev, and Z. Wang, *Topologically protected elastic waves in phononic metamaterials*. Nature communications, 2015. **6**: p. 8682.
 135. Nash, L.M., et al., *Topological mechanics of gyroscopic metamaterials*. Proceedings of the National Academy of Sciences, 2015. **112**(47): p. 14495-14500.
 136. Zhang, T., Y. Cheng, and X. Liu, *One-way self-collimated acoustic beams in two-dimensional asymmetric sonic crystals with circulating fluids*. Applied Physics Express, 2017. **10**(6): p. 067301.
 137. Khanikaev, A.B., et al., *Topologically robust sound propagation in an angular-momentum-biased graphene-like resonator lattice*. Nature communications, 2015. **6**: p. 8260.
 138. Mei, J., Z. Chen, and Y. Wu, *Pseudo-time-reversal symmetry and topological edge states in two-dimensional acoustic crystals*. Scientific reports, 2016. **6**: p. 32752.
 139. Guild, M.D., et al., *Aerogel as a Soft Acoustic Metamaterial for Airborne Sound*. Physical Review Applied, 2016. **5**(3): p. 034012.
 140. Souslov, A., et al., *Topological sound in active-liquid metamaterials*. Nature Physics, 2017. **13**(11): p. 1091.
 141. Xu, X., et al., *Spin and pseudospins in layered transition metal dichalcogenides*. Nature Physics, 2014. **10**(5): p. 343.
 142. fan Li, Y., et al., *Evolutionary topological design for phononic band gap crystals*. Structural and Multidisciplinary Optimization, 2016. **54**(3): p. 595-617.
 143. Yang, Y., et al., *A metasurface carpet cloak for electromagnetic, acoustic and water waves*. Scientific reports, 2016. **6**: p. 20219.
 144. Xie, Y., et al., *Acoustic Imaging with Metamaterial Luneburg Lenses*. Scientific reports, 2018. **8**(1): p. 16188.
 145. Laureti, S., et al., *High-resolution acoustic imaging at low frequencies using 3D-printed metamaterials*. AIP Advances, 2016. **6**(12): p. 121701.
 146. Ahmed, H., R. Ahmed, and S. Banerjee. *Butterfly metamaterial for acoustic holographic imaging through superlensing capability (Conference Presentation)*. in *Health Monitoring of Structural and Biological Systems XII*. 2018. International

- Society for Optics and Photonics.
147. Jiang, Y., et al., *Flexible film bulk acoustic wave filters toward radiofrequency wireless communication*. *Small*, 2018. **14**(20): p. 1703644.
 148. Yang, Q., et al., *A modified lattice configuration design for compact wideband bulk acoustic wave filter applications*. *Micromachines*, 2016. **7**(8): p. 133.
 149. Ghasemi Baboly, M., et al., *Acoustic waveguiding in a silicon carbide phononic crystals at microwave frequencies*. *Applied Physics Letters*, 2018. **112**(10): p. 103504.
 150. Ang, L.Y.L., Y.K. Koh, and H.P. Lee, *Broadband sound transmission loss of a large-scale membrane-type acoustic metamaterial for low-frequency noise control*. *Applied Physics Letters*, 2017. **111**(4): p. 041903.
 151. Lavazec, D., et al. *Attenuation of noise and vibration at low frequencies using a nonlinear microstructured material*. 2016.
 152. Man, X.-f., et al., *3D Hilbert fractal acoustic metamaterials: low-frequency and multi-band sound insulation*. *Journal of Physics D: Applied Physics*, 2019. **52**(19): p. 195302.
 153. Liu, Y. and J. Du, *Sound attenuation analysis and optimal design for a duct with periodic membranes embedded in its sidewalls*. *Journal of Applied Physics*, 2019. **125**(3): p. 034901.
 154. Cavalieri, T., et al., *Three-dimensional multiresonant lossy sonic crystal for broadband acoustic attenuation: Application to train noise reduction*. *Applied Acoustics*, 2019. **146**: p. 1-8.
 155. Suh, W., Z. Wang, and S. Fan, *Temporal coupled-mode theory and the presence of non-orthogonal modes in lossless multimode cavities*. *IEEE Journal of Quantum Electronics*, 2004. **40**(10): p. 1511-1518.
 156. Kane, C.L. and E.J. Mele, *Z₂ topological order and the quantum spin Hall effect*. *Physical review letters*, 2005. **95**(14): p. 146802.
 157. Liu, X., et al., *Study of acoustic wave propagation in micro- and nanochannels*. *Wave Motion*, 2018. **76**: p. 51-60.
 158. Chen, Y., et al., *Large Gap Topological Insulator Bi₂Te₃ with a Single Dirac Cone on the Surface*. arXiv preprint arXiv:0904.1829, 2009.
 159. Hsieh, D., et al., *A topological Dirac insulator in a quantum spin Hall phase (experimental realization of a 3D Topological Insulator)*. arXiv preprint arXiv:0910.2420, 2009.
 160. Casimir, H.B.G., *On Onsager's principle of microscopic reversibility*. *Reviews of Modern Physics*, 1945. **17**(2-3): p. 343.
 161. Bi, L., et al., *On-chip optical isolation in monolithically integrated non-reciprocal optical resonators*. *Nature Photonics*, 2011. **5**(12): p. 758-762.
 162. Sounas, D.L., C. Caloz, and A. Alu, *Giant non-reciprocity at the subwavelength scale using angular momentum-biased metamaterials*. *Nature communications*, 2013. **4**: p. 2407.
 163. Fan, L., et al., *An all-silicon passive optical diode*. *Science*, 2012. **335**(6067): p. 447-450.
 164. Khanikaev, A.B., et al., *Photonic topological insulators*. *Nat Mater*, 2013. **12**(3): p. 233-239.
 165. Rechtsman, M.C., et al., *Photonic Floquet topological insulators*. *Nature*, 2013. **496**(7444): p. 196-200.
 166. Lumer, Y., et al., *Self-localized states in photonic topological insulators*. *Physical review letters*, 2013. **111**(24): p. 243905.

167. Hafezi, M., et al., *Robust optical delay lines with topological protection*. 2011. **7**: p. 907.
168. Hafezi, M., et al., *Imaging topological edge states in silicon photonics*. Nature Photonics, 2013. **7**(12): p. 1001-1005.
169. Poo, Y., et al., *Experimental realization of self-guiding unidirectional electromagnetic edge states*. Physical review letters, 2011. **106**(9): p. 093903.
170. Lu, L., et al., *Weyl points and line nodes in gyroid photonic crystals*. Nature photonics, 2013. **7**(4): p. 294-299.
171. Kittel, C., *Interaction of spin waves and ultrasonic waves in ferromagnetic crystals*. Physical Review, 1958. **110**(4): p. 836.
172. Rinaldi, R., et al., *Zeeman effect in parabolic quantum dots*. Physical review letters, 1996. **77**(2): p. 342.
173. Deng, Y., et al., *Zone folding induced topological insulators in phononic crystals*. arXiv preprint arXiv:1706.05668, 2017.
174. Chen, Z.-G., et al., *Acoustic frequency filter based on anisotropic topological phononic crystals*. arXiv preprint arXiv:1706.07283, 2017.
175. Bergman, T.L. and F.P. Incropera, *Fundamentals of heat and mass transfer*. 2011: John Wiley & Sons.
176. Brekhovskikh, L.M. and O. Godin, *Acoustics of layered media II: Point sources and bounded beams*. Vol. 10. 2013: Springer Science & Business Media.
177. Wang, Z. and S. Fan, *Magneto-optical defects in two-dimensional photonic crystals*. Applied Physics B: Lasers and Optics, 2005. **81**(2): p. 369-375.
178. Bird, R., W. Stewart, and E. Lightfoot, *Transport Phenomena (revised 2nd ed.)* John Wiley & Sons. New York, 2007.
179. Mittal, S., et al., *Topologically robust transport of photons in a synthetic gauge field*. Physical review letters, 2014. **113**(8): p. 087403.
180. Wang, Z., et al., *Observation of unidirectional backscattering-immune topological electromagnetic states*. Nature, 2009. **461**(7265): p. 772.
181. Peano, V., et al., *Topological phases of sound and light*. Physical Review X, 2015. **5**(3): p. 031011.
182. Fang, K. and S. Fan, *Controlling the flow of light using the inhomogeneous effective gauge field that emerges from dynamic modulation*. Physical review letters, 2013. **111**(20): p. 203901.
183. Chen, Y. and L. Wang, *Periodic co-continuous acoustic metamaterials with overlapping locally resonant and Bragg band gaps*. Applied Physics Letters, 2014. **105**(19): p. 191907.
184. Zhou, X. and G. Hu, *Analytic model of elastic metamaterials with local resonances*. Physical Review B, 2009. **79**(19): p. 195109.
185. Rechtsman, M.C., et al., *Photonic Floquet topological insulators*. Nature, 2013. **496**(7444): p. 196.
186. Raghu, S. and F. Haldane, *Analogs of quantum-Hall-effect edge states in photonic crystals*. Physical Review A, 2008. **78**(3): p. 033834.
187. Chen, W.-J., et al., *Symmetry-protected transport in a pseudospin-polarized waveguide*. Nature communications, 2015. **6**: p. 8183.
188. Allard, J. and N. Atalla, *Propagation of sound in porous media: modelling sound absorbing materials 2e*. 2009: John Wiley & Sons.
189. Oka, T. and H. Aoki, *Erratum: Photovoltaic Hall effect in graphene [Phys. Rev. B 79, 081406 (R)(2009)]*. Physical Review B, 2009. **79**(16): p. 169901.

190. Gad-el-Hak, M., *The MEMS handbook*. 2001: CRC press.
191. Park, J.H., P. Bahukudumbi, and A. Beskok, *Rarefaction effects on shear driven oscillatory gas flows: a direct simulation Monte Carlo study in the entire Knudsen regime*. *Physics of Fluids* (1994-present), 2004. **16**(2): p. 317-330.
192. Gad-el-Hak, M., *The fluid mechanics of microdevices—the Freeman scholar lecture*. *Journal of Fluids Engineering*, 1999. **121**(1): p. 5-33.
193. Sharipov, F. and D. Kalempa, *Numerical modeling of the sound propagation through a rarefied gas in a semi-infinite space on the basis of linearized kinetic equation*. *The Journal of the Acoustical Society of America*, 2008. **124**(4): p. 1993-2001.
194. Greenspan, M., *Propagation of sound in five monatomic gases*. *The Journal of the Acoustical Society of America*, 1956. **28**(4): p. 644-648.
195. Meyer, E. and G. Sessler, *Schallausbreitung in Gasen bei hohen Frequenzen und sehr niedrigen Drucken*. *Zeitschrift für Physik*, 1957. **149**(1): p. 15-39.
196. Loyalka, S. and T. Cheng, *Sound - wave propagation in a rarefied gas*. *Physics of Fluids* (1958-1988), 1979. **22**(5): p. 830-836.
197. Sharipov, F., W. Marques Jr, and G. Kremer, *Free molecular sound propagation*. *The Journal of the Acoustical Society of America*, 2002. **112**(2): p. 395-401.
198. Kalempa, D. and F. Sharipov, *Sound propagation through a rarefied gas confined between source and receptor at arbitrary Knudsen number and sound frequency*. *Physics of Fluids* (1994-present), 2009. **21**(10): p. 103601.
199. Desvillettes, L. and S. Lorenzani, *Sound wave resonances in micro-electro-mechanical systems devices vibrating at high frequencies according to the kinetic theory of gases*. *Physics of Fluids* (1994-present), 2012. **24**(9): p. 092001.
200. Struchtrup, H., *Resonance in rarefied gases*. *Continuum Mechanics and Thermodynamics*, 2012. **24**(4-6): p. 361-376.
201. Danforth, A.L. and L.N. Long, *Nonlinear acoustic simulations using direct simulation Monte Carlo*. *The Journal of the Acoustical Society of America*, 2004. **116**(4): p. 1948-1955.
202. Hadjiconstantinou, N.G. and A.L. Garcia, *Molecular simulations of sound wave propagation in simple gases*. *Physics of Fluids* (1994-present), 2001. **13**(4): p. 1040-1046.
203. Cercignani, C., *The Boltzmann equation*, in *The Boltzmann Equation and Its Applications*. 1988, Springer. p. 40-103.
204. Hadjiconstantinou, N.G., *The limits of Navier-Stokes theory and kinetic extensions for describing small-scale gaseous hydrodynamics*. *Physics of Fluids* (1994-present), 2006. **18**(11): p. 111301.
205. Radtke, G.A., et al., *On the second-order temperature jump coefficient of a dilute gas*. *Journal of Fluid Mechanics*, 2012. **707**: p. 331-341.
206. Sone, Y., T. Ohwada, and K. Aoki, *Temperature jump and Knudsen layer in a rarefied gas over a plane wall: Numerical analysis of the linearized Boltzmann equation for hard - sphere molecules*. *Physics of Fluids A: Fluid Dynamics* (1989-1993), 1989. **1**(2): p. 363-370.
207. Li, Q., et al., *Lattice Boltzmann modeling of microchannel flows in the transition flow regime*. *Microfluidics and nanofluidics*, 2011. **10**(3): p. 607-618.
208. Colin, C.A., StÉphane, *High-order boundary conditions for gaseous flows in rectangular microducts*. *Microscale Thermophysical Engineering*, 2001. **5**(1): p. 41-54.
209. Wu, L., *A slip model for rarefied gas flows at arbitrary Knudsen number*. *Applied*

- Physics Letters, 2008. **93**(25): p. 253103.
210. Wagner, W., *A convergence proof for Bird's direct simulation Monte Carlo method for the Boltzmann equation*. Journal of Statistical Physics, 1992. **66**(3-4): p. 1011-1044.
 211. Chapman, S., *On the kinetic theory of a Gas. Part II: a composite monatomic gas: diffusion, viscosity, and thermal conduction*. Philosophical Transactions of the Royal Society of London. Series A, Containing Papers of a Mathematical or Physical Character, 1918. **217**: p. 115-197.
 212. Enskog, D., *The kinetic theory of phenomena in fairly rare gases*. 1917.
 213. Karniadakis, G., A. Beskok, and M. Gad-el-Hak, *Micro flows: fundamentals and simulation*. Applied Mechanics Reviews, 2002. **55**: p. 76.
 214. Zhang, H., et al., *Corrected second-order slip boundary condition for fluid flows in nanochannels*. Physical Review E, 2010. **81**(6): p. 066303.
 215. Liu, H.-Y., et al., *Study of gaseous velocity slip in nano-channel using molecular dynamics simulation*. International Journal of Numerical Methods for Heat & Fluid Flow, 2014. **24**(6): p. 1338-1347.
 216. Finger, G.W., J.S. Kapat, and A. Bhattacharya, *Molecular dynamics simulation of adsorbent layer effect on tangential momentum accommodation coefficient*. Journal of Fluids Engineering, 2007. **129**(1): p. 31-39.
 217. Kalempa, D. and F. Sharipov, *Sound propagation through a binary mixture of rarefied gases at arbitrary sound frequency*. European Journal of Mechanics/B Fluids, 2016(57): p. 50-63.

Curriculum Vitae

Name: Xingxing Liu

Post-secondary Education and Degrees: Tianjin University
Tianjin, China
2010-2014 B.A.

The University of Western Ontario
London, Ontario, Canada
2014-2019 Ph.D.

Honours and Awards: Outstanding Graduate of Tianjin University
2014

Graduate Teaching Assistantship & Graduate Research Assistantship
2014-2019

Related Work Experience Teaching Assistant & Research Assistant
The University of Western Ontario
2014-2019

Publications:

Liu X, Cai X, Guo Q, et al. Robust nonreciprocal acoustic propagation in a compact acoustic circulator empowered by natural convection[J]. *New Journal of Physics*, 2019, 21(5): 053001.

Liu, Xingxing, Qiuquan Guo, and Jun Yang. "Miniaturization of Floquet topological insulators for airborne acoustics by thermal control." *Applied Physics Letters* 114.5 (2019): 054102.

Liu X, Cai X, Guo Q, et al. Study of acoustic wave propagation in micro-and nanochannels[J]. *Wave Motion*, 2018, 76: 51-60.

Liu, X., Q. Guo, and J. Yang, Tunable acoustic valley edge states in a flow-free resonator system. *Applied Physics Letters*, 2019. **115**(7): p. 074102.